DISSERTATION

COMPUTATIONAL MODELING OF THE PHARMACOKINETICS AND PHARMACODYNAMICS OF SELECTED XENOBIOTICS

Submitted by

Todd J. Zurlinden

Department of Chemical and Biological Engineering

In partial fulfillment of the requirements

For the Degree of Doctor of Philosophy

Colorado State University

Fort Collins, Colorado

Fall 2016

Doctoral Committee:

Advisor: Brad Reisfeld

Sean Hays
Patrick Shipman
Brian Munsky

ABSTRACT

COMPUTATIONAL MODELING OF THE PHARMACOKINETICS AND PHARMACODYNAMICS OF SELECTED XENOBIOTICS

The determination of important endpoints in toxicology and pharmacology continues to involve the acquisition of large amounts of data through resource-intensive experimental studies involving a large number of resources. Because of this, only a small fraction of chemicals in the environment and marketplace can reasonably be evaluated for safety, and many promising drug candidates must be eliminated from consideration based on inadequate evaluation. Promisingly, advances in biologically-based computational models are beginning to allow researchers to estimate these endpoints and make useful extrapolations using a limited set of experimental data.

The work described in this dissertation examined how computational models can provide meaningful insight and quantitation of important pharmacological and toxicological endpoints related to toxicity and pharmacological efficacy. To this end, physiologically-based pharmacokinetic and pharmacodynamic models were developed and applied for several pharmaceutical agents and environmental toxicants to predict significant, and diverse, biological endpoints. First, physiologically-based modeling allowed for the evaluation of various dosing regimens of rifapentine, a drug that is showing great promise for the treatment of tuberculosis, by comparing lung-specific concentration predictions to experimentally-derived thresholds for antibacterial activity. Second, physiologically-based pharmacokinetic modeling, coupled with Bayesian inference, was used as part of a methodology to characterize genetic differences in acetaminophen pharmacokinetics and also to help clinicians predict an ingested dose of this drug

under overdose conditions. Third, a methodology for using physiologically-based pharmacokinetic modeling to predict health-based cognitive endpoints was demonstrated for chronic exposure to chlorpyrifos, an organophosphorus insecticide. The environmental public health indicators derived from this work allowed for biomarkers of exposure to be used to predict neurobehavioral changes following long-term exposure to this chemical. Finally, computational modeling was used to develop a mechanistically-plausible pharmacodynamic model for hepatoprotective and pro-inflammatory events to relate trichloroethylene dosing conditions to observed pathologies associated with auto-immune hepatitis.

ACKNOWLEDGEMENTS

I would like to thank my advisor, Dr. Brad Reisfeld, for his amazing guidance and support throughout the entirety of this work. From start to finish, Dr. Reisfeld imparted an extraordinary amount of knowledge onto me, continuously challenged me to scrutinize problems from multiple views and provided countless hours of his time to ensure my success. For all of this, and so much more, I am incredibly grateful to have completed my studies under his direction. I also thank my graduate committee: Dr. Sean Hays, Dr. Patrick Shipman, and Dr. Brian Munsky for their advice and expertise on each project. In addition, I thank Garrett Eppers for his persistence with the rifapentine model and his overall commitment to providing assistance throughout the entirety of this research. Also, I would like to thank all the members of the Quantitative and Computational Pharmacology and Toxicology group for their valuable discussions and comments throughout the years. To our collaborators, Dr. Kennon Heard and Dr. Kathleen Gilbert, I thank you for your expertise and willingness to assist in the development of our projects. Additionally, this research was supported by Colorado State University, the United States Environmental Protection Agency Science to Achieve Results (FP – 91730301), and the Bill and Melinda Gates Foundation, all of which allowed for the successful completion of the work presented in this dissertation. Lastly, I would like to thank the Department of Chemical and Biological Engineering at Colorado State University for providing so many opportunities for me to grow through the teaching and mentoring of students.

Outside of the academic environment, thank you to all my friends, both inside and outside the CBE department for helping make graduate school such an amazing experience, and to the San Francisco Giants for helping with that experience every other October. Finally, thank

you to my family for their incredible encouragement and support for the completion of this work. My parents, Ron and Trish Zurlinden, my brother Phillip, Kuips and Obi, and my amazing wife Samantha all provided the extra boost I needed to get the job done. I have to give considerable thanks to Samantha for her continuous support throughout my entire time at CSU. She pushed me to join Dr. Reisfeld's group as an undergraduate engineering major and was nothing but supportive throughout the entire length of graduate school.

DEDICATION

To my wife, Samantha, whose love and support truly helped make this journey possible.

TABLE OF CONTENTS

LIST OF TABLES

LIST OF FIGURES

CHAPTER 1

INTRODUCTION AND BACKGROUND

This dissertation details research centered on integrating knowledge of biological systems and mathematical and computational modeling to develop approaches useful in quantifying and characterizing human exposure to foreign chemicals (xenobiotics). The development and application of several of these computational models to describe relevant toxicological and pharmacological endpoints are presented in chapters 3-6. To give context to these chapters, a number of key concepts must first be presented, including the role of biological modeling in toxicology and pharmacology, how computational biologically-relevant models in these fields are developed and implemented, and how such models strengthen *in vivo* and *in vitro* experimental results and assist in building linkages between these standard experimental methodologies.

1.1 EXPOSURE TO XENOBIOTICS

Toxicology and pharmacology aim to study the effect of foreign chemicals on living systems. Animals, plants, and entire ecosystems are constantly exposed to xenobiotics and each exposure to a given chemical results in a biological or ecological consequence. Examples of xenobiotics include prescription drugs, environmental pollutants, food additives, and a number of other common household items [1]. Quantifying how these chemicals affect human health, both beneficially and adversely, requires a characterization of diverse biological, biochemical, and physiological processes and interactions. Consequences of exposure to xenobiotics can be beneficial (e.g., killing of harmful bacteria, the inhibition of cancer angiogenesis, pain relief) or harmful (organ toxicity, system disregulation, increased probability of cell mutation), depending

on (i) the magnitude and duration of exposure within the target tissue and (ii) the effect of the chemical species (and/or its metabolites) on the organism.

More formally, these two areas of concern are known as *pharmacokinetics* and *pharmacodynamics*. Pharmacokinetics aims to determine 'what the body does to the drug' through the processes of absorption, distribution, metabolism, and elimination (ADME). On the other hand, pharmacodynamics aims to characterize 'what the drug does to the body'. Here, the goal is to determine not only the biological response but also the intensity of that response once the drug reaches the target tissue or organ, i.e. the site of action. From a therapeutic perspective, ensuring that a drug enters the body and reaches a safe and effective level and the site of action is of the utmost importance; however from the viewpoint of safety, the paramount concern is assuring that the concentration of the chemical at the potential site of toxicity stays below an acceptable threshold. Together, pharmacokinetics and pharmacodynamics are critical fields in pharmacology and toxicology, allowing researchers to better understand the disposition and biological consequences of exposure to xenobiotics.

1.1.1 Current Methods for Assessing Toxicity and Efficacy

From the perspective of pharmacology or toxicology, biological responses depend on **two** conditions [2]:

1. A molecular target exists with which the xenobiotic interacts to initiate a response.
2. The drug reaches the site of action in a meaningful amount to induce this response.

If either one of these criteria is not met, a chemically-induced biological response will not occur. For example, if a molecular target within the lung initiates a mutation that leads to cancer, but the concentration of toxicant does not reach the necessary threshold to produce this effect, then an adverse biological response will not occur. Similarly, if animal studies demonstrate an

adverse health outcome due to the presence of a biological receptor in the rat, and this receptor is not present in humans, the observed biological effect will occur in humans. By utilizing knowledge of the above conditions, dose-response studies, and insights about the similarities and differences between animals and humans, results from *in vitro* and/or *in vivo* experiments can be utilized to gain insights into the pharmacological and toxicological characteristics of xenobiotics of interest.

1.1.1.1 In vitro methods

In vitro methods have the unique ability to probe very specific subsystems of the body to determine what effect a chemical might have on a tissue or organ of interest. In particular, using a minimal biomatrix, these methods are meant to mimic a susceptible body tissue or organ and determine changes in salient characteristics following chemical exposure. *In vitro* experiments can include high-throughput screening of drug candidates on an immortalized cell line to investigate the presence of a molecular receptor or cellular dysfunction following exposure to a chemical [3,4], enzyme-substrate assays to elucidate metabolic pathways [5], and tissue distribution and protein binding assays to determine drug bioavailability [6]. In general, these studies are designed to give investigators the ability to rapidly evaluate chemicals against batteries of tests indicative of key events along putative toxicological or pharmacological pathways. Because of their high-throughput nature, numerous chemicals can be tested and prioritized for further testing based on the desired/undesired biological responses they elicit [7].

Examples of an *in vitro* screening for drug efficacy include *Mycobacterium tuberculosis* (MTB) [8] killing kinetics experiments, receptor binding assays for the inhibition of cholesterol synthesis using statins [9], and dissolution tests for drug delivery vehicles to ensure proper release characteristics within a biological environment [10]. With respect to MTB killing

kinetics, strain of MTB of interest is grown in a biologically suitable environment with varying levels of local drug concentrations. The drug's potency as an anti-TB compound is determined through the mean inhibitory concentration (MIC) which is simply the lowest antibacterial concentration that prevents bacterial growth following incubation with the antibacterial drug [11]. In this application, *in vitro* methods allow for a high throughput screening of drugs against a target of interest to determine antimicrobial activity, rank candidates with respect to efficacy [8], and assess the potential for bacterial resistance [11].

Rather than the evaluation of therapeutic efficacy, *in vitro* methods for environmental toxicants aim to characterize the concentration-response for a chemical interacting with a specific receptor within the body that may result in an adverse health outcome. These *in vitro* studies have a two-fold purpose in that they elucidate the biological mechanisms that lead to the biological response and provide a concentration-dependent relationship between the chemical and the observed biological response. One example of using *in vitro* methods for characterizing toxicity was for organophosphorus (OP) insecticides. When these insecticides were first synthesized, researchers understood that cholinergic interactions within the central nervous system (CNS) played a role in the observed acute toxicity [12]. However, the mechanism of action to produce this toxicity within the CNS was unknown. Using *in vitro* experimentation, it was determined that the inhibition of muscarinic acetyl cholinesterase (mAChE) enzymes within the central nervous system resulted in acetylcholine neurotransmitter accumulating within the synaptic cleft [12,13]. This accumulation of parasympathetic neurotransmitter explained the observable OP toxicity such as lethargy, nausea, muscle twitches, respiratory paralysis, and possible death [14]. In addition to demonstrating the target receptor for the toxicant, these studies also quantified the degree of inhibition based on how much insecticide was present at the site of

action. One of the most comprehensive *in vitro* developments for high-throughput analysis is the U.S. Environmental Protection Agency's ToxCast project [15]. With the thousands of chemicals and chemical families currently registered for use, it is not feasible to test each one of these chemicals individually for toxicity. This program utilizes pathway-specific assays to assess molecular and pathway perturbations from a given chemical concentration. Therefore, *in vitro* assay development focuses on characterizing *in vivo* systems to determine which chemicals within an extensive chemical space perturb the system of interest [16].

In sum, for both drugs and toxicants, *in vitro* experimentation can be valuable to identify receptor targets at the site of action, the degree of interaction between receptors and drug, and the rates of transport/metabolism too and from the target tissue. Moreover, the relatively low cost and high throughput nature of these assays often facilitates the screening of large libraries of chemicals in a short time.

1.1.1.2 In vivo methods

Because of various ethical and practical issues, testing of unknown chemicals on human subjects is often impractical or impossible; thus, animal models are commonly used to mimic human diseases and human processes and metabolic pathways [17]. At the physiological and anatomical level, mammals are very similar [18]. This similarity lends itself to testing environmental toxicants and pharmaceutical drugs on animals and extrapolating those effects to humans. This extrapolation is often accomplished through a variety of animal models, including gene knockout/knockin mice for human disease or zebrafish for vertebrate developmental biology [19]. For example, to investigate the autoimmune effects of trichloroethylene (TCE) on humans, genetically-altered mice are used as a model system of systemic lupus [20]. Upon exposure to TCE, these mice exemplify the autoimmune effects of TCE exposure in the liver

through the production of liver-specific anti-bodies, inflammatory responses, and idiopathic autoimmune hepatitis (AIH). This *in vivo* system gives insight into how a mammalian liver reacts to chronic TCE exposure and, provided that similar metabolic network pathways and receptors are present in humans, AIH progression can be extrapolated to human exposure. This strategy is similar for most toxicity or pharmaceutical studies that take advantage of an animal model to study a particular disease or chemical exposure outcome. By using an animal model that sufficiently represents the human disease and biological network surrounding the disease, insights into the potential human response to the given xenobiotic can be gained [21]. In addition, once it has been demonstrated that there is minimal potential for toxicity in an animal model, targeted studies can then be conducted in humans to investigate efficacy and safety.

In addition to investigating the action of the drug or toxicant on the organism, *in vivo* pharmacokinetic studies have proven essential in both pharmacology and toxicology. When conducting such studies, investigators determine the levels of parent compound and relevant metabolites in blood and tissues of interest over time. These measurements are then used to quantify measures such as absorption rates, chemical half-life, tissue distribution, and the metabolic fate of the xenobiotic. As with pharmacodynamic studies, pharmacokinetic testing on humans is relatively limited and is generally restricted to xenobiotic measurements that are relatively non-invasive, such as the blood, urine, or saliva. The biomatrix measurements limit the amount of internal dose information, leading researchers to extrapolate information obtained from studies in animals.

Finally, by integrating results from pharmacokinetic and pharmacodynamic studies, observed pharmacodynamic responses can be linked to the initially administered dose. Ultimately, this relationship between ‘what the body does to the chemical’ and ‘what the

chemical does to the body' is foundational to the field of toxicology and pharmacology. Once this relationship has been determined, risk assessments that protect human health from environmental toxicants, or clinical trials for pharmaceutical drugs can be developed and refined, resulting in a better understanding of these health outcomes.

1.1.1.3 Characterizing endpoints for toxicity/efficacy testing

Modern approaches to risk and safety assessment [22,23] integrate data from *in vitro* and *in vivo* studies to evaluate the toxicity or efficacy of xenobiotics. Therefore, the above *in vitro* and *in vivo* studies are designed to determine the effects a given chemical induces based on the administered dose. The effects are characterized by a measurable biological endpoint, with this endpoint measurement reflecting a current physiological state. This state can represent progression/regression of disease, injury to an organ, or a direct measure of the overall health of the organism. In addition, clinical endpoints for a pharmaceutical drug can include the survival rate of a disease, decreased rate of developing a condition, or improvement of disease symptoms. In many situations, useful *surrogate* endpoints can be used to assess the health of an individual from a more quantitative standpoint rather than objective or subjective clinical endpoints, i.e. alanine aminotransferase levels in the serum as a measure for hepatotoxicity, blood pressure and cholesterol as a measure for heart disease and stroke risk, and cognitive learning tests as a measure for CNS damage. Finally, exposure to a single drug can result in multiple observed biological endpoints. In protecting against toxicity, the endpoint that occurs at the lowest dose, i.e. the sensitive or critical endpoint, is the endpoint that must be considered.

1.1.2 Limitations of Current Methods

The ethical concerns and substantial resources surrounding *in vivo* animal testing is continuously scrutinized. From an economic standpoint, the sheer cost of animal experiments,

such as a long-term mouse study conducted over three years, can be upwards of $1-2 million [24]. In all of these *in vivo* studies, the animals must eventually be sacrificed for measurement of internal dose and pharmacodynamic outcomes. Compounding the issues with animal testing is the uncertainty surrounding the extrapolation of effects from animal to human. In 2007, then U.S. Secretary of Health and Human Services, Mike Leavitt stated that "nine out of ten experimental drugs fail in clinical studies because we cannot accurately predict how they will behave in people based on laboratory and animal studies" [25]. In addition, animal models of human disease are constantly called into question, and one animal model might produce a completely different biological response than another accepted animal model [26–28].

For all of these reasons, and more, the European Union has instituted a ban on animal testing for cosmetics [29] and has restricted overall animal testing "as a last resort to satisfy registration information requirements" [30]. In the United States, agencies have made a move towards reduced animal testing propelled in part by the recently amended Toxic Substances Control Act (TSCA) which states that, "The Administrator shall reduce and replace, to the extent practicable, scientifically justified, and consistent with the policies of title, the use of vertebrate animals in the testing of chemical substances or mixtures" [31]. To account for this shift in policy, both the Federal Drug Administration (FDA) and Environmental Protection Agency (EPA) have moved towards "reduced animal testing" with significant resources dedicated to *in vitro* methods and computational models for the prediction of adverse health outcomes in humans [32,33]. Because of this governmental pressure and the need to create more robust and predictive methods for determining a chemical's effect within a human, alternatives to animal testing are continuously being developed and are currently of great priority.

Even *in vitro* studies, which are of much less resource intensive and controversial than their *in vivo* counterparts have severe limitations, principally the inability to recapitulate processes and outcomes observed in living organisms. Any living system is a complex arrangement of tissues, metabolic networks, and barriers to transport, which all influence how the chemical reaches and influences the site of action. For example, when investigating classic glucuronidation of a compound through phase II metabolism, there are many discrepancies between results obtained through *in vivo* and *in vitro* models due to factors such as up- or down-regulation of substrate-influencing enzymes and the transport of cofactor into the hepatocyte [34].

Furthermore, *in vitro* cell cultures themselves often lack the ability to replicate the complex tissues and cell lines necessary to obtain results that are directly translatable to animals. Two of the more apparent issues with these cell lines are (i) the orders of magnitude decrease in cell density compared to their respective organ and the impact this has on cell viability [35] and (ii) the non-homeostatic culture conditions where the system changes rapidly upon administration of the chemical, rather than gradually over time as would be seen in a living organism. These issues have been shown to significantly impact results of toxicity and efficacy tests [17].

1.2 Computational Modelling to Complement Current Methodologies

Owing to advances in computational technologies and the understanding of mechanisms governing toxicity and pharmacological efficacy, computational modeling is increasingly used to complement experimental studies and address some of the limitations inherent within *in vitro* and *in vivo* testing. In general, these computational models have been developed to derive

quantitative relationships between dose and endpoint over the continuum of exposure and extrapolate effects outside of the space in which experimentation has been conducted.

With regard to the first point, biological modeling aims to describe the experimental space using biologically-plausible equations and information gleaned from *in vitro* and *in vivo* experiments. This third arm of chemical assessment, termed *in silico*, serves as the tool for linking *in vitro* systems that do not perfectly replicate cell physiology with *in vivo* results that may be limited in scope and unable to quantify levels of chemical species needed to guide decision making. In addition, because these models can be formulated based on rigorous biological and mechanistic information, they often allow for dose extrapolation outside the range of a particular study and between species, i.e. establishing plausible linkages between animal and human. Ultimately, these biological models allow for endpoint prediction and the tracking of chemical species from chemical exposure to the target tissue. Finally, these models allow for investigation concerning pathway perturbations and dose optimization to determine potential effects of a new chemical [32] or existing pharmaceutical drug [36,37].

These features make computational modeling applicable to numerous areas of pharmacology and toxicology. For instance, from a pharmaceutical side, these models can be used to predict internal concentrations required for efficacy [37,38] and/or toxicity [36,39]. Once constructed and validated, models can also be used to investigate differences in metabolism between ethnically different populations [40] and provide insight into the optimal sampling conditions needed to reduce uncertainty in reconstructing administered doses [39]. Similarly, these models have applicability to a wide variety of applications involving environmental toxicants. For instance, they can be used within a framework of risk assessment [41] to aid in regulatory decision making or may facilitate the determination of dosing scenarios which gives

rise to an adverse biological outcome [42]. In all of these examples, linkages are made between available *in vitro* and *in vivo* data to create an accurate mathematical representation of the living organism.

1.3 Relevant Modeling Approaches

In order to understand how a chemical interacts with the body, we must first describe how the drug reaches the site of action and how long the drug remains there. To accomplish this, computational pharmacokinetics applies mathematical equations to simulate the ADME of the drug once administered to the organism. Comparatively, computational pharmacodynamics applies mechanistically realistic formulas to describe the biological response based on the amount of drug or toxicant present at the site of action.

In the following sections is an overview of the relevant modeling techniques used in this research. While the modeling of each drug or toxicant system requires a thorough understanding of the unique properties of the compound and the specific biological processes and interactions, the approach presented here gives an outline of the general procedures used to develop a given pharmacokinetic or pharmacodynamic model.

1.3.1 Pharmacokinetic Model Development

A variety of computational methods has been developed to mathematically describe the processes of absorption, distribution, metabolism, and excretion. These approaches generally fall into two categories: (i) "classical", data-driven models and (ii) physiologically-based pharmacokinetic models. The former approach assumes homogeneity throughout the body to describe characteristics of the drug related to how long it spends in the body and how well it distributes to tissues [43]. While these model types are convenient for characterizing the ADME of a drug under the given dosing conditions, they are not based on descriptions of inherent

biological processes and therefore cannot be used to extrapolate to lower doses, across species, or to a different route of exposure [44].

One of the most flexible approaches for whole-body pharmacokinetic analysis is physiologically-based pharmacokinetic (PBPK) modeling, which is developed using quantitative descriptions of the anatomy, physiology, and biochemistry of the organism [45]. Here, tissues are described using appropriate organ volumes and weights and flow into and out of these compartments are governed by relevant arterial and venous blood flow. Because of its physiological and mechanistic foundation, PBPK models are useful in extrapolation outside of the measured dose range, between species, or across different routes of exposure by adjusting the model structure and/or parameters [44].

1.3.1.1 Absorption

The absorption process begins immediately after the chemical enters the first cellular layer of the organism [46]. The mechanism in which the drug transports from the environment to the organism is called the route of exposure and each route requires a different mechanistic description to characterize how the drug enters the body. Primary routes of exposure examined in this work are oral, dermal, and inhalation, though xenobiotic exposure (or administration) may also occur via other routes such as intravenous, subcutaneous, and rectal. For oral administration of a drug, absorption occurs as the drug dissolves in the stomach, transits the gastrointestinal tract lumen, and is absorbed into the hepatic portal vein [46]. For a dermal route of exposure, absorption begins on the skin as the chemical is transferred from the epidermis, the dermis, and ultimately to the blood vessels [47]. Finally, for an inhaled compound, absorption occurs rapidly through the alveoli, into the blood stream [46,48].

The foundational equations in the PBPK model are species mass balances. As illustrated below, the exposure equations involve a forcing function, $I(t)$, that represents the initial dosing rate including the dose amount, duration, and periodicity of the exposure:

Oral:

$$\begin{aligned} \frac{dA_{ST}}{dt} &= I(t) - k_a A_{ST} \\ \frac{dA_{GI}}{dt} &= k_a A_{ST} - k_P A_{GI} \end{aligned} \tag{1.1}$$

Here, A_{ST} and A_{GI} represent the amount of drug in the stomach and gastrointestinal (GI) tract, respectively. Mass transport constants, k_a and k_p, represent the first order rate of absorption from the stomach into the GI and the first order perfusion rate from the GI into the hepatic portal vein.

Dermal:

$$\begin{aligned} \frac{dA_{epi}}{dt} &= I(t) - k_e A_{epi} - \frac{dA_{dis}}{dt} \\ \frac{dA_{derm}}{dt} &= k_e A_{epi} - k_d A_{derm} \end{aligned} \tag{1.2}$$

A_{epi} and A_{derm} represent the amount of chemical on the epidermis and within the dermis of the skin respectively. Similar to oral absorption, k_e and k_d represent the first order mass transfer rate from the epidermis to the dermis and from the dermis to the venous bloodstream. dA_{dis}/dt is the rate of dissipation of chemical from the skin back into the environment. It should be noted that an underlying assumption of this dermal absorption model is that k_e and k_d account for the mass transfer through all layers of the skin.

Inhalation:

$$\frac{dA_L}{dt} = Q_L\left(C_{A,f} - C_{VL}\right) + \frac{dA_{Inh}}{dt} - \frac{dA_{Exh}}{dt}$$
$$\frac{dA_{Inh}}{dt} = I(t)\cdot \mathrm{Q}_{Alv} \tag{1.3}$$
$$\frac{dA_{Exh}}{dt} = Q_{Alv}\cdot C_{Exh}$$

Inhalation requires an accurate description of the lung compartment (described below) in addition to rates of inhalation and exhalation. In eq. (1.3), Q_{alv} represents the alveolar ventilation rate and C_{Exh} is the concentration of chemical in exhaled air. dA_{Inh}/dt and dA_{Exh}/dt represent the rates of inhalation and exhalation respectively.

The equations presented above are based on various assumptions such as rapid dissolution of the drug into the aqueous phase, uninterrupted exposure, and constant physiological properties over the duration of exposure.

1.3.1.2 Distribution

Once the chemical is absorbed into the body and enters the bloodstream, the distribution will depend on factors such as the physicochemical properties of the drug. Traditionally, transport of the drug from the blood into the tissue is governed by passive diffusion described through Fick's first law of diffusion. Here, the diffusive flux into the tissue is proportional to the drug concentration gradient [45]:

$$\frac{dA_{tissue}}{dt} = k_T\left(A_{blood} - A_{tissue}\right) \tag{1.4}$$

The mass transfer coefficient for each tissue (k_T) is defined using physiological parameters where $k_T = Q_T/\left(P_T\cdot V_T\right)$ and Q_T is the arterial blood flow into the tissue, V_T is the physiological volume of the tissue, and P_T is the tissue:blood partition coefficient. Modeled as a perfectly mixed

compartment with no generation or consumption of drug, the following equation describes the time-course change of chemical for a given compartment:

$$\frac{dA_T}{dt} = Q_T \left(C_{A,f} - C_{VT} \right) \tag{1.5}$$

where $C_{A,f}$ is the unbound arterial blood concentration and C_{VT} is the blood concentration leaving the tissue, i.e. pooling in the venous blood stream [44]. C_{VT} is calculated using volume of the compartment along with the tissue:blood partition coefficient such that $C_{VT} = A_T / (V_T \cdot P_T)$. Traditionally, Q_T and V_T are calculated using allometrically scaled cardiac outputs and volumes based on the species of interest. This scaling allows for differences in body weight (BW) to be extrapolated to differences in tissue volumes and arterial flow rates and is usually governed through BW^{α} where typical values for α are 1 and 0.75 for tissue volumes and blood flow rates respectively [45].

The physiochemical parameter unique to each compound in the distribution phase is the tissue:blood partition coefficient (P_T). This parameter describes the equilibrium ratio of compound concentration between the tissue and blood stream and quantitates the chemical's affinity to a given tissue. For example, a hydrophobic compound will have a high affinity to adipose tissue, resulting in a relatively large Fat:Blood partition coefficient. Having an accurate estimate for this parameter value is imperative for developing tissue-specific compartments that are reflective of the physiology and physicochemistry of the chemical. A number of methods have been developed for determining this chemical-specific parameter [49–51] two of which were utilized in this research. The first method utilizes quantitative structure-activity relationships (QSARs) to predict partition coefficients [49,50] based on properties specific to the compound, such as pKa, octanol/water partition coefficient (logP), and binding affinity. While these models can provide reasonable estimates in many cases instances [52], they generally

provide poor predictions for molecules with a large molecular weight (>500 Da) or chemicals that exhibit uncharacteristic behavior inside the body [53]. The second method for the estimation of tissue:blood partition coefficients utilizes data from animal studies. Specifically, during the elimination phase of the concentration versus time curve, the rate of chemical diffusion into the tissue is equal to the rate of diffusion out of the tissue. Under these equilibrium conditions, the ratio of tissue concentration divided by the unbound blood concentration represents the tissue:blood partition coefficient. While this method provides a more accurate tissue:blood partition coefficient estimate, it also requires adequate experimental data on the xenobiotic of interest in tissues relevant to the PBPK model.

1.3.1.3 Metabolism

The metabolic rate equations describe the biotransformation of parent chemical into its metabolites. The liver is frequently the primary organ for metabolism and by incorporating relevant chemical kinetics with species mass balances, time-course metabolic concentrations can be computed. Chemical rate equations can take a variety of forms, but because metabolic reactions within the body are generally mediated by enzymes, a Michaelis-Menten kinetic description is often implemented to describe the generation/consumption of a chemical species:

$$\begin{aligned} \frac{dA_{met}}{dt} &= \frac{V_{\max} C_L}{K_M + C_L} \\ \frac{dA_L}{dt} &= Q_L \left(C_{A,\mathrm{f}} - C_{LV} \right) - \frac{dA_{met}}{dt} \end{aligned} \tag{1.6}$$

Here, C_L and A_L represent the concentration and molar amount of parent compound in the liver respectively. dA_{met}/dt is the metabolic rate of consumption and V_{max} and K_M are the Michaelis-Menten constants for enzyme-mediated reactions. These constants can be derived from *in vitro*

enzyme-substrate reactions, or through *in vivo* studies where both parent and metabolite concentrations are measured.

1.3.1.4 Elimination

The kidney serves as the primary organ for the elimination of parent drug and/or metabolites through glomerular filtration of unbound, water-soluble compounds into the urine. Mathematically, using the concentration of unbound chemical in the arterial blood stream, the kidney compartment of the PBPK model can be modeled using the following relationship:

$$\frac{dA_K}{dt} = Q_K \left(C_{A,f} - C_{VK} \right) - k_R C_K \tag{1.7}$$

Here, elimination is governed through the renal mass transfer coefficient (k_R) where only chemicals within the kidney are eliminated and subsequently accumulate in the urine. In addition to renal elimination, biliary elimination removes the compound through the bile. Bile reabsorbed into the GI tract can be reabsorbed into the body, enterohepatic recirculation, or ultimately removed through the feces [54].

1.3.1.5 Developing physiologically-based pharmacokinetic models

The system of equations comprising the PBPK model contains many parameters: physiological parameters specific to the organism and physiochemical parameters specific to the chemical. Most of the required physiological parameters, such as cardiac output, organ weights, and tissue blood flow, are tabulated in Brown et al. [55] for a multitude of animal species. As noted earlier, physiochemical parameters, such as partition coefficients and metabolic parameters are specific to the chemical of interest and must be estimated using experimental data or theoretical approaches.

1.3.2 Pharmacodynamic model development

Unlike PBPK modeling, there is no unifying framework for pharmacodynamic (PD) model development since each PD model is meant to describe a unique biological interaction or outcome. Thus, successful development of PD models requires knowledge of which biological receptors are influenced by the presence of the drug and how drug-induced perturbations to the homeostatic receptor network affect the physiology of the body. The ability to predict this effect hinges on developing a plausible mathematical relationship between the concentration at the site of action and the observed biological response. The basic requirements for a PD model include concentrations or concentration surrogates of chemical at the site of action, a description of how the chemical interacts with a receptor at the site of action, and a relationship between the change in receptor and the observed effect on the body. This relationship can be mechanistic where the mechanism of action has been determined, or semi-mechanistic to describe a higher-level interaction between the chemical and body. This modeling structure allows for relationships between *in vitro* experiments and *in vivo* results to be identified [56]. What follows is a brief review of some basic PD modeling structures utilized in this research and the assumptions surrounding them.

Though numerous PD models have been developed to make predictions for various systems of interest [44,56–59], here we focus on two broad model types used in the present research. The first type of model is based on the Hill equation, often known as the E_{max} model, and is used to describe how a drug concentration at the site of action influences the resulting pharmacodynamic effect. This model assumes that drug effects (E) are directly proportional to a receptor's occupancy level. When the receptor binds drug concentration at the site of action (C_s),

the following sigmoidal E_{max} model describes how the resulting health effect is directly related to the occupancy of the receptor [44,56]:

$$E = E_0 \pm \frac{E_{\max} C_S^{\gamma}}{EC_{50} + C_S^{\gamma}}, \tag{1.8}$$

where E_0, E_{max}, and EC_{50} are the initial effect, maximal effect, and drug concentration when 50% of maximal effect is attained, respectively. The exponent, γ, represents a fitting constant to describe the steepness in transition from no effect to full effect. The E_{max} model is an example of a "direct response" model where the concentration at the site of action is directly responsible for binding a receptor and causing the drug effect.

Conversely, an indirect pharmacodynamic model describes a chain of events initiated by the presence of the drug. Here, the measured change in response, or effect, over time depends on a series of indirect mechanisms where factors controlling the effect are either inhibited or stimulated by the presence of the chemical [60,61]. The homeostasis rate of change for a response is described using the following system of coupled ordinary differential equations:

$$\begin{aligned} \frac{dR_1}{dt} &= k_{up,1} - k_{down,1} R_1 \\ \frac{dR_2}{dt} &= k_{up,2} - k_{down,2} R_2 \\ &\vdots \\ \frac{dR_i}{dt} &= k_{up,i} - k_{down,i} R_i \end{aligned} \tag{1.9}$$

Here, $k_{up,i}$ and $k_{down,i}$ represent the zeroth order production of the biological response and the first order loss of the biological response, respectively. In the presence of an exogenous chemical of interest, a change to these rate constants implies an inhibited response, $f(c)k_{up,i}$, or a stimulated response effect $f(c)k_{down,i}$ where $f(c)$ represents the concentration-dependent effect on the rate constant bounded between zero and one [42,60,62]:

$$\frac{dR_1}{dt} = f(C)k_{up,1} - k_{down,1}R_1$$
$$\frac{dR_1}{dt} = k_{up,1} - f(C)k_{down,1}R_1 \quad (1.10)$$

In the first line of Eq. (1.10), k_{up} is limited due to the presence of the interacting chemical concentration (C) which ultimately decreases the overall rate of response. However, when k_{down} is reduced through *f(c)*, the rate of loss of response is reduced. By limiting this pathway, the overall rate of response increases.

Many drugs or environmental toxicants induce a biological response through the inhibition or stimulation of endogenous factors. These factors can initiate a cascade of downstream events to produce the observed effect. By mathematically describing the homeostasis of the system through a series of biologically-plausible steps, perturbations to the system from chemical exposure can be investigated to determine the chemical concentration responsible for initiating the change in response.

1.3.3 Model parameterization

In order for PBPK and PD models to be physiologically realizable, they must be parameterized using data derived from experimental studies. As previously stated, a majority of PBPK parameters can be estimated through *in vivo* and *in vitro* methods. However, when a parameter cannot be determined from such data, numerical fitting techniques must be implemented. There are numerous methods for this estimation; three that were used extensively throughout this research are outlined below.

1.3.3.1 Linear regression

One of the simplest forms of modeling the relationship between a dependent variable (y) and one or more explanatory, independent variables (x) is through linear regression [63]. In most

cases, because multiple independent variables are needed to describe the dependent variable, *multi-linear regression* is used to fit the observed y to a linear combination of the x's:

$$y = \beta_0 + \sum_{j=1}^{M} \beta_j x_j + \varepsilon \ , \tag{1.11}$$

where, x_j and β_j represent the independent variables and regression coefficients respectively and ε is an error term that accounts for any additional factors outside the original independent variables.

In order to make model predictions and investigate how covariates influence dependent variable predictions, regression coefficients must be determined. A straightforward method to determine these variables is through ordinary least squares (OLS) regression, which minimizes the sum of the residual errors [64]. By rearranging Eq. (1.11), the residual errors can be expressed as

$$S_r = \sum_{i=1}^{N} \left(y_{i,measured} - y_{i,predicted} \right)^2 = \sum_{i=1}^{N} \left(y_{i,measured} - \beta_0 + \sum_{j=1}^{M} \beta_j x_{i,j} \right)^2 \tag{1.12}$$

Here, $y_{i,measured}$ and $y_{i,predicted}$ represent the measured dependent variable and the model prediction from Eq. (1.11) for each i^{th} observation, respectively.

Minimizing the residual errors by setting the partial derivative of each independent variable to zero, Eq. (1.12) can be rearranged to solve for the $\hat{\beta}$, the vector that minimizes S_r [63]:

$$\hat{\beta} = \left(X^T X \right)^{-1} \left(X^T Y \right) \tag{1.13}$$

In this formulation, X is the matrix of independent variables resulting in the Y vector of observations. The above expression depends on the underlying model to be linear. In these cases, multi-linear regression is useful in determining covariate dependence and making basic

pharmacokinetic predictions based on given observations. Many standalone Python [65–67], and R [68] packages have been developed to determine coefficients for this type of multi-linear regression.

1.3.3.2 Non-linear least squares

While the method discussed above is appropriate for investigating covariate dependencies and performing basic predictions for linear models, the processes governing most pharmacokinetic and pharmacodynamic processes are best described by non-linear equations. To solve for parameters in this realm, non-linear regression focuses on minimizing the residual error between observed value and predicted value. This is accomplished by defining the nonlinear model as $f(x_i; a_0, a_{1,\ldots,}a_n)$ where x_i represents the independent variable(s) and a_0 through a_n are the parameters to be fit to the data. Using this model, an objective function is defined as

$$obj = \sum_{i=1}^{m} \left[y_i - f\left(x_i; a_0, a_1, ..., a_n\right) \right]^2 , \tag{1.14}$$

where y_i are the observed values and the sum of the squares of the residual is calculated through evaluation of the proposed model for each observation's independent variable. While the basis of this method is straightforward, exploring the parameter space and determining a *global* minimum for the objective function can prove difficult. Many standalone applications and python packages [66,69,70] use sophisticated algorithms to explore the parameter space and minimize the objective function.

1.3.3.3 Bayesian Inference

One of the most flexible methods for parameter estimation is Bayesian inference. The Bayesian approach relies on the relationship between probability distributions involving unknown parameters (θ) and data made available through observations (y) which are linked through Bayes' theorem:

$$p(\theta \mid y) \propto p(\theta)\, p(y \mid \theta) \tag{1.15}$$

Here, the posterior distribution, $p(\theta \mid y)$, is obtained by the product of the prior distribution, $p(\theta)$, and the likelihood, $p(y \mid \theta)$. The parameters, θ, all have biological significance and knowledge of the initial parameter distribution, such as the mean, variance, and range, is used to determine the prior (or initial) distribution on each parameter. The data, y, corresponds to experimentally observed biological response profiles following a known exposure. The likelihood contains the underlying model equations calculated with parameters, θ where $p(y \mid \theta)$ is determined through comparison of the predicted probability distribution for y with the observed probability distribution, i.e measured concentrations containing population variability and measurement error. Biological models can be either a PBPK model for pharmacokinetic predictions or a system of pharmacodynamic model equations. Bayesian inference will return the probability distribution of the parameter of interest from these models.

To arrive at the posterior parameter distributions, Markov chain Monte Carlo (MCMC) methods generate a sequence of random draws from the prior probability distributions for the given parameter and accept or reject these draws based on the calculated joint posterior distribution [71]. The most common method for creating the Markov chain is through the Metropolis-Hasting (MH) algorithm [72]. Here, an initial θ_0 is sampled from a proposal distribution. This distribution is independent of the prior, and is generally symmetric, such as a Gaussian or uniform distribution, and is centered about the previous draw of θ. The first parameter, θ_0 - the initial parameter for the chain - serves as a basis for comparison for the next iteration. The candidate parameter, θ_c, is then sampled from the current proposal distribution. For example, if a symmetric distribution, such as a Gaussian, is used for the proposal distribution,

then $\theta_c = \theta_0 + N(0, \sigma)$. Acceptance of this candidate point follows a series of steps [71]. First, the acceptance ratio is determined using the calculated posterior distribution:

$$r = \frac{p(\theta_c)\, p(y \mid \theta_c)}{p(\theta_0)\, p(y \mid \theta_0)}, \tag{1.16}$$

where the numerator is the candidate posterior probability distribution and the denominator is the previous step's posterior distribution. If $r \geq 1$, θ_c is accepted outright and becomes the next the new θ_0 for the next iteration. If $r < 1$, θ_c is accepted only if r is greater than a random draw for a uniform distribution: $U(0,1)$. Otherwise, θ_c is rejected and θ_0 remains the current parameter for the Markov chain. After a sufficient number of iterations to achieve convergence in the θ_i chain [73], the final N iterations of the Markov chain represent the posterior probability distribution: $p(\theta \mid y)$.

Because a central tenet of Bayesian inference involves updating prior knowledge of a parameter based on observed data, prior distributions can be set based on the current scientific literature with these prior observations serving as a reference point for calibrating the PBPK model [74]. Additionally, Bayesian inference can be used to determine population parameter distributions where the intra- and inter-individual variability is separated from model uncertainty [36,74].

Though there are several software applications capable of providing a framework for Bayesian inference and MCMC analyses, including PyMC [75] and JAGS [76], the primary software package used throughout this work was MCSim [77], which contains flexible capabilities for standard PBPK, Monte Carlo, and MCMC modeling.

CHAPTER 2

PROJECT OVERVIEW

The research described in this dissertation builds upon previously developed computational methods as a basis for the design and implementation of novel *in silico* approaches to describe biological processes following administration of a pharmaceutical drug or exposure to an environmental toxicant. Central to all of the projects described herein is the application of computational models to solve real-world xenobiotic exposure problems; specifically optimization of tuberculosis drug therapy, determination of acetaminophen disposition resulting from overdose, prediction of adverse health outcomes from organophosphate insecticide exposure, and development of benchmark response modeling for trichloroethylene-mediated hypersensitivity.

This chapter provides an overview of each project and how tools and methods were developed to solve a given problem. The common themes throughout this research were (i) utilization of *in vivo* and *in vitro* experimental results to develop novel biological models to describe the pharmacokinetics and/or pharmacodynamics of a system and (ii) application of computational models to make biologically relevant predictions to guide future experimental studies.

2.1. A PHYSIOLOGICALLY-BASED PHARMACOKINETIC MODEL OF RIFAPENTINE AND 25-DESACETYL-RIFAPENTINE DISPOSITION IN HUMANS

Tuberculosis (TB) is a common and often fatal infectious disease caused by various strains of mycobacteria, usually *Mycobacterium tuberculosis* (MTB). In 2014, 9.6 million people fell ill with TB and 1.1 million died from the disease [78]. Because current drug therapies for TB

are long, complex, burdensome for patients, and may not be effective against certain strains of MTB, new anti-TB drugs are needed [78,79]. Currently, anti-TB dosing regimens consist of three to four antibacterial drugs administered over six to nine months with each drug targeting a different aspect of TB replication. Traditionally, this combination of first-line agents contains a rifamycin derivative which serves as a potent inhibitor of prokaryotic RNA polymerase within MTB [80], with the current drug of choice being rifampicin (RIF) [81]. However, owing to an increased prevalence of multidrug-resistant (MDR) tuberculosis and the recognition that shorter treatment regimens are essential, there is a constant search for more effective drugs [79].

One such drug, as a candidate to replace RIF within the first-line combination therapy, is rifapentine (RPT) [79,82], whose metabolite 25-desactyl-rifapentine (dRPT), has also demonstrated activity against MTB *in vitro* [8]. Although results from a number of studies indicate that rifapentine has the potential to shorten treatment duration and enhance completion rates compared with other rifamycin agents utilized in anti-tuberculosis drug regimens [83–86], its tissue-level absorption, distribution, metabolism and excretion (ADME) in humans are unknown. This information is a critical element in creating dosing regimens and therapies that maximize efficacy while minimizing toxicity to the patient.

To help inform such an optimization for this rifamycin drug candidate, the goal of the work detailed in Chapter 3 was to develop and utilize a physiologically-based pharmacokinetic (PBPK) model to predict tissue-specific concentrations of RPT and dRPT in humans [87]. Starting with the development and verification of a PBPK model for rats, the model was extrapolated and then tested using human pharmacokinetic data. Testing and verification of the models included comparisons of predictions to experimental data in several rat tissues and time-course RPT and dRPT plasma concentrations in humans from several single- and repeated-

dosing studies. Finally, the model was used to predict RPT concentrations in the lung during the intensive and continuation phases of the currently recommended TB treatment regimen. Overall, the major outcome of this work is a methodology for evaluating dosing regimens for RPT and for predicting tissue-level concentrations that could be predictors of problems related to efficacy or safety.

2.2. Characterization of the Disposition of Acetaminophen Through Development and Application of a Novel PBPK Model

Acetaminophen (*N*-acetyl-para-aminophenol, paracetamol, APAP) is one of the most widely used analgesics and antipyretics in the world. It is a well-known hepatotoxicant and, owing to its ubiquitous usage, is the principal cause of acute liver failure in both the United States [88,89] and the United Kingdom [88,90]. APAP is metabolized primarily by sulfation through conjugation with 3'-phosphoadenosine-5'phosphgosulfate (PAPS) cofactor and glucuronidation through conjugation of uridine diphosphate glucuronic acid (UDPGA). However, APAP can also be oxidized by CYP isozymes to form the reactive metabolite, and putative mediator of toxicity, N-acetyl-*p*-benzoquinonimine (NAPQI). Characterizing and quantifying the role of these pathways and the formation and clearance of key metabolites can be facilitated by the use of predictive models that incorporate salient biochemical and physiological phenomena in a tissue-specific manner. In addition, such models can include differences in parameters related to absorption and metabolic pathways indicative of differences between genetically different populations. Currently, predictions of APAP pharmacokinetics are based on models that were developed using limited experimental data in humans, which may be misleading for populations with atypical metabolic capacities for APAP. Moreover, current models lack predictive capabilities for overdose scenarios (> 7000 mg or > 90 mg/kg of APAP

over 24 hours) and have no capabilities to estimate the administered dose, important information in the personalized treatment and follow-up for affected patients.

Broken into three subchapters (§3.1-3.3), the acetaminophen modeling work included the development and utilization of a physiologically-based pharmacokinetic model to describe APAP pharmacokinetics in humans using physiologically realistic descriptions of the non-ideal absorption and metabolism seen with this commonly used drug. This computational modeling work was accomplished through three main components; (i) development of a population-based PBPK model to describe APAP ADME under therapeutic dosing conditions [36], (ii) use of a hierarchical Bayesian population model to quantify ADME differences between genetically different sub-population [40], and (iii) development of a computational method for reconstructing initial APAP dose following an overdose [39].

2.2.1. Physiologically based modeling of the pharmacokinetics of acetaminophen and its major metabolites in humans using a Bayesian population approach

The first aspect of this work focused on development and application of a PBPK model to predict and characterize the ADME of acetaminophen in humans under therapeutic dosing conditions [36]. This model incorporated pharmacologically and toxicologically-relevant tissue compartments along with mechanistic descriptions of the absorption and metabolism of APAP, such as gastric emptying time, cofactor enzyme kinetics, and transporter-mediated movement of conjugated metabolites in the liver. Through the use of a hierarchical Bayesian framework unknown model parameters were estimated using a large training set of data from human pharmacokinetic studies, resulting in parameter distributions that account for data uncertainty and inter-study variability. Predictions from the model showed good agreement with a diverse test set of data across several measures, including plasma concentrations over time, renal

clearance, APAP absorption, and pharmacokinetic and exposure metrics. The utility of the model was then demonstrated through predictions of cofactor depletion, dose response of several pharmacokinetic endpoints, and the relationship between APAP marker levels in the plasma and those in the liver.

2.2.2. Characterizing the effects of race/ethnicity on acetaminophen pharmacokinetics using physiologically-based pharmacokinetic modeling

Using the validated therapeutic PBPK model noted above (§2.2.1), genetic differences in APAP pharmacokinetics were investigated using a hierarchical Bayesian population modeling approach [40]. The objective of this study was to develop subpopulation-specific PBPK models for two genetically different groups (Western Europeans and East Asians) and then use the models to quantify the differences in APAP ADME between these two groups. First, a comprehensive data set for APAP pharmacokinetics (PK) was divided into two groups based on ethnicity of the subjects as an indicator of the expected abundance of their phenol-metabolizing alleles. Next, using these datasets and a Bayesian hierarchical framework, subpopulation-specific PBPK models for APAP were developed and tested for these two groups. Finally, using the validated models, differences in ADME were characterized between the two groups with respect to various PK measures, including urinary excretion and APAP area under the curve (AUC) in the liver. Although not dramatic at therapeutic dosing levels, these results demonstrated a divergence in the liver-specific APAP concentrations and AUC between the two groups and suggested that differences in glucuronidation capacity may play a role in this disparity and ultimately lead to differences in liver APAP concetrations at higher administered doses, such as in cases of overdose.

2.2.3. A novel approach for estimating ingested dose associated with acetaminophen overdose

To better understand the ADME of APAP under overdose conditions, the previously described therapeutic APAP PBPK model was scaled up to an overdose scenario using mechanistically accurate drug dissolution kinetics to simulate a solid to aqueous phase change of drug in the stomach and the resulting absorption into the body [39]. This new model was developed to address three objectives: (i) prediction of tissue-level concentrations of APAP under overdose conditions, (ii) provide a clinically-useful methodology for estimating the administered APAP dose following the ingestion of a potentially harmful APAP overdose, and (iii) elucidating the effect of blood sampling time and additional biomarker measurements on reconstructing the APAP dose. The overall outcome of this work is a methodology to help inform individualized overdose treatment and follow-up plans for patients based on an individual patient's serum sample data anthropometric and physiological information.

2.3. Development of Environmental Public Health Indicators and a new Benchmark Dose for Chlorpyrifos using a Health-Based Endpoint

Organophosphate (OP) insecticides are among the most widely used synthetic chemicals for the control of agricultural and domestic insect pests. Of the 93 million pounds of insecticides used in the United States every year, 35% are OP insecticides, which amounts to 33 million pounds used each year [91]. The primary mechanism of action of OP insecticides is the inhibition of acetylcholinesterase (AChE) by active oxon metabolites, resulting in the accumulation of the acetylcholine neurotransmitter within the cholinergic synapses. Risk assessments aimed at protecting human health have focused primarily on point-of-departure (PoD) studies to determine benchmark doses (BMD) resulting in a given benchmark response

(BMR), i.e. target percent cholinesterase inhibition [92,93]. While AChE inhibition in the brain represents an actual measure for cholinergic toxicity, it may not necessarily be the most sensitive endpoint for overall OP toxicity.

To investigate more sensitive measures of OP toxicity, studies in animals and humans have attempted to characterize various cognitive deficits associated with low-dose, chronic exposure to OP's [94–96]. Within these analyses, the involvement of OP insecticide exposure is determined to contribute to deficits in learning and memory within exposed human cohorts, and studies in rats have demonstrated adverse health outcomes from OP exposure, specifically with respect to attention and spatial memory deficits [97–100].

The work presented in this section of the dissertation (Chapter 5) centered on determining a benchmark dose associated with cognitive deficits in humans and characterizing related biomarkers that could be used as environmental public health indicators (EPHIs). To achieve this aim, a methodology was developed that made use of a well-validated PBPK/PD model and a novel dose-response model for one such OP, chlorpyrifos (CPF) [48]. Similar to AChE PoD animal studies, this work utilized cognitive deficit studies in rats and linked these deficits to a steady-state internal-dose-metric (CPF concentrations in the brain). Overall, the outcome of this work was (i) a tool for calculating benchmark doses from measurable cognitive deficits, (ii) the development of a new, more sensitive, benchmark dose for CPF exposure, and (iii) correlation of CPF biomarkers of exposure to cognitive deficit endpoints.

2.4. Modeling Toxicodynamic Effects of Trichloroethylene on Liver in Mouse Model of Autoimmune Hepatitis

Trichloroethylene (TCE) is a chlorinated hydrocarbon that has been used as a popular degreasing agent since the 1920s. While a carcinogen at higher doses, one of the predominant

non-cancer endpoints from chronic exposure to the industrial solvent is immunotoxicity, most notably the progression of autoimmune hepatitis (AIH) [101–104]. TCE is still widely used throughout the world, and due to poor disposal methods, is an abundant groundwater contaminant and represents the putative cause of systemic hypersensitivity diseases often accompanied by immune-mediated hepatitis [105].

To address the issues surrounding AIH progression following low-dose chronic exposure to TCE in drinking water, multiple *in vivo* studies in mice have demonstrated T-cell mediated liver disease similar to that found in human AIH. To help elucidate the biological basis for this phenomenon, Gilbert et al. [42] studied the effect of TCE macrophage cytokines and demonstrated that this toxicant inhibits the production of interleukin-6 (IL-6), which is necessary for normal hepatocyte turnover and protection of the liver against pro-inflammatory events. In related studies, these investigators characterized liver histopathology following chronic exposure to TCE in drinking water for mice, providing a time-dependent metric for liver tissue damage as a result of TCE exposure.

Despite these and other experimental studies, the specific TCE-mediated mechanism of toxicity resulting in progression of AIH was still unknown. In addition, linkages between the dose-dependent decrease in both transcriptional and protein levels and the resulting observed liver pathology are unknown. In order to fill this gap between experimental results and the AIH endpoint of interest, a mechanistically-based mathematical model was developed to test a hypothesized mechanism of toxicity and predict doses that lead to observed hypersensitivity.

As an initial step in understanding the effects of TCE exposure on AIH progression, a pharmacodynamic model, also known as a toxicodynamic model, was developed to quantify the relationship between immune system signaling and cellular events in the liver of TCE-treated

mice; more specifically, the model was aimed at quatifying the role of IL-6 as a maintenance mechanism and predicting downstream events such as liver pathology following disruption of this IL-6 repair pathway owing to TCE exposure. By incorporating results from *in vivo* experiments and *in silico* toxicodynamic simulations, this study supported the hypothesis that TCE-induced liver pathology was associated with the suppression of hepatoprotective cytokines, such as IL-6, and not due to an increase of pro-inflammatory events. Aside from a useful predictive model, a major outcome of this study was the determination of a benchmark TCE dose eliciting a desired benchmark response level, i.e. mild inflammation of the portal regions of the liver.

CHAPTER 3

A PHYSIOLOGICALLY-BASED PHARMACOKINETIC MODEL OF RIFAPENTINE AND 25-DESACETYL-RIFAPENTINE DISPOSITION IN HUMANS

3.1 INTRODUCTION

Rifapentine (RPT) is a rifamycin-class antibiotic indicated for the treatment of pulmonary tuberculosis (TB) caused by *Mycobacterium tuberculosis* (MTB) and in the treatment of latent TB infection in patients at high risk of progression to TB disease. RPT has a longer half-life, increased affinity to serum protein binding [106], and lower minimum inhibitory concentration (MIC) against MTB than rifampin, which is currently used as part of several first-line TB treatment regimens [84,107]. Moreover, the primary metabolite for RPT, 25-desacetyl-rifapentine (dRPT), has also been found to be active against MTB, although at markedly lower mean inhibitory concentrations [8,106,107]. Because of these characteristics, RPT has been the subject of a number of clinical pharmacology studies aimed at evaluating pharmacokinetics and developing effective therapies [83,85,108–116]. Although data from these investigations are valuable in their own right, mathematical modeling offers a way to complement these studies, synthesize their disparate data, and provide the clinician an additional tool to characterize and predict the absorption, distribution, metabolism, and excretion (ADME) of RPT under dosing conditions of interest.

One of the very few such mathematical models was developed by Savic et al. [86] who used a classical compartmental modeling approach to assess human population pharmacokinetics of both RPT and dRPT. This model described the absorption, metabolism, and clearance of these

This work was performed jointly with the full list of co-authors in [32].

two species and accurately predicted their time-course plasma concentrations in healthy volunteers. Unfortunately, compartmental concentrations in this model were not directly relatable to those in actual tissues of interest (e.g., the lung and liver) because the effects of plasma protein binding and blood-tissue partitioning of the parent drug and metabolite were not included. Moreover, because the study utilized data from healthy subjects, the effects of the disease on pharmacokinetic outcomes could not be characterized.

A finer-grained approach that specifically includes relevant physiological and biochemical effects and processes and facilitates examination of organ or tissue-level pharmacokinetics is physiologically-based pharmacokinetic (PBPK) modeling. Regrettably, few PBPK models have been developed for anti-TB drugs, let alone RPT. Using targeted experimental data in mice, Reisfeld et al. [117] developed a PBPK model to describe the biodistribution of the second-line TB agent, capreomycin, and because capreomycin is nephrotoxic [118], PBPK modeling allowed for tissue-specific concentration predictions at both the site of action for the antibiotic effect, the lung, and the site of potential toxicity, the kidney. Subsequently, Lyons et al. [38] used a rich set of literature data to create a PBPK model to describe the disposition of rifampin which, as noted earlier, is a first-line agent in current therapies for TB. Although the above models are useful in simulating and comparing the disposition of anti-TB drugs in tissues of interest, they were developed using data from rodents and currently have limited applicability to humans.

To begin to address this gap, the principal aims of this study were to (i) develop a PBPK model to predict the ADME for rifapentine and its active metabolite in humans, (ii) test the model against available human study data, and (iii) make tissue-specific predictions of concentrations of RPT and dRPT in the lung and compare those to the MIC. This latter aim is

particularly relevant because current dosing recommendations for anti-TB drugs are guided by knowledge of the unbound concentration of the agent in the plasma and by comparing this free fraction to the known MIC against MTB [114]. Because this plasma concentration may not accurately reflect that in the lung, the recommended dose may not provide the desired level of antibiotic effect.

3.2 Materials and Methods

3.2.1 Approach

To achieve the study aims, two PBPK models were developed, parameterized, and tested: one specific to the rat (R-PBPK) and another for humans (H-PBPK). The models shared the same compartmental structure and set of governing equations (§3.4), with differences only in the parameter values, principally related to physiology and metabolism. Starting with development of the R-PBPK, tissue specific pharmacokinetic data were used to compute key drug-tissue properties (e.g., partition coefficients) that were later utilized in the H-PBPK. Ultimately, both the R-PBPK and H-PBPK were parameterized and verified using relevant sets of training and test data. Further details are given below.

3.2.2 Experimental data

TABLE 3.1. Studies containing pharmacokinetic data for humans following oral dosing of rifapentine

References	Dose	Regimen: single dose (S) or repeated dose (R)	TB Infected	Number of subjects (sex)
Data used for parameter estimation				
Weiner, 2004 (14)	1200 mg 900 mg 600 mg	R: once weekly	Yes	35 (M/F)
Data used for model testing/verification				
Dooley, 2008 (16)	900 mg	R: three times weekly	No	15 (M/F)
Dooley, 2012 (3)	1200 mg 900 mg 600 mg	S R: daily dosing	No	5 (M/F)
Keung, 1998 (11)	600 mg	S	No	20 (M/F)
Keung, 1998 (9)	600 mg	S	No	20 (M)
Keung, 1998 (8)	600 mg	S	No	15 (F)
Keung, 1999 (10)	600 mg 300 mg 150 mg	S R: daily dosing	No	23 (M)
Langdon 2004 (12)	600 mg 750 mg 900 mg	R: daily dosing, 4 days	Yes	46 (M/F)
Reith, 1998 (15)	600 mg	S	No	4 (M)

Pharmacokinetic data for RPT in rats were obtained from the work of Assandri et al. [119], which provided (i) drug concentrations in the plasma under multiple dosing conditions, (ii) concentrations obtained from homogenates of several relevant tissues following oral dosing, and (iii) the fraction of drug bound to plasma proteins over time. For development of the human model, a comprehensive review of the literature was conducted to identify pharmacokinetic studies where RPT was administered to adults as either a single dose or via repeated doses. Emphasis was placed on studies in which concentrations of both parent RPT and its metabolite dRPT were quantified because these coincident data could be used in the estimation of relevant metabolism and dRPT-specific parameters. As shown in Table 3.1, these data were divided into two parts: a 'training' set used to determine unknown model parameters and a 'validation' set, used to test and verify the model predictions.

3.2.3 PBPK models

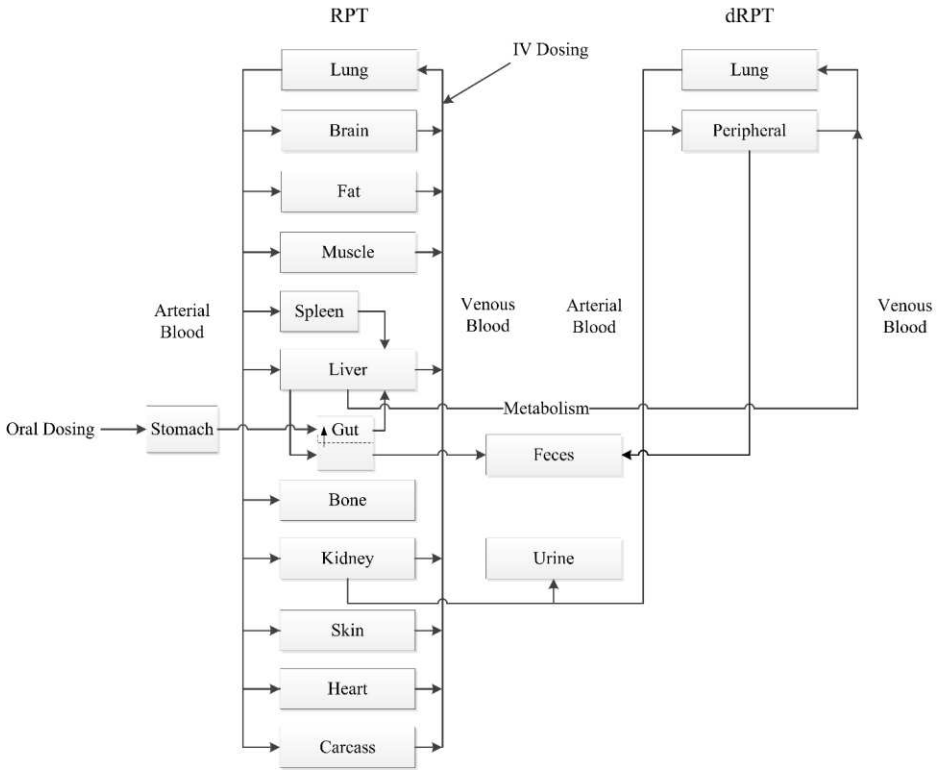

FIGURE 3.1. PBPK model structure

The common PBPK model structure is shown in Figure 3.1. The model comprises a set of compartments for RPT, identical to those used previously for rifampin [38], integrated with a simpler structure for the metabolite, dRPT, which consisted of only the lung and a *lumped* peripheral compartment. The compartmental species mass balance equations are similar to those used in this prior study with the exception of the description of oral absorption fraction for the parent compound and the explicit quantitation of the metabolite concentration over time described below.

Consistent with the experimental results from Assandri *et al.* [119], oral absorption was specified to be dose dependent. In particular, the following form was used to describe the oral fraction absorbed, F_a:

$$F_a = \frac{F_{a,k}}{D + F_{a,k}}, \tag{3.1}$$

where D is the oral dose and $F_{a,k}$ represents a constant to be fit from the data.

Because the metabolite dRPT is active against MTB and its level has been measured in several studies in humans, the present model included equations to explicitly track its rate of formation and distribution over time. The deacetylation reaction to transform RPT to dRPT in the liver for humans was assumed to follow Michaelis-Menten kinetics [120],

$$v = \frac{V_M C_{liver}^{RPT}}{K_M + C_{liver}^{RPT} + \frac{{C_{liver}^{RPT}}^2}{K_I}}, \tag{3.2}$$

where v is the rate of RPT deacetylation, V_M, K_M, and K_I represent the maximum reaction rate, the Michaelis-Menten constant, and the substrate inhibition constant for RPT deacetylation, respectively. While its mechanism of action is currently unknown, *in vitro* studies have demonstrated the activity of dRPT against MTB [8], and because this species may exhibit similar

antibiotic effects *in vivo*, its disposition may be of interest when characterizing anti-TB therapies involving RPT. Interestingly, although the levels of dRPT are quantifiable in humans following RPT administration [85,108–112,114–116], similar studies in rats have shown that this chemical is undetectable in the plasma [119]. Consistent with this observation, the metabolic transformation of RPT to dRPT was not included in the R-PBPK.

Lastly, rather than using *in vitro* results for RPT and dRPT protein binding, unbound fractions for this PBPK model were calculated using results from TB infected patients following RPT dosing [121].

3.2.4 Parameter estimation

Parameters in the governing PBPK model equations were taken from the literature or were estimated using the procedures described below.

3.2.4.1 Physiological parameters

Physiological compartment volumes and blood flow rates for human and rat were obtained from Brown et al. [55]. Compartment volumes were scaled linearly with body weight, blood flow rates were scaled with body weight to the 0.75 power [45], and the coefficient of variation for each organ volume and arterial blood flow rate was set at 0.2 and 0.3, respectively [38,122]. The resulting physiological parameters for each compartment are summarized in Table 3.2.

TABLE 3.2. Physiological and anatomical parameters

Parameter (units)	Abbreviation	Mean		Coefficient of Variation
		Rat	Human	
Body Weight (kg)	BW	0.23	65	0.16
Cardiac Output ($L/h/kg^{0.75}$)	QCC	14.1	16.2	0.2
Compartment				
Lung	Q_{LUC}	14.1	16.2	0.3
	V_{LUC}	0.005	0.0076	0.2
Brain	Q_{BRC}	0.02	0.12	0.3
	V_{BRC}	0.0057	0.02	0.2
Fat	Q_{FC}	0.07	0.0675	0.3
	V_{FC}	0.07	0.2142	0.2
Heart	Q_{HC}	0.049	0.045	0.3
	V_{HC}	0.0033	0.0047	0.2
Muscle	Q_{MC}	0.278	0.145	0.3
	V_{MC}	0.4043	0.4	0.2
Bone	Q_{BC}	0.122	0.05	0.3
	V_{BC}	0.073	0.1429	0.2
Skin	Q_{SKC}	0.058	0.05	0.3
	V_{SKC}	0.1903	0.0371	0.2
Kidney	Q_{KC}	0.141	0.18	0.3
	V_{KC}	0.0073	0.0044	0.2
Spleen	Q_{SC}	0.01	0.01	0.3
	V_{SC}	0.002	0.0026	0.2
Gut	Q_{GC}	0.14	0.14	0.3
	V_{GC}	0.027	0.0171	0.2
Liver	Q_{LAC}	0.024	0.06	0.3
	V_{LC}	0.0366	0.0257	0.2
Carcass	Q_{CRC}	0.088	0.1325	0.3
	V_{CRC}	0.1015	0.0448	0.2
Venous Blood	V_{BLVC}	0.0493	0.0526	0.2
Arterial Blood	V_{BLAC}	0.0247	0.0263	0.2

3.2.4.2 Partition coefficients

With data for the free concentration of RPT in the plasma [119], mean values for the tissue:blood partition coefficient, $P_{T:blood}$, were determined using the following equation:

$$P_{T:blood} = \frac{1}{BP}\left(\frac{C^{RPT}_{tissue}}{C^{RPT}_{plasma,f}}\right),$$

where *BP* is the blood:plasma partition coefficient, and C^{tissue}_{RPT} and $C^{plasma,f}_{RPT}$ are the measured tissue and free plasma concentration of RPT, respectively. Tissue:plasma partition coefficients were computed for all model compartments based on time-course tissue concentration data [119] using points during the elimination phase at which equilibrium had been reached in drug concentration between the tissue and the venous blood.

3.2.4.3 Other model parameters

To include the effect of data uncertainty and inter-study variability on model outputs, unknown parameters were estimated within a Bayesian hierarchical context [36,39,123]. Within this context, parameters were estimated by first computing partition coefficients and other relevant parameters for the R-PBPK and then using these parameter distributions as 'priors' in the estimation of the human-specific parameters.

3.2.5 Simulation methodology and computing platform

Once the parameter distributions had been computed, a Monte Carlo approach was used to generate a large family of simulation results that would account for inter-study variability and data uncertainty. These results were then aggregated and processed to yield mean and 95% prediction intervals for pharmacokinetic outcomes of interest.

Data from the literature were digitized using DigitizeIt v.1.5.8 [124]. Simulations of the PBPK governing equations, including the Bayesian Markov chain Monte Carlo and resulting model evaluation were conducted in MCSim v5.4 [77]. Processing, analysis, and visualization of data were carried out using scripts written in Python v2.7.2 [125] utilizing the numpy [126], scipy [66], and matplotlib [127] packages. All computations were performed on a compute

cluster running the 64 bit CentOS Linux operating system on six gigabit-linked Dell 2950 servers, each containing two quad-core 2.5 GHz Xeon processors and 64 GB of RAM.

3.3 RESULTS

3.3.1 Model parameter values

Using the procedures and data detailed above, distributions for unknown model parameters were estimated.

The resulting parameters (posterior distributions) for both rat- and human-specific models are listed in Table 3.3.

3.3.2 Testing and verification of the rat-specific model (R-PBPK)

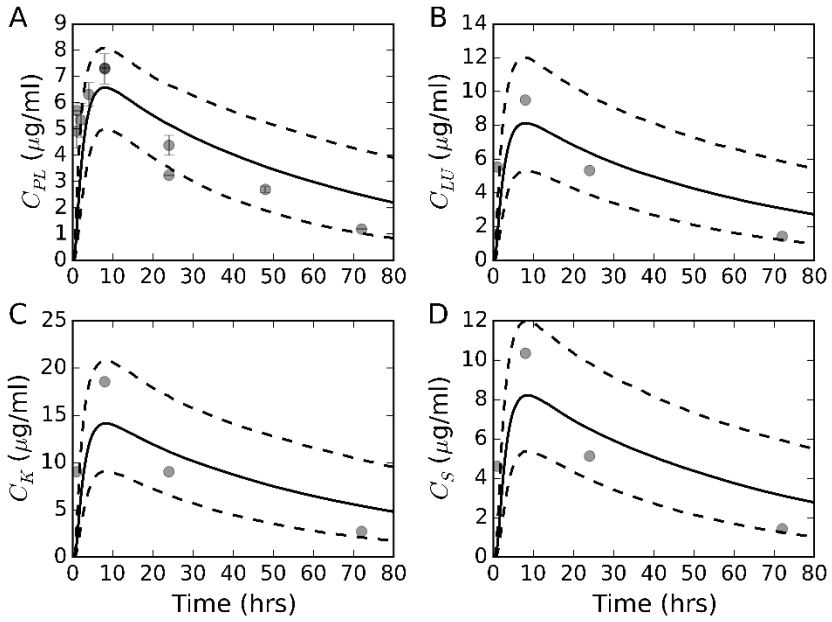

FIGURE 3.2. Simulations of rifapentine pharmacokinetics following a 10 mg/kg oral dose in the rat, showing concentration profiles in the plasma (A), lung (B), kidney (C), and spleen (D). Solid and dashed lines represent the simulated mean and 95% prediction intervals, respectively; while transparent circles represent the training set data from Assandri et al. [119]

TABLE 3.3. Physicochemical, biochemical, and clearance-related parameters

Description	Parameter (units)	Rat			Human		
		Prior	Posterior	Source	Prior	Posterior	Source
Fraction bound							
RPT	$f_{b,R}$	-	0.97	(20)	-	0.994	(22)
dRPT	$f_{b,D}$	-	-	-	-	0.976	(22)
Absorption							
Fractional absorption constant	$F_{a,k}$	U(1, 1000)	N(27, 0.21)	-	N(27, 0.21)	N(21.23, 0.16)	Rat
Oral absorption rate	k_{SG} (1/h)	N(0.31, 0.2)	N(0.30, 0.06)	(20)	N(0.30, 0.06)	N(0.33, 0.18)	Rat
Gut lumen reabsorption	k_{GLG} (1/h)	N(0.17, 0.3)	N(0.17, 0.06)	(19)	N(0.17, 0.06)	N(0.17, 0.06)	Rat
Total blood clearance							
RPT	CLC_R (L/h-$BW^{0.75}$)	U(0.01, 10)	N(0.74, 0.31)	-	N(0.74, 0.31)	N(0.64, 0.18)	Rat
dRPT	CLC_D (L/h-$BW^{0.75}$)	-	-	-	U(0.001, 100)	N(0.07, 0.28)	-
Fractional renal clearance	f_R	-	0.13	(20)	-	0.13	Rat
Deacetylation							
	$V_{max}C$ (μmol/h-$BW^{0.75}$)	-	-	-	U(0.01, 100)	N(0.97, 0.22)	(21)
	K_M (μmol)	-	-	-	N(37.1, 0.2)	N(34.29, 0.16)	
	K_I (μmol)	-	-	-	N(174, 0.2)	N(168.07, 0.17)	
Partition Coefficients							
Lung	P_{LU}	N(48.9, 0.2)	N(48.48, 0.17)	(20)	-	N(48.48, 0.17)	-
Brain	P_{BR}	N(5.93, 0.2)	N(5.81, 0.17)		-	N(5.81, 0.17)	
Fat	P_F	N(79.8, 0.2)	N(78.67, 0.17)		-	N(78.67, 0.17)	
Heart	P_H	N(63.9, 0.2)	N(62.02, 0.18)		-	N(62.02, 0.18)	
Muscle	P_M	N(38.1, 0.2)	N(37.39, 0.17)		-	N(37.39, 0.17)	
Bone	P_B	N(28.3, 0.2)	N(27.33, 0.18)		-	N(27.33, 0.18)	
Skin	P_{SK}	N(43.5, 0.2)	N(43.22, 0.17)		-	N(43.22, 0.17)	
Kidney	P_K	N(88.7, 0.2)	N(87.47, 0.17)		-	N(87.47, 0.17)	
Spleen	P_S	N(49.9, 0.2)	N(49.71, 0.17)		-	N(49.71, 0.17)	
Gut	P_G	N(42.1, 0.2)	N(38.69, 0.18)		-	N(38.69, 0.18)	
Liver	P_L	N(183.3, 0.2)	N(164.21, 0.18)		-	N(164.21, 0.18)	
Carcass	P_{CR}	N(28.3, 0.2)	N(29.04, 0.18)		-	N(29.04, 0.18)	
Peripheral	P_P	-	-	-	U(0.1, 200)	N(5.50, 0.29)	-

N(*a*, *b*) denotes a normal distribution with a mean of *a* and fractional coefficient of variation, *b*; U(*a*, *b*) represents a uniform distribution bounded by the minimum (*a*) and maximum (*b*); a single number in the *posterior* column represents no distribution. When "Rat" is specified as the source, the posterior mean used in the R-PBPK (with a fractional CV of 0.3) was used as the prior distribution for the H-PBPK.

Using the computed parameters for the R-PBPK, simulations were conducted and compared to *in vivo* time-course concentration values from a literature study [119] that detailed plasma and tissue pharmacokinetics following a single 10 mg/kg oral dose in the rat. This comparison is illustrated in Figure 3.2, which shows experimental data (points) and predicted mean (solid line) and 95% prediction intervals (dashed lines) for the PBPK model.

3.3.3 Testing and verification of the human-specific model (H-PBPK)

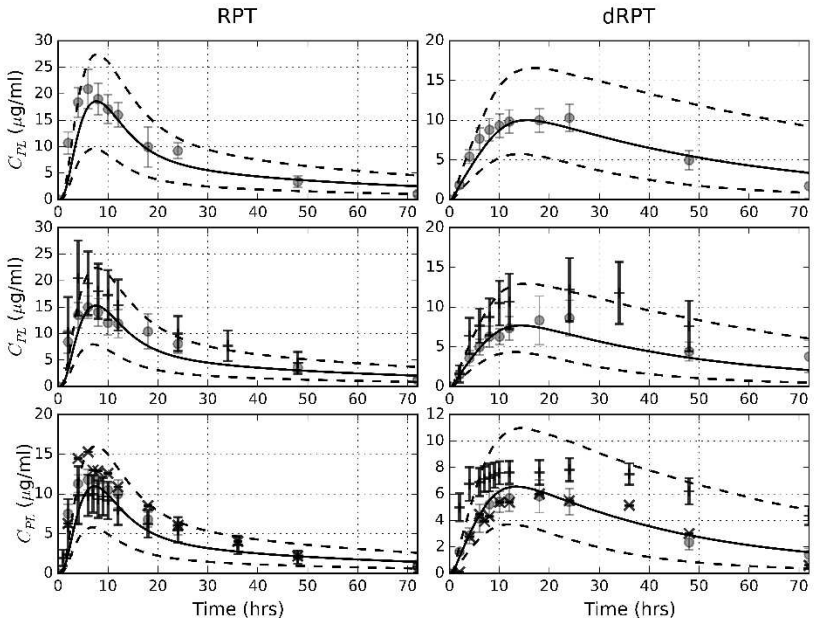

FIGURE 3.3. Comparison of simulation results to human plasma concentration data for RPT and dRPT following oral administration of 600, 900, and 1200 mg oral RPT doses. Training set data are shown as transparent circles (o), while data from the validation set are shown as dark x's.

Throughout the studies, training set data were used for parameter estimation (model calibration) while verification data were used for model evaluation [36]. Using the set of parameters listed in Table 3.2 and Table 3.3, simulations were run for 600, 900, and 1200 mg single oral doses of RPT and compared to the corresponding dose training and verification data referenced in Table 3.1. Figure 3.3 shows the results of these comparisons for both RPT and

dRPT in the plasma over multiple studies. The range of the experimental doses shown in this figure match those in a standard treatment regimen for TB treatment [106,128]. These comparisons show that the experimental data fall within the 95% prediction intervals, indicating that the model can accurately predict the pharmacokinetics of the drug and account for the variance in this measure across the population sampled.

TABLE 3.4. Computed pharmacokinetic measures for rifapentine

Parameter	**Symbol (units)**	**Model Prediction**	**Experiment***
maximum plasma concentration	C_{max} (μg/ml)	15.48 (21)	15.2 (30)
drug half-life	$t_{1/2}$	10.92 (14)	12.03 (20)
area under the curve from time 0 extrapolated to infinity	$AUC_{0-\infty}$ (μg-h/ml)	382.19 (25)	380.63 (31)
apparent oral clearance	CL/F (L/h)	1.69 (29)	1.92 (44)
apparent volume of distribution	V/F (L)	40.81 (29)	35.85 (47)

*Observed values reported from '*occasion 2*' of Langdon et al. [112]

Measures were derived from pharmacokinetic data (or simulation results) for a regimen consisting of a 900-mg dose administered repeatedly, four days apart. Shown are median properties (% CV)

As an additional verification, pharmacokinetic measures for RPT (e.g., maximum concentration, area under the curve, and half-life) were computed from the model and compared to those from the literature. In particular, Table 3.4 shows the predicted values from simulations of time-course plasma concentrations and those in Langdon et al. [112], which were based on experimental data that were not used in the model parameterization.

3.3.4 Testing and verification of the human-specific model (H-PBPK) for repeated dosing scenarios

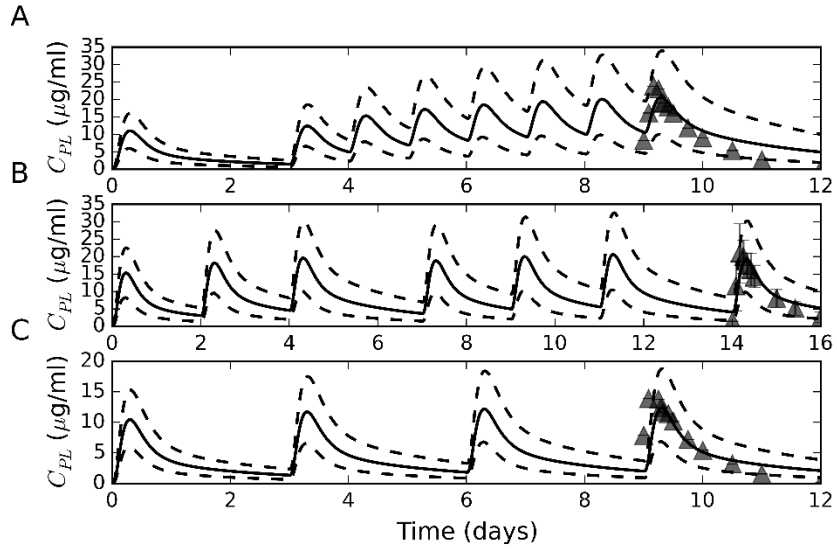

FIGURE 3.4. Model verification for repeated dosing: predictions of plasma RPT concentrations for the three dosing regimens described in the text. Solid and dashed lines represent the simulated mean and 95% prediction intervals, respectively, while the triangles denote experimental data from the test set.

Relevant to standard treatments regimens for MTB [129,130], model simulations were conducted for three repeated dosing scenarios for which well-controlled experimental data were available: regimen A - a 600 mg dose every day starting three days after an initial 600 mg dose [110]; regimen B - a 900 mg dose every two days [116]; and regimen C - a 600 mg dose every three days [110]. Both the experimental data and corresponding simulation results are displayed in Figure 3.4.

3.3.5 Prediction of lung concentrations using the human-specific model

Along with the predicted plasma concentrations shown in Figure 3.4, simulations yielded the levels of RPT and dRPT in the lung over time. As an illustration of potential antibiotic effect,

Figure 3.5 shows the predicted levels of RPT, dRPT, and total rifamycin over time in the lung for the three RPT oral dosing scenarios described above.

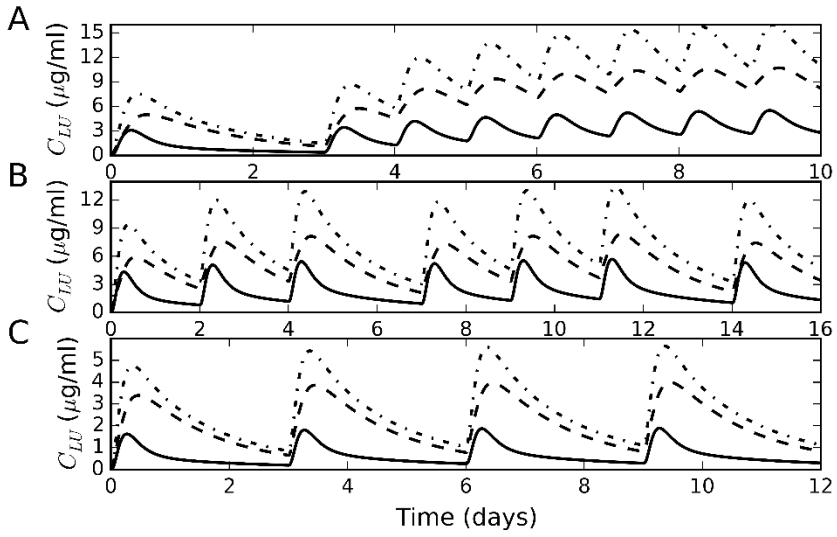

FIGURE 3.5. Model predictions of time-course concentrations in the lung following the three repeated oral regimens described in Figure 3.4, showing concentrations of RPT (solid line), dRPT (dashed line), and total rifamycin (dot-dashed line).

There are a number of current and anticipated guidelines for the treatment of both active TB disease and latent TB infection involving rifapentine as part of a combination therapy [82,107,131–133]. Across these regimens, doses of RPT range from 600 to 1200 mg with administration frequencies extending from daily to once weekly. To determine the pharmacokinetics and potential antibiotic effect of RPT and dRPT across these regimens, the model was used to predict lung concentrations of these species in a simulated population resulting from various doses of RPT at three administration frequencies: once weekly, twice weekly, and daily. The simulated population in these cases was the group of (virtual) individuals whose pharmacokinetics were predicted by Monte Carlo sampling across the estimated physiological and biochemical parameter distributions determined using the Bayesian procedure

described earlier. Figure 3.6 depicts a cumulative distribution function of the dose response that indicates the probability that RPT or dRPT concentrations in the lung are above their respective MICs, which were 0.063 mg/L for RPT and 0.25 mg/L for dRPT [8].

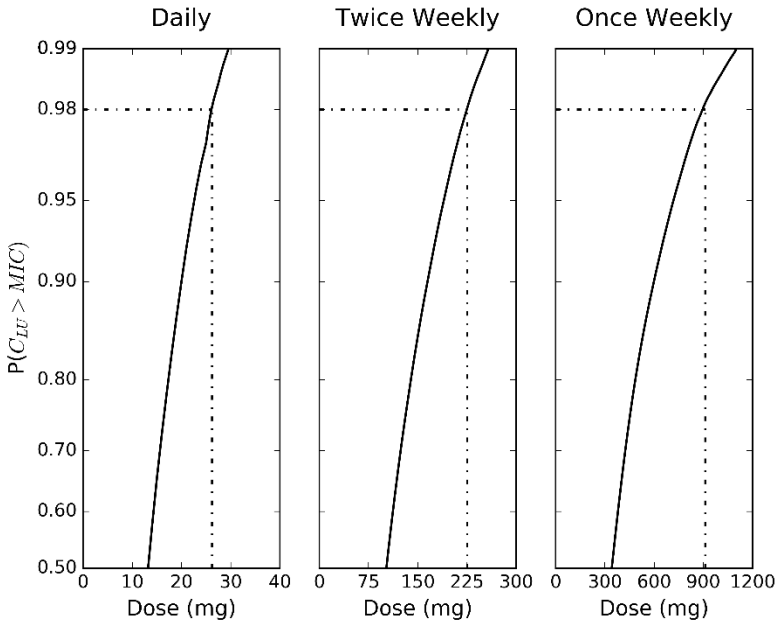

FIGURE 3.6. Probability that the minimum steady-state concentration of RPT in the lung exceeds the minimum inhibitory concentration.

3.4 DISCUSSION

3.4.1 Methodology

The PBPK models detailed herein utilized a system of biologically-based physiological and biochemical descriptions and species mass balance equations to make tissue-specific pharmacokinetic predictions for RPT and its metabolite, dRPT, in relevant tissue compartments for both rats and humans. The values of unknown parameters in the model system were estimated within a hierarchical Bayesian framework to incorporate data uncertainties and inter-study variability, and Monte Carlo simulations were conducted using these distributions to quantify their effect on pharmacokinetic predictions.

3.4.2 Testing and verification

Model predictions were generally in good agreement with data from the literature. As shown in Figure 3.2, the experimental data corresponding to plasma and tissue (lung, kidney, and spleen) concentrations were within the 95% prediction intervals for the rat-specific PBPK model, demonstrating its ability to reasonably predict tissue-level RPT pharmacokinetics in this species. For the human-specific PBPK model, single-dose data from multiple studies for both RPT and dRPT concentrations were in reasonable concordance with results from simulations (Figure 3.3). The relatively poorer agreement between predictions and data for dRPT is likely related to variability in metabolism between subjects, differences in analytical quantitation methods between studies, and/or an inadequate specification for RPT metabolism in the model. For repeated oral dosing, model predictions for RPT concentrations compare well with experimental data for all three dosing scenarios (Figure 3.4). Finally, as shown in Table 3.4, there was reasonable to very good agreement between pharmacokinetic measures, such as C_{max} and *AUC*, computed from simulations and experimental data.

3.4.3 Model predictions

A principal benefit to the PBPK approach is the ability to estimate internal doses that are generally not available in human subjects or patients. Figure 3.5 shows the predicted levels of RPT, dRPT, and total rifamycin over time in the lung for three repeated oral dosing scenarios for RPT. It should be noted that dRPT does not bind to plasma protein as readily as RPT. This decrease in fractional protein binding increases the bioavailabilty of dRPT and results in a higher predicted concentration of metabolite within the lungs. It is also notable that for all three dosing regimens, the predicted minimum concentrations for both RPT and dRPT in the lung are significantly above their *in vitro* MICs for MTB of 0.063 μg/ml and 0.25 μg/ml, respectively [8].

Finally, the total rifamycin concentration is presented in this figure as an indication that there may be additional bactericidal effect owing to the presence of dRPT; however, because the mechanism of action of dRPT is not currently known, the overall pharmacodynamic effect cannot be assumed to be additive.

Finally, the model was used to assess the potential efficacy of regimens spanning current recommended anti-TB therapies that include RPT [82,128,131–133]. This assessment was conducted by computing lung-tissue concentrations and comparing those to the MIC for MTB. These results are depicted in Figure 3.6, which shows the probability of the minimum steady-state drug concentration in the lungs exceeding the MIC for MTB for three distinct administration frequencies. For illustration, this figure also contains an example probability threshold of 0.98 from which a *minimum protective dose* (MPD) can be found. Using this probability threshold, the MPD was seen to be 26 mg for once daily dosing, 225 mg for the twice weekly regimen, and 910 mg for the once weekly administration (see Figure 3.6,). Based on these estimates, anti-TB regimens that include daily administration of 1200 mg RPT [82] for active TB disease exceed the predicted MPD, while those that reduce this dose and frequency for the treatment of latent TB infection to 750 mg once weekly [132], fall below the predicted MPD. It is important to note that these results do not include the antimicrobial effects of other anti-TB drugs given as part of the regimen; however, depending on the margin of safety, they could suggest possible adjustments to the dosing schedule.

3.4.4 Novel features and advantages of the present model

Unlike previous PBPK models for anti-TB drugs [38,117], the present model was developed to make predictions of pharmacokinetics in humans. To quantify and illustrate uncertainty in simulation outputs, model development and testing included a Bayesian approach

to parameter estimation and Monte Carlo simulations. These features allowed the verified model to be used to assess a current treatment regimen by comparing lung-specific predictions of antibiotic concentrations with the MIC for MTB. In addition, because administration of certain rifamycins (including rifapentine) has resulted in signs of drug induced liver injury [134], liver-specific predictions of drug levels could help inform treatments that minimize the potential for hepatotoxicity. Like most PBPK models, the one described herein allowed prediction of species concentrations in tissues/organs of interest and provided a systematic way to extrapolate across doses and between species. With these features, the model has the potential to aid in dose optimization and in the determination of how pharmacokinetic endpoints depend on alterations to anatomical, physiological, and biochemical parameters.

3.4.5 Limitations and deficiencies of the present model

The current H-PBPK currently suffers from several limitations and deficiencies: (i) it is not immediately applicable to the analysis of combination drug therapies, (ii) the pharmacokinetic predictions, while expected to be valid and useful for a population or subpopulation, may contain too much uncertainty for individualized applications like personalized medicine, (iii) parameters for the R-PBPK were estimated using relatively few data points and inaccuracies in some of these parameters were propagated to the human-specific model, and (iv) the specification used for RPT metabolism is biologically plausible, but owing to a lack of data, has not been adequately verified.

3.4.6 Future Directions

Using the present model as a foundation, efforts are underway to add additional anti-TB agents (e.g., isoniazid or bedaquiline) to simulate combination therapies and quantify pharmacokinetic drug-drug interactions. Other enhancements include integration of

pharmacodynamic descriptions that include MTB growth and drug-induced killing kinetics [59,135], and descriptions of RPT-induced hepatotoxicity [83,134].

3.5 Appendix: Derivation of Governing Equations

The following are the governing equations for the PBPK model, which mathematically specify the species mass balances and relevant biological phenomena in each compartment. In these equations, the superscript, *i*, corresponds to either parent RPT or the dRPT metabolite. While RPT disposition is described in all of the discrete tissue compartments, dRPT is modeled within only two compartments: lung and peripheral. Individual tissue blood flow rates, Q_T, were computed using total cardiac flow as $Q_T = Q_C \cdot Q_{TC}$ and $Q_C = Q_{CC} \cdot BW^{0.75}$. Q_{TC} values for the percentages of cardiac flow to each tissue are given in Table 1. Finally, the drug concentration entering tissues in the arterial blood is the free concentration of drug, $C^i_{A,f}$, and concentrations leaving the tissues are calculated using the concentrations within the tissue compartment along with the respective partition coefficients: $C^i_{T,ven} = C^i_T \,/\, P_T$.

Lung:

$$\frac{dA^i_{lung}}{dt} = Q_C \left(C^i_{venous} - C^i_{L,ven} \right) \tag{3.3}$$

Kidney:

$$\frac{dA^{RPT}_K}{dt} = Q_K \cdot \left(C^{RPT}_{A,f} - C^{RPT}_{K,ven} \right) - f_R \cdot CL^{RPT} \cdot C^{RPT}_{Art} \tag{3.4}$$

where *CL* and f_R are the total arterial blood stream clearance and fractional renal clearance, respectively.

Liver:

$$\frac{dA_L^{RPT}}{dt} = Q_{LA}C_{A,f}^{RPT} + Q_S C_S^{RPT} + Q_G C_G^{RPT} - Q_L C_{L,ven}^{RPT} - \left(1 - f_R\right) \cdot CL \cdot \left(Q_{LA}C_{Art}^{i} + Q_S C_S^{i} + Q_G C_G^{i}\right) / Q_L - v \tag{3.5}$$

where Q_L is the total blood flow leaving the liver and is the sum of the spleen, gut, and inlet liver blood flow rates. Biliary clearance for RPT occurs in the liver where the fraction of total blood clearance is equal to $1 - f_R$. Finally, *v* represents the rate of metabolism from RPT to dRPT presented in Eq. (3.2).

Gut:

$$\frac{dA_G^{RPT}}{dt} = Q_G \left(C_{A,f}^{RPT} - C_{G,ven}^{RPT}\right) + k_{GLG}A_{GL}^{RPT} + k_{SG}A_{RPT}^{stom} \tag{3.6}$$

Stomach:

$$\frac{dA_{Stom}^{RPT}}{dt} = F_a D \cdot d\left(t\right) - k_{SG}A_{Stom}^{RPT} \tag{3.7}$$

where F_a is the fractional absorption presented in Eq. (3.1), *D* is the ingested dose, and *d(t)* describes the time dependence of the dosing schedule.

Remaining Tissues:

$$\frac{dA_T^i}{dt} = Q_T \left(C_{A,f}^{i} - C_{T,ven}^{i}\right) \tag{3.8}$$

Arterial Blood:

$$\frac{dA_A^i}{dt} = Q_C \left(C_{L,ven}^{i} - C_{A,f}^{i}\right) - \alpha^i f_R \cdot CL^{dRPT} \cdot C_{A,f}^{dRPT} \tag{3.9}$$

Renal clearance for dRPT occurs based on the free concentration of dRPT in the arterial blood and is removed from the arterial blood compartment; therefore, $\alpha^{RPT} = 0$ and $\alpha^{dRPT} = 1$.

Venous Blood:

$$\frac{dA_V^i}{dt} = \sum_j^{N_T} Q_j C_{j,ven}^i + \beta^i v \tag{3.10}$$

All concentrations exiting the tissues are pooled in the venous blood compartment. Because there is no liver compartment for the dRPT sub-model, any generation of dRPT is within the venous blood; therefore, $\beta^{RPT} = 0$ and $\beta^{dRPT} = 1$.

Peripheral Compartment:

$$\frac{dA_P^{dRPT}}{dt} = Q_C \left(C_{A,f}^{dRPT} - C_{P,ven}^{dRPT} \right) - \left(1 - f_R \right) \cdot CL^{dRPT} \cdot C_{P,ven}^{dRPT} \tag{3.11}$$

Biliary clearance occurs within the peripheral compartment where the fraction of total clearance is equal to $1 - f_R$.

CHAPTER 4

CHARACTERIZATION OF THE DISPOSITION OF ACETAMINOPHEN THROUGH DEVELOPMENT AND APPLICATION OF A NOVEL PBPK MODEL

Acetaminophen (*N*-acetyl-para-aminophenol, paracetamol, APAP), is one of the most widely used analgesic and antipyretics in the world. It is metabolized primarily through glucuronidation by conjugation of uridine diphosphate glucuronic acid (UDPGA), and sulfation through conjugation with the 3'-phosphoadenosine-5'-phosphosulfate (PAPS) cofactor; however, APAP can also undergo cytochrome P450-mediated bioactivation to the glutathione depleting, putative hepatotoxicant *N*-acetyl-*p*-benzoquinone imine (NAPQI) [136–138].

Owing to its ubiquitous usage, potential for hepatotoxicity, and varying pharmacological effects across diverse and susceptible populations, numerous human pharmacokinetic studies have been conducted for this drug [136–156]. To quantify the results of such studies, non-compartmental [148,151,152,154,155] and compartmental [139,150,157,158] approaches have often been employed to determine the degree of exposure following administration of the drug (such as area under the curve, AUC) and the drug's associated pharmacokinetic (PK) parameters, such as clearance, elimination half-life, and the maximum concentration (C_{max}). Although useful and widely employed, these modeling approaches are limited in their ability to predict drug disposition in a tissue-specific manner, extrapolate across dosing scenarios, and account for an individual's unique anatomical, physiological, and biochemical features. One approach that is well suited for making such predictions, and is increasingly used in the field of pharmaceutical sciences [159], is physiologically-based pharmacokinetic (PBPK) modeling [45,160].

Using PBPK modeling coupled with hierarchical Bayesian inference methods, three components of APAP pharmacokinetics were investigated. First, a population PBPK model was developed to describe the absorption, distribution, metabolism, and elimination (ADME) of APAP under therapeutic dosing conditions [36]. Second, using a hierarchical Bayesian inference methodology, differences in APAP ADME were quantified in a sub-population specific manner to investigate the extent to which genetic variation and ethnicity may predispose individuals to a higher risk of APAP-induced hepatotoxicity [40]. Finally, the therapeutic PBPK model was extended to account for an APAP overdose scenario to predict the pharmacokinetics of APAP under clinically-realistic dosing conditions [39]. Using this model, a method for reconstructing administered dose was developed and optimal biomarker sampling times for dose reconstruction are presented. The following subchapters present the acetaminophen modeling work.

4.1 Physiologically Based Modeling of the Pharmacokinetics of Acetaminophen and its Major Metabolites in Humans Using a Bayesian Population Approach

There are presently several PBPK models for APAP and its metabolites, each of which was developed with different aims and a distinct approach. As part of a series of PBPK models for drug disposition in children, Edgington et al. [161] developed a PBPK model for APAP that utilized age-dependent anatomical and physiological parameter values. Results from this model showed reasonable agreement to values in the literature for several pharmacokinetic parameters, such as volume of distribution at steady state and drug half-life; however, there were significant differences between predicted and experimental values for plasma concentrations of APAP for many of the values compared. Although not physiologically based, Ben-Shachar et al. [162]

This work was performed jointly with the full list of co-authors available in [31].

created a multi-compartmental mathematical model to predict time-course plasma concentrations of APAP, accumulation of APAP and its metabolites in the urine, and glutathione (GSH) depletion. The model trends were in rough agreement with experimental data, but because it was not physiologically based, it is anticipated that accurate model predictions beyond the conditions used for calibration would be unlikely. With the aim of predicting APAP toxicity in humans, Péry et al. [163] coupled a PBPK and a toxicodynamic model to make predictions of APAP toxicity in humans. By utilizing *in vitro* data from rats and quantitative structure activity relationships to estimate model parameters, this approach could potentially reduce the need for extensive PK data from animals when developing PBPK models. Predictions from the model were in reasonable agreement with plasma PK data from rats; however, the model was not validated using human data, and since previous studies have shown that there is significant differences in phase II metabolism between rats and humans [164], such an extrapolation is likely to be problematic. To better understand APAP-induced hepatoxicity under several physiological conditions, Navid et al [165] created a PBPK model that included a quantitative description of GSH kinetics and semi-empirical relationships for chronic APAP uptake. Model predictions were in good agreement with plasma PK data from both a single dose and a multiple dosing study. Unfortunately, model predictions of GSH levels and kinetics were not compared to experimental values and the model equations contained no allometric scaling in the physiological parameters, limiting its utility beyond the range of data used for calibration. To better understand the kinetics of glutathione depletion and the role of ophthalmic acid and 5-oxoproline in GSH metabolism, Geenen et al. [166] developed a PBPK model for APAP that consisted of a small number of compartments (lung, kidney, liver, and "other tissue") and a detailed mathematical specification of GSH kinetics. Model predictions were in reasonable-to-good agreement with

various PK data from APAP dosing in both rats and humans. Assessing the accuracy and predictive capabilities of this model and others described previously is hampered by the lack of detail provided with respect to data and model uncertainty; it is also unclear if the same data used to illustrate the accuracy of model predictions were the same as those used for model calibration and parameter estimation.

The focus of the present work was to develop and demonstrate a new PBPK model that addresses some of the limitations of previous approaches and provides an accurate means of predicting the ADME of APAP and its conjugated metabolites in humans. To this end, the model integrated mechanistic descriptions of the absorption and metabolism of APAP, a Bayesian approach to model parameterization that accounts for data uncertainty and inter-study variability, and utilization of a comprehensive set of human pharmacokinetic data for model calibration and validation.

4.2 METHODS

4.2.1 Compiling and classifying data from the literature

A comprehensive review of the literature was conducted to identify adult human pharmacokinetic studies where APAP was administered in a single oral or intravenous dose. Emphasis was placed on identifying studies in which two major APAP metabolites, APAP-glucuronide (APAP-G) and APAP-sulfate (APAP-S), were quantified in addition to parent APAP. Studies were divided into a *training set* to be used for parameters estimation (model calibration) and a *test set* for verification and evaluation (model validation). A summary of the studies and their characteristics and classifications is given in Table A of the appendix.

4.2.2 Model description and formulation

In the following sections, we detail the model structure and the equations specifying the ADME within the model compartments.

4.2.2.1 Model structure and physiological parameters

As depicted in Figure 4.1.1, the PBPK model structure developed for APAP, APAP-G, and APAP-S consisted of compartments representing fat, muscle, liver, gastrointestinal (GI), and kidney, with remaining tissues lumped [45] into either rapidly perfused or slowly perfused compartments. All compartments were assumed to be perfusion limited [167].

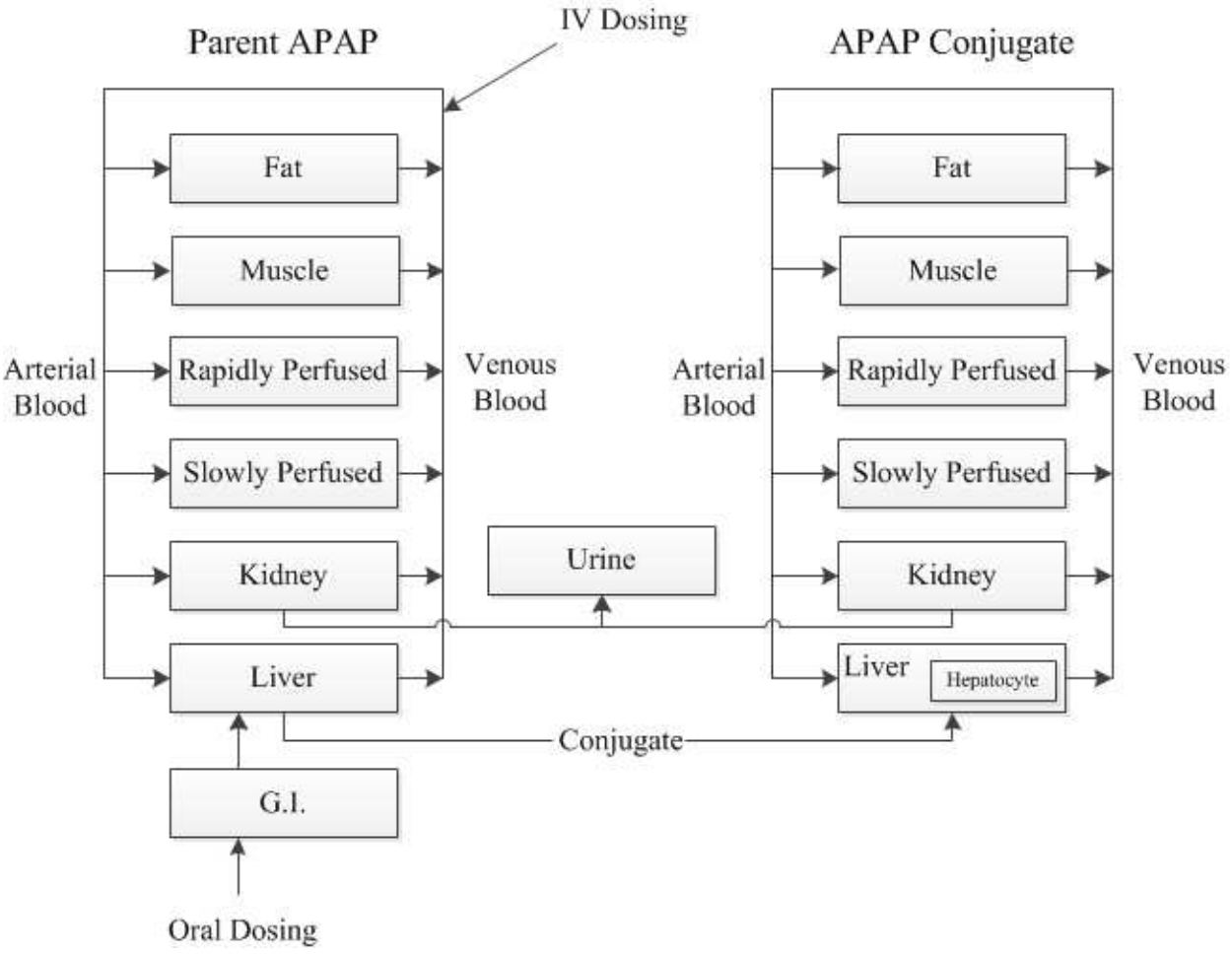

FIGURE 4.1.1. PBPK model structure

Compartmental volumes and blood flow rates (Table 4.1.1) were taken from Brown et al. [55], and volumes and flow rates for the rapidly- and slowly-perfused compartments were calculated as the mean values for the lumped tissues from Brown et al. [55].

TABLE 4.1.1. Physiological parameters. Cardiac output is expressed in units of L/(hr-BW0.75), while remaining tissue blood flow rates are expressed as fractions of cardiac output. Tissue volumes are expressed as L/BW0.75

Compartment		Value
Cardiac Output		
	Q_{CC}	16.2
Fat		
	Q_{FC}	0.052
	V_{FC}	0.21
Muscle		
	Q_{MC}	0.19
	V_{MC}	0.4
Liver		
	Q_{LC}	0.28
	V_{LC}	0.026
Kidney		
	Q_{KC}	0.18
	V_{KC}	0.0044
Slowly Perfused		
	Q_{SC}	0.14
	V_{SC}	0.19
Rapidly Perfused		
	Q_{RC}	0.22
	V_{RC}	0.077
Arterial Blood		
	V_{BLAC}	0.024
Venous Blood		
	V_{BLVC}	0.056

Rapidly perfused tissue comprised brain, lung, and spleen tissues, while slowly perfused consisted of bone, heart and skin [55].

4.2.2.2 Absorption

Several processes contribute to the absorption kinetics of APAP administered orally, including dissolution of the dose in the stomach, gastric emptying, and absorption down the length of the small intestine. To quantify these effects, the "averaged model" from Levitt [168] was used. This relationship, representing an approximate spatially-averaged solution of the diffusion-convection equation takes the following form:

$$\begin{aligned} \frac{dA_{GI}^{APAP}}{dt} &= I(t) - \frac{dA_{abs}}{dt} \\ \frac{dA_{abs}}{dt} &= \frac{M\left[\exp\left(\frac{-t}{T_G}\right) - \exp\left(\frac{-t}{T_P}\right)\right]}{T_G - T_P} \\ M &= F_A \cdot D_{oral} \end{aligned} \tag{4A.1}$$

Consistent with a previous convention [160], symbols indicating amounts and concentrations are given with a subscript indicating the tissue or compartment involved and a superscript indicating the chemical species. Here, A_{GI}^{APAP} is the amount of APAP in the GI compartment. Additionally, A_{abs} is the amount of APAP absorbed into the bloodstream, t is time, *I(t)* is the initial rate of dosing to the stomach, M is the total amount of drug available for absorption, D_{oral} is the initial APAP dose, and T_G and T_P represent time constants for gastric emptying and intestinal permeability, respectively. The fraction of APAP absorbed, F_A, has been shown to be dose dependent at doses less than 1000 mg [150]. To account for this effect in the model, the following equation was developed:

$$F_A = \begin{cases} 0.0005 \cdot D_{oral} + 0.37 & , \quad \text{if } D_{oral} \le 1000\,\text{mg} \\ 0.88 & , \quad \text{if } D_{oral} > 1000\,\text{mg} \end{cases} \tag{4A.2}$$

Predictions from Eq. (4A.1), are in good agreement with bioavailability data from the literature [139,150,154]. For example, for a 350 mg dose, the measured and predicted values of the

fraction absorbed are 0.57 [154] and 0.55, respectively, while for a 650 mg dose the values are 0.75 [139] and 0.7, respectively.

4.2.2.3 Tissue distribution

Assuming passive diffusion into and out of the tissue, the rate of change of concentration within a compartment is given by the species mass balance equation

$$\frac{dA_T^j}{dt} = V_T \frac{dC_T^j}{dt} = Q_T \left(C_A^j - C_{V-T}^j \right)$$
$$C_{V-T}^j = \frac{C_T^j}{P_{T:blood}} \qquad \text{(4A.3)}$$

where A_T^j is the amount of species j within the tissue compartment T, V_T is the volume of compartment T, C_A^j is the concentration of the chemical in the arterial blood flowing into the tissue, C_{V-T}^j is the concentration of drug flowing out of the compartment into the venous blood, and $P_{T:blood}$ is the tissue:blood partition coefficient.

TABLE 4.1.2. Drug specific physiochemical properties and resulting tissue:blood partition coefficients

Physicochemical properties [169,170]

	APAP	APAP-G	APAP-S
pKa_1	9.96	3.17	-2.2
pKa_2	-4.4	-3.7	-4.4
logP	0.91	-0.68	-1
Fraction unbound	0.82	0.92	0.46
Calculated partition coefficients			
P_{fat}	0.447	0.128	0.088
P_{muscle}	0.687	0.336	0.199
P_{kidney}	0.711	0.392	0.261
P_{liver}	0.687	0.321	0.203
P_{rapid}	0.676	0.364	0.207
P_{slow}	0.606	0.351	0.254

Values for the tissue:blood partition coefficients were determined using the method from Rodgers et al. [49], which requires specification of several physicochemical properties of the molecule of interest. Table 4.1.2 lists the values of these parameters for APAP, APAP-G, and APAP-S, along with the calculated partition coefficients for each model compartment. Finally, because there is negligible protein binding of APAP in the blood [171,172], a blood-to-plasma concentration ratio of one was used for each species.

4.2.2.4 Metabolism and clearance

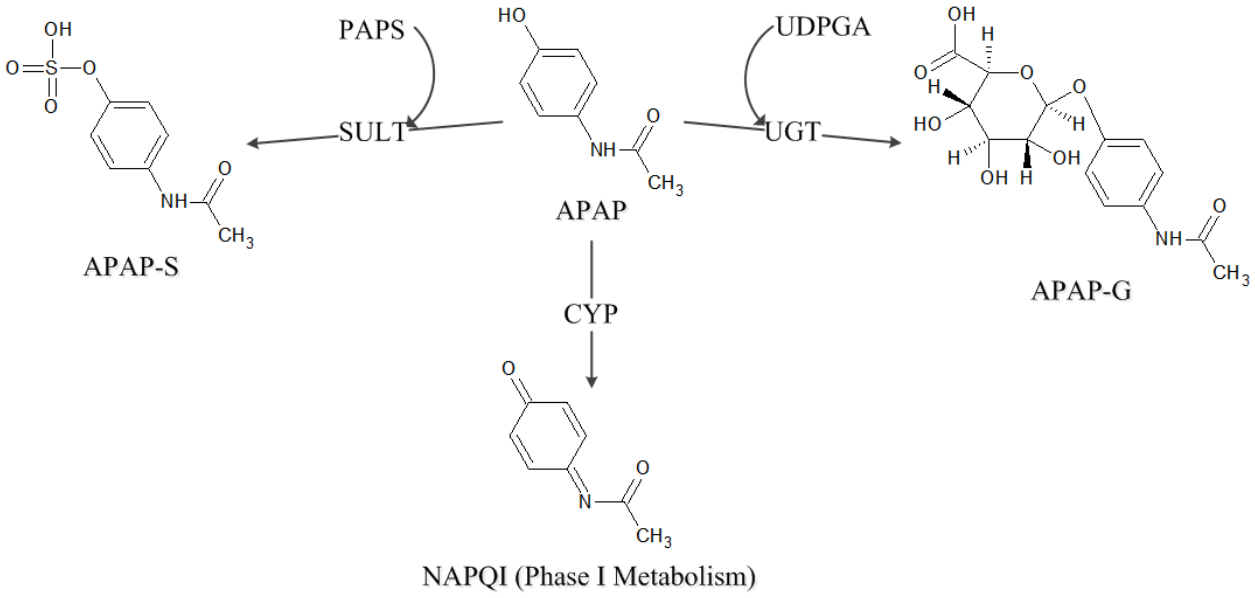

FIGURE 4.1.2. Principal pathways for APAP metabolism in humans

As depicted in Figure 4.1.2, major routes of metabolism of APAP in the liver include glucoronidation to form APAP-G, sulfation to APAP-S, and cytochrome P450-mediated bioactivation to the glutathione-depleting species *N*-acetyl-*p*-benzoquinone imine (NAPQI) [4–6]. As shown, the phase II pathways require a cofactor for conjugation: uridine diphosphate glucuronic acid (UDPGA) for glucuronidation and 3'-phosphoadenosine-5'-phosphosulfate (PAPS) for sulfation. In humans, the percentage of APAP metabolized is roughly 54-58% to

APAP-G through UDP-glucuronosyltransferase (UGT) [138,148,173], 29-32% to APAP-S through sulfotransferases (SULT) [138,148,173], and 4-8% to NAPQI through cytochrome P450 isozymes [173,174].

These processes of APAP metabolism were specified mathematically as follows. For phase I metabolism, standard Michaelis-Menten saturation kinetics were used to describe the APAP oxidation,

$$v_{cyp} = \frac{V_{M-cyp} C_{liver}^{APAP}}{K_{M-cyp}^{APAP} + C_{liver}^{APAP}} \tag{4A.4}$$

where v_{cyp} is the rate of APAP conversion, and V_{M-cyp} and K_{M-cyp}^{APAP} represent the Michaelis-Menten constants for APAP biotransformation through cytochrome p450 isozymes. Because the phase II conjugation pathways involve both co-substrate and substrate inhibition [173,175,176], bi-bi enzyme kinetics [177] with APAP substrate inhibition was used to specify the rates of conjugation formation:

$$v_{conjugate} = \frac{V_{M-enz} C_{liver}^{APAP} \phi_{liver}^{cf}}{\left(K_{M-enz}^{APAP} + C_{liver}^{APAP} + \frac{\left(C_{liver}^{APAP} \right)^2}{K_{I-enz}} \right) \left(K_{M-enz}^{cf} + \phi_{liver}^{cf} \right)} \tag{4A.5}$$

Here, $v_{conjugate}$ is the rate of APAP conversion to conjugate; V_{M-enz} is the enzyme-specific maximum rate of conversion; K_{M-enz}^{APAP} and K_{I-enz}^{APAP} represents the Michaelis-Menten constants and inhibition constants for APAP, respectively; and ϕ_{liver}^{cf} is the fraction of cofactor available for reaction within the liver. As the abundance of enzyme depends on liver mass, values of the maximum rates of conversion in Eqns. (4A.4) and (4A.5) were computed through allometric

scaling of corresponding values from the literature, V_{MC-enz}, by the equation $V_{M-enz} = V_{MC-enz} \cdot BW^{0.75}$, where BW is body weight.

The rates of formation and depletion of the cofactors UDPGA and PAPS influence the levels of APAP conjugates [178,179] and mediate the flux of APAP through the phase I metabolic pathway to NAPQI [180]. To quantify this effect, it was assumed that the rate of cofactor depletion is equal to the rate of APAP consumption for the associated enzyme and that cofactor is regenerated once APAP concentrations in the liver are reduced. The resulting relationship for cofactor kinetics then takes the form

$$\frac{dA_{liver}^{cf}}{dt} = -v_{conjugate} + k_{syn-cf}\left(1-\phi_{liver}^{cf}\right) \tag{4A.6}$$

where A_{liver}^{cf} is the amount of cofactor in the liver, $v_{conjugate}$ is the rate of conjugate formation, and $k_{syn\text{-}cf}$ represents the rate of synthesis of the cofactor.

In addition to cofactor kinetics, active transport of the conjugates from hepatocytes into the extracellular environment has a significant influence on APAP metabolism and clearance. Iida and coworkers [181] demonstrated that APAP freely diffuses into hepatocytes, but once it is metabolized to either APAP-G or APAP-S, membrane transporters facilitate movement of these conjugated molecules into the greater liver parenchyma. Following their mathematical description, the rate of transport of a given conjugate, $v_{mem-conj}$, was assumed to follow saturation kinetics,

$$v_{mem}^{conj} = \frac{V_{M-mem}^{conj} C_{hep}^{conj}}{K_{M-mem}^{conj} + C_{hep}^{APAP}}, \tag{4A.7}$$

where V_{M-mem}^{conj} and K_{M-mem}^{conj} are the kinetic parameters for membrane transport, and C_{hep}^{conj} is the concentration of conjugate within the hepatocyte.

The final factor considered with regard to clearance of APAP and its metabolites was renal excretion to the urine, which was modeled though an allometrically-scaled clearance constant,

$$\frac{dA_{KE}^{j}}{dt} = k_R^j \cdot C_A^j \qquad (4A.8)$$
$$k_R^j = k_{R0}^j \cdot BW$$

Here, k_R^j is the rate of renal elimination of the chemical; *j* represents APAP, APAP-G, or APAP-S; and k_{R0}^j are baseline values that are scaled allometrically by body weight. Biliary clearance was neglected because APAP and APAP-S are not excreted into the bile, and APAP-G is only excreted in trace amounts [182].

4.2.2.5 PBPK model equations

Combining the above species mass balance equations and mechanistic relationships results in the governing equations comprising the mathematical expression of the PBPK model. This system of differential and algebraic equations is summarized in Table B of the appendix.

4.2.3 Parameter estimation and model simulations

Unknown model parameters in the governing equations were estimated within the context of a Bayesian hierarchical framework [123,183]. The hierarchy consisted of two levels: a population level, comprising an aggregation of all of the training set data across all of the studies, and a study level, consisting of all of the separate training set studies. Using this methodology, inter-study variability could be accounted for and pharmacokinetic predictions and parameter distributions could be found and compared at both levels within the hierarchy.

Within the framework, the parameter space was sampled using a Markov chain Monte Carlo (MCMC) method [73] using three independent Markov chains per simulation. Distributions for parameter priors were based on values from the literature when available, and were assumed to be uniform distributions over biologically-plausible ranges otherwise. Markov chains were run for 100,000 iterations per chain, and convergence was assessed using a Gelman-Rubin reduction factor [73] with a maximum threshold of $R = 1.05$. Posterior parameter distributions were computed from the final 30,000 iterations of each chain. For each of these final iterations, the complete set of parameter values was recorded as an individual "setpoint" [77].

Following parameterization, the governing equation system was solved at dosing scenarios of interest using all of the 30,000 setpoints, leading to a family of simulation results that was used subsequently to illustrate predictions for a variety of pharmacokinetics measures of interest and quantify the uncertainty associated with these values.

4.2.4 Software and computing platform

Data available from the literature in graphical form were digitized using DigitizeIt v.1.5.8 [124]. Simulations of the governing equation system, including the MCMC and setpoint analyses, were conducted using MCSim v5.4 [77]. Processing, analysis, and visualization of data and simulation results was carried out using scripts written in Python v.2.7.2 [125], utilizing the numpy [126], scipy [66], and matplotlib [127] packages. All calculations were performed on a computer cluster running the 64 bit CentOS Linux operating system on six gigabit linked Dell 2950 servers, each containing two quad-core 2.5 GHz Xeon processors and 64 GB of RAM.

4.3 RESULTS AND DISCUSSION

4.3.1 Model parameter values

TABLE 4.1.3. Parameter descriptions and prior distributions.

Description	Parameter (units)	Distribution	Reference
Acetaminophen Absorption			
gastric emptying time constant	T_G (hr)	N (0.23, 0.5)	[168]
GI perfusion time constant	T_P (hr)	N (0.033, 0.5)	[168]
Phase I metabolism			
cytochrome P450 K_M	K_{M-cyp}^{APAP} (μM)	N (130, 1)	[184]
cytochrome P450 V_{max}	V_{MC-cyp} (μmol/hr-BW$^{0.75}$)	U (0.14, 2900)	-
Phase II metabolism: sulfation			
sulfation pathway acetaminophen K_M	K_{M-sult}^{APAP} (μM)	N (300, 1)	[185]
sulfation pathway substrate inhibition K_i	K_{I-sult}^{APAP} (μM)	N (526, 1)	[176]
sulfation pathway PAPS K_M	K_{M-sult}^{PAPS} (unitless)	N (0.5, 0.5)	-
sulfation pathway acetaminophen V_{max}	$V_{MC-sult}$ (μmol/hr-BW$^{0.75}$)	U (1, 3.26E6)	-
Phase I metabolism: glucuronidation			
glucuronidation pathway acetaminophen K_M	K_{M-ugt}^{APAP} (μM)	N (6.0E4, 1)	[185]
glucuronidation pathway substrate inhibition K_i	K_{I-ugt}^{APAP} (μM)	N (5.8E4, 0.25)	[175]
glucuronidation pathway GA K_M	K_{M-sult}^{UDPGA} (unitless)	N (0.5, 0.5)	-
glucuronidation pathway acetaminophen V_{max}	V_{MC-ugt} (μmol/hr-BW$^{0.75}$)	U (1, 3.26E6)	-
Active hepatic transporters			
APAP-G hepatic transporter K_M	K_{M-mem}^{APAP-G} (μM)	N (1.99E4, 0.3)	[181]
APAP-G hepatic transporter V_M	V_{M-mem}^{APAP-G} (μmol/hr)	U (1.09E3, 3.26E6)	-
APAP-S hepatic transporter K_M	K_{M-mem}^{APAP-S} (μM)	N (2.29E4, 0.22)	[181]
APAP-S hepatic transporter V_M	V_{M-mem}^{APAP-S} (μmol/hr)	U (1.09E3, 3.26E6)	-
Cofactor synthesis			
UDPGA synthesis	$k_{syn-UDPGA}$ (1/hr)	U (1, 4.43E5)	-
PAPS synthesis	$k_{syn-PAPS}$ (1/hr)	U (1, 4.43E5)	-
Clearance			
acetaminophen clearance	k_{R0}^{APAP} (L/hr-BW$^{0.75}$)	U (2.48E-3, 2.718)	-
acetaminophen-glucuronide clearance	k_{R0}^{APAP-G} (L/hr-BW$^{0.75}$)	U (2.48E-3, 2.718)	-
acetaminophen-sulfate clearance	k_{R0}^{APAP-S} (L/hr-BW$^{0.75}$)	U (2.48E-3, 2.718)	-

N(a, b) denotes a normal distribution with mean, a, and coefficient of variation, b; U(a, b) denotes a uniform distribution with minimum and maximum values a and b, respectively.

Using time-course plasma and urinary data from the designated training set of studies (Table A), and the priors listed in Table 4.1.3, distributions for the unknown parameters in the governing equations were computed through the Bayesian framework described earlier.

TABLE 4.1.4. Posterior distributions for parameters

Parameter (units)	Value
Acetaminophen absorption	
T_G (hr)	0.332 (0.36)
T_P (hr)	0.0476 (0.30)
Phase I metabolism	
K_{M-cyp}^{APAP} (μM)	123 (0.29)
V_{MC-cyp} (μmol/hr-BW$^{0.75}$)	2.57 (0.87)
Phase II metabolism: sulfation	
K_{M-sult}^{APAP} (μM)	1.2E3 (0.39)
K_{I-sult}^{APAP} (μM)	478 (0.25)
K_{M-sult}^{PAPS} (unitless)	0.345 (0.40)
$V_{MC-sult}$ (μmol/hr-BW$^{0.75}$)	467 (0.38)
Phase II metabolism: glucuronidation	
K_{M-ugt}^{APAP} (μM)	6.14E3 (0.33)
K_{I-ugt}^{APAP} (μM)	4.99E4 (0.26)
K_{M-sult}^{UDPGA} (unitless)	0.343 (0.38)
V_{MC-ugt} (μmol/hr-BW$^{0.75}$)	5.21E3 (0.31)
Active hepatic transporters	
K_{M-mem}^{APAP-G} (μM)	1.75E4 (0.27)
V_{M-mem}^{APAP-G} (μmol/hr)	3.54E4 (0.45)
K_{M-mem}^{APAP-S} (μM)	2.23E4 (0.20)
V_{M-mem}^{APAP-S} (μmol/hr)	1.4E7 (1.65)
Cofactor synthesis	
$k_{syn-UDPGA}$ (1/hr)	3.6E4 (0.87)
$k_{syn-PAPS}$ (1/hr)	3.66E3 (0.69)
Clearance	
k_{R0}^{APAP} (L/hr-BW$^{0.75}$)	0.0123 (0.35)
k_{R0}^{APAP-G} (L/hr-BW$^{0.75}$)	0.155 (0.22)
k_{R0}^{APAP-S} (L/hr-BW$^{0.75}$)	0.138 (0.28)

Values are reported as the mean (coefficient of variation) of the distribution

The resulting posterior distributions for each parameter are summarized in Table 4.1.4. As described, setpoint analyses were then conducted to accumulate a large family of simulation results indicative of the data uncertainty and inter-study variability realized in these parameter distributions. These results were subsequently used in the various comparisons and predictions shown below.

4.3.2 Model validation and testing

To validate the PBPK model, several comparisons and assessments were made. For convenience in evaluating these comparisons, both the appropriate training set data (used in the model calibration) and test set data (reserved for validation) from Table A of the appendix are shown in subsequent plots. The former points are presented so that the accuracy of the parameter estimation can be assessed, while the latter can be used to evaluate the predictive nature of the model.

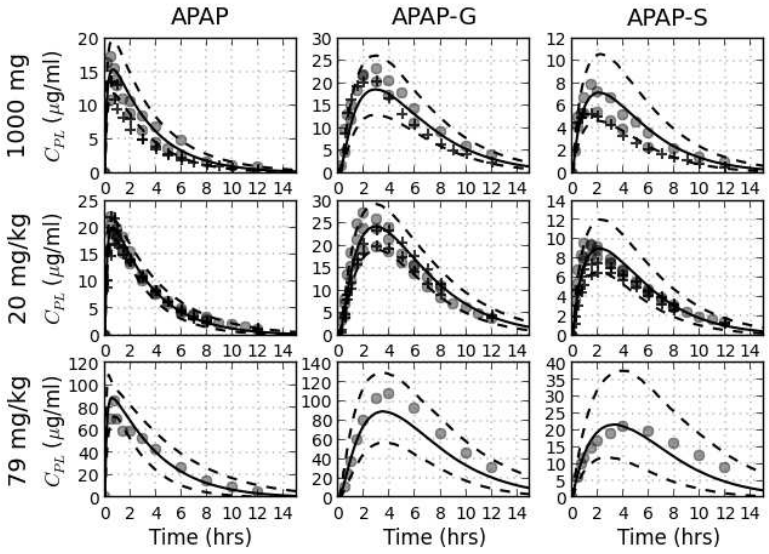

FIGURE 4.1.3. Comparison of model simulations results to human plasma concentration data following oral dosing of APAP. Simulation results are shown with a solid line for mean values and dashed lines representing 95% confidence intervals. Data from the training set are represented by circles (o), while those from the test are represented by the plus sign (+).

First, model predictions for time-course plasma concentrations of APAP, APAP-G, and APAP-S were compared to experimental values obtained from the literature. As shown in Figure 4.1.3, there is generally good agreement between predicted and measured values of the time-course concentrations for both the parent chemical and its metabolites over a wide range of data obtained from numerous studies. These simulations also illustrate the degree of uncertainty in the model predictions based on parameterization to data from a diverse set of studies.

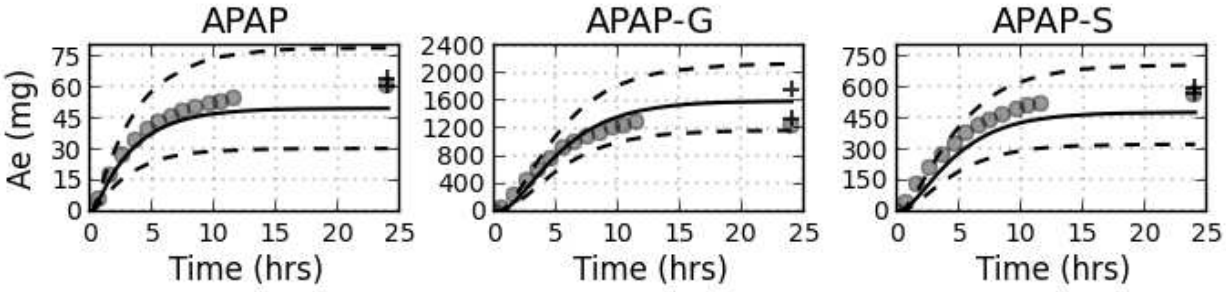

FIGURE 4.1.4. Comparison of model simulation results to experimental data for the accumulated amount of APAP in the urine following a 20 mg/kg oral dose

The ability of the model to accurately simulate renal clearance was then evaluated. There are relatively few studies in humans detailing the amount of APAP and its metabolites in the urine over time. Here, available time-course data [138,147,148,152] were used as the training set for model calibration, while data at the terminal time point of 24 hours [137,142,145] were applied as the test set. As shown in Figure 4.1.4, model and experimental results at 24 hours are in satisfactory to good agreement for the accumulated amounts of all three chemical species. Future studies quantifying the time course amounts of APAP and its metabolites in the urine would further reduce the uncertainty in these predictions.

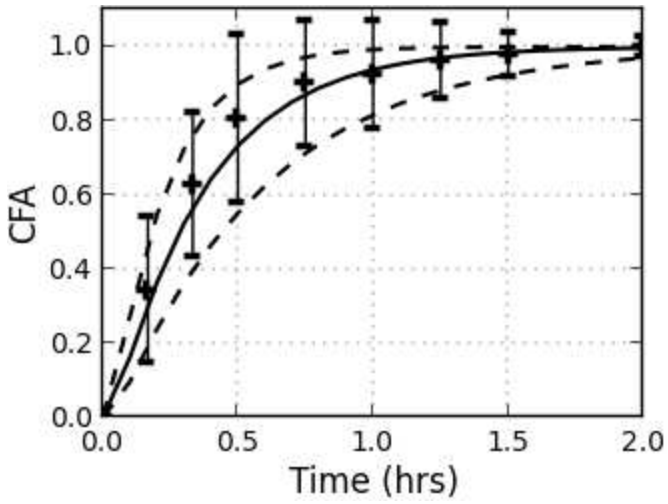

FIGURE 4.1.5. Cumulative fraction absorbed (CFA) of APAP into the blood stream. Simulation results are shown with a solid line for mean values and dashed lines representing 95% confidence intervals. Plus signs (+) represent data from the literature and were not part of the training set.

Next, model predictions of APAP absorption into the blood stream were assessed. Figure 4.1.5 shows simulated values of cumulative fraction absorbed (CFA), along with corresponding *in vivo* data from Souliman et al. [186] for a 500 mg oral dose of APAP administered to humans in a fasted state. The good agreement between model predictions and experimental data lends support to the quantitative description of absorption used in the PBPK model. However, although not explicitly tested in this study, if simulations for dosages outside of the clinical range (e.g., overdose) are to be conducted, it is anticipated that the time constants in the model for gastric emptying and gut perfusion may need to be adjusted or made dose dependent.

Finally, comparisons were made with respect to several common pharmacokinetic parameters: AUC, C_{max}, mean residence time (MRT), and fraction excreted. Table 4.1.5 lists mean values and uncertainties of these measures for a single oral dose of 20 mg/kg of APAP. Because the data values [137] were part of the test set enumerated in Table A and were not used in model calibration, the good agreement between simulation-based and experimentally-derived

TABLE 4.1.5. Comparison of pharmacokinetic parameters from experiments and model simulations

		Experiments	Model simulations
APAP	C_{max} (μg/ml)	21.51 (14.4 - 32.3)	20.50 (16.45 - 28.93)
	AUC (μg/m/hr)	83.16 (50.8 - 117.1)	83.09 (49.56 - 128.62)
	MRT (hr)	3.21 (3.01 - 3.51)	3.45 (2.41 - 4.69)
	CL_R (mL/min)	11.52 (4.5 - 18.1)	13.27 (6.75 - 26.09)
	% Recovery	5.03 (2.4 - 9.0)	5.06 (1.51 - 10.27)
APAP-G	C_{max} (μg/ml)	10.27 (5.8 - 15.1)	11.43 (6.82 - 17.04)
	AUC (μg/m/hr)	82.68 (50.9 - 119.5)	87.65 (55.33 - 135.66)
	MRT (hr)	6.18 (5.18 - 6.77)	5.76 (4.40 - 7.58)
	CL_R (mL/min)	133.95 (82 - 187)	169.51 (107.46 - 267.41)
	% Recovery	57.21 (40.7 - 68.6)	68.77 (51.66 - 85.94)
APAP-S	C_{max} (μg/ml)	5.18 (3.15 - 7.41)	5.64 (2.79 - 10.32)
	AUC (μg/m/hr)	38.74 (24.2 - 62)	38.28 (16.61 - 79.78)
	MRT (hr)	5.91 (5.35 - 6.49)	4.91 (3.55 - 6.42)
	CL_R (mL/min)	153.4 (85 - 217)	158.35 (94.18 - 266.24)
	% Recovery	31.28 (19.8 - 46.4)	27.73 (11.51 - 45.61)

Tabulated values presented in the "Experiments" columns were taken directly from Critchley et al. [137], except for MRT, which was computed from digitized data extracted from the same reference.

values for all measures and chemical species provides evidence of the accuracy of the PBPK model in predicting these summary parameters within the uncertainties of the system.

4.3.3 Model predictions

To demonstrate its utility for elucidating and quantifying the ADME of APAP, several predicted outputs and endpoints of interest are illustrated in the following sections: cofactor depletion, dose-dependence of pharmacokinetic parameters, and the relationship between APAP levels in the plasma to those in the liver.

4.3.3.1 Cofactor depletion

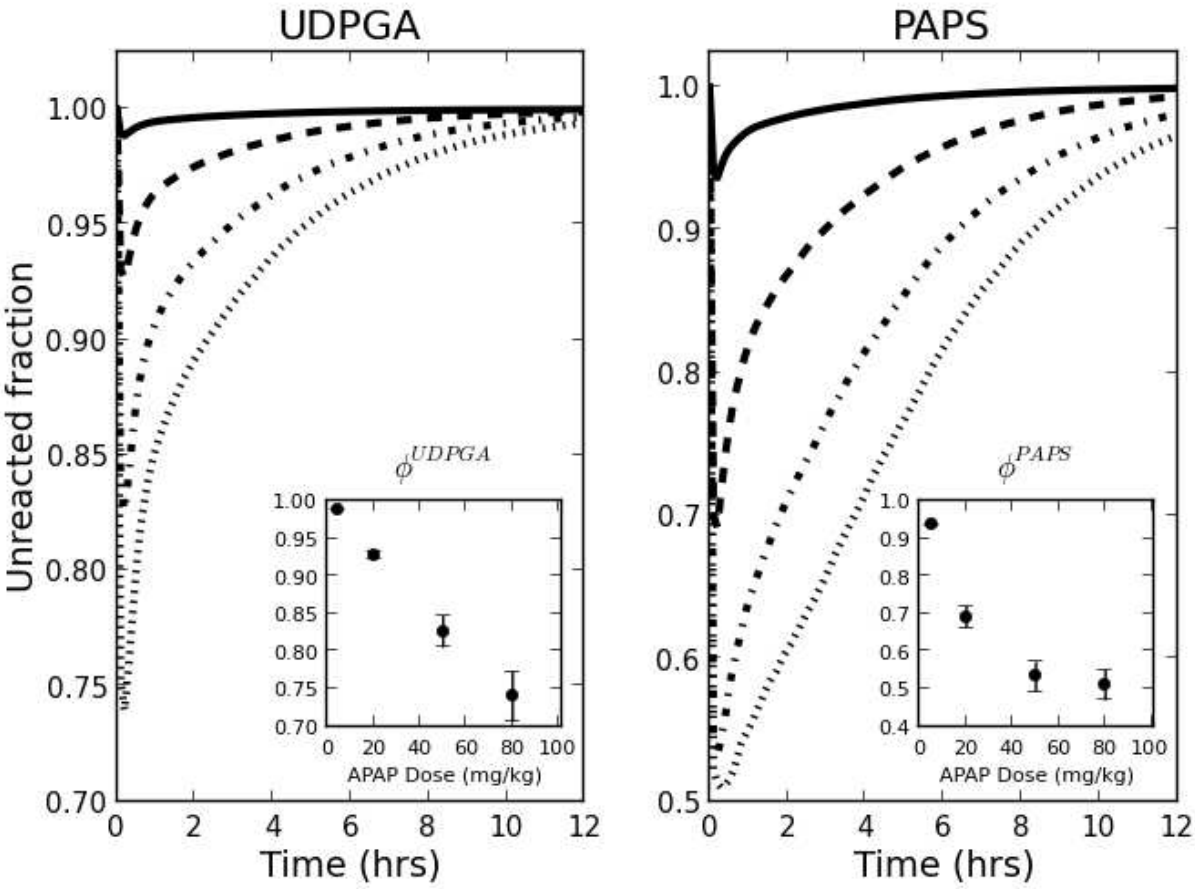

FIGURE 4.1.6. Model prediction of depletion of the cofactors UDPGA and PAPS. Insets depict the predicted dose-response for the minimum available cofactor following APAP administration.

Because acetaminophen is rapidly metabolized to APAP-G and APAP-S, associated cofactors may be quickly depleted, thus reducing the rate of acetaminophen conjugation. For example, the PAPS cofactor has been reported to deplete under therapeutic dosing conditions, reducing the rate of acetaminophen clearance [6]. In addition, since sulfation and glucuronidation are common during phase II metabolism of many xenobiotics [154], cofactor depletion may be an important consideration for the co-administration of other drugs with APAP. Figure 4.1.6

depicts model simulations for cofactor depletion following APAP administration. The predicted time-frame for PAPS and UDPGA depletion in the liver agree with that from Hjelle et al. [187], where the majority of cofactor is depleted 30 to 60 minutes post-acetaminophen dosing. The insets in Figure 4.1.6 show the predicted values of the minimum fraction of cofactor available, ϕ^{PAPS} and ϕ^{UDPGA}, at various clinically-relevant doses. Data quantifying the dose-dependency of cofactor depletion in humans could not be found in the literature; however, the trends seen in these insets are similar to those for reduction in PAPS and UDPGA observed in an experimental study in rats [187].

4.3.3.2 Dose-dependent pharmacokinetic parameters

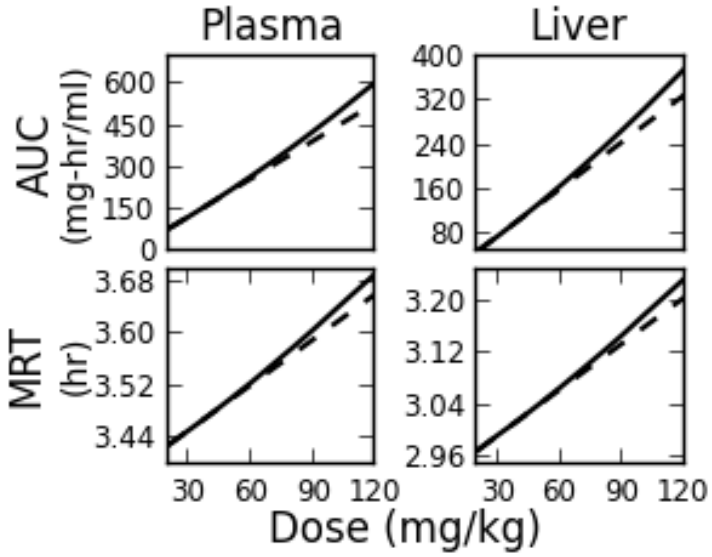

FIGURE 4.1.7. Model prediction of the dose-dependence of pharmacokinetic measures for APAP in the plasma and the liver compartment: AUC and mean residence time (MRT). Dashed lines represent a linear response with respect to dose.

Understanding the variation in a drug's pharmacokinetic parameters with respect to dose can help to inform its safe and effective administration. Figure 4.1.7 shows model predictions of

the dose dependence of two important pharmacokinetic metrics for APAP: AUC and mean residence time (MRT) in both the plasma and liver. Consistent with results from the literature [188], predictions from the PBPK model indicate a linear dose-dependence for these metrics over a range of common therapeutic oral doses, but show deviations from this linear trend at doses above about 60 mg/kg. These latter simulation results are indicative of saturation of the sulfation and glucoronidation pathways through depletion of the metabolic cofactors (see §4.3.3.1) and are in accord with results from previous experimental studies [189–191].

4.3.3.3 Relating APAP levels in the plasma to those in the liver

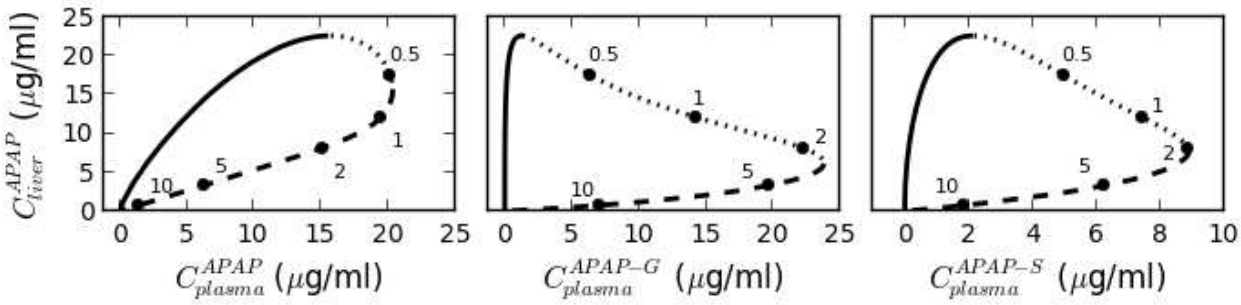

FIGURE 4.1.8. Model prediction of the relationship between plasma levels of parent compound and conjugates and parent APAP in the liver for a 20 mg/kg dose. Time increases in the clockwise direction around the trajectory loops and numbers shown correspond to the number of hours post dosing. Line styles are described in the text.

Although the putative species responsible for hepatotoxicity is NAPQI and not APAP, assessment of potential acetaminophen toxicity is currently based on knowledge of the administered dose or the APAP level measured in the plasma [174]. Even when using the level of APAP as a measure of potential hepatotoxicity, the concentration in the liver is expected to be a more representative dose metric than that present elsewhere in the body. To estimate this concentration, however, requires a method to associate it with a more readily measurable quantity, such as the amount of APAP or its metabolite in the plasma. This predictive

relationship could be deduced by comparing and connecting concentration-time profiles for these species. Figure 4.1.8 depicts an alternative approach, in which each trace or trajectory provides a direct means of estimating C_{liver}^{APAP} given a value of C_{plasma} for one (or more) of APAP, APAP-G, or APAP-S, and some knowledge of the time after dosing. Additionally, from a qualitative perspective, these plots characterize the relationship between the pharmacokinetics of the two chemicals. For instance, each trajectory in this figure is visually segmented to give a rough indication of regions of shared pharmacokinetic processes:

	plasma		*liver*
	APAP	APAP-G , APAP-S	APAP
solid line:	absorption	formation	absorption
dotted line:	absorption	formation	elimination
dashed line:	elimination	elimination	elimination

Furthermore, the trajectory's deviation from the diagonal and degree of diagonal indicate the gross differences in the magnitude and time scale for the ADME of the plasma and liver species, and the length of the dotted portion of a curve expresses the difference in the time at which C_{max} occurs (t_{max}).

4.4 CONCLUSIONS

The primary objective of this study was to create a physiologically-based pharmacokinetic model for acetaminophen ADME in humans, supported by a broad set of experimental data from the literature. Once developed and validated, this model enabled the simulation of the disposition of APAP and two of its key metabolites, APAP-G and APAP-S, in plasma, urine, and several pharmacologically- and toxicologically-relevant tissues, and included information to compute the uncertainty in these predictions. Although not commonly measured clinically, the metabolites examined here have markedly different pharmacokinetic profiles than that of the parent drug, and their levels provide additional and complementary information useful

in estimating APAP dose and internal tissue concentrations. Because the model is based on physiological and biochemical relationships, we anticipate that it will be useful in a number of applications, such as dose extrapolation studies, determining the tissue-specific pharmacokinetics of APAP in susceptible, vulnerable, or health-compromised populations, assessing the pharmacokinetic impact of co-administration of another drug, relating measured biomarker levels to internal concentrations, and estimating administered dose using concentrations measured in plasma and urine. Finally, if integrated with appropriate pharmacodynamic equations and relationships, the present model could be used to help predict and characterize APAP toxicity.

4.5 Characterizing the Effects of Race/Ethnicity of Acetaminophen Pharmacokinetics using Physiologically Based Pharmacokinetic Modeling

While APAP is a well-known hepatotoxicant in both the United States and United Kingdom, relatively little is known about the influence of genes and race/ethnicity on the disposition of APAP and the extent to which genetic variation and ethnicity may predispose individuals to a higher risk of APAP-induced hepatotoxicity. Although numerous pharmacokinetic studies [136–139,141–144,146–155] and compartmental and non-compartmental analyses [139,148,150,162] have been conducted to estimate important pharmacokinetic parameters for this drug, only a few studies [137,138,192,193] have clarified the pharmacokinetics of APAP with a focus on the influence of intersubject and genetic variations. And, to our knowledge, models that are capable of making tissue specific predictions [36,163,166,194,195], important in evaluating the risk of hepatotoxicity, are generally based on

This work was performed jointly with the full list of co-authors available in [35].

pooled data sets and cannot be expected to provide accurate predictions for APAP ADME for individual subgroups or subpopulations.

To begin to fill this gap, the objective of this research was to extend an extensively-validated PBPK model for APAP [36] and utilize a hierarchical parameterization approach to develop and validate *subpopulation-specific* PBPK models for two genetically-different groups. The model was then used to quantify the difference in ADME between these groups and demonstrate and predict tissue-specific measures not available from experimental studies.

4.6 METHODS

4.6.1 Compiling and classifying experimental data from the literature

A comprehensive set of human pharmacokinetic data mined from the literature [36] was divided into two groups based on ethnicity as an indicator of the expected abundance of phenol-metabolizing alleles. Group ‘A’ comprised studies whose subjects were from ethnic groups that exhibit a higher proportion of the sulfotransferase (SULT1A1*2) [176,196] allele and the UDP-glucuonosyltransferase (UGT1A6*2/UGT1A9*1) [197–199], such as those found in Western Europeans. Group ‘B’ comprised studies where the SULT and UGT enzymes reflected those in Eastern Asian populations. These two enzyme polymorphisms were chosen as they are important in phase II metabolism of APAP in the liver [192,196,197]. When the ethnicity of the subjects was not noted in the source paper, the group designation was inferred from the study location. Studies were further subdivided into a training set to be used for parameter estimation (model calibration) and a test set for verification and evaluation (model validation). The studies and their classifications (Group A vs. Group B and training vs test) are listed in Table A of the appendix.

4.6.2 PBPK model description

The PBPK model structure consisted of compartments representing fat, muscle, liver, and kidney, with remaining tissues lumped [45] into either rapidly perfused or slowly perfused compartments. The PBPK model structure for this study was the same as the one in §4.2.2 and the graphical representation of the model structure is shown in Figure 4.1.1. Compartmental volumes and blood flow rates were taken from Brown et al. [55]. Compartmental volumes and blood flow rates were taken from Brown et al. 1997. Detailed descriptions of the governing equations describing each aspect of the ADME are found in Zurlinden and Reisfeld [36] and the equations themselves are listed in appendix Table B.

4.6.3 Parameter estimation

Using time-course plasma and urinary data from the designated training data set (Table A), unknown model parameters from Table 4.2.1 were estimated within the context of a Bayesian hierarchical framework [36,123]. This approach was used because it facilitated the calculation of uncertainty in both parameter values and endpoints of interest and allowed for the *simultaneous estimation* of parameter values that were shared between the groups and levels (e.g., physiological parameters) and those that were expected to differ (e.g., parameters related to metabolism and clearance). The hierarchy consisted of three levels (i) a population level, comprising all of the training set data from all of the studies; (ii) a group level, with the training data divided according the 'Group A' and 'Group B' designations described earlier; and (iii) a study level, consisting of all of the separate training set studies. Using this methodology, pharmacokinetics predictions and parameter estimates could be made and compared at each level in the hierarchy. Here, our primary concern was with examining this behavior at the group levels to develop subpopulation-specific parameter distributions.

Within the Bayesian framework, sampling was performed using a Markov chain Monte Carlo (MCMC) approach and distributions for all parameter *priors* were log-transformed and sampled as either normal or uniform distributions. When available, these distributions were based on values reported in the literature. For instance, the Michaelis-Menten constants (K_M, V_{max}) for the CYP, UGT, SULT pathways, and conjugate active transporters were taken from *in vitro* studies conducted in human liver microsomes [185], recombinant enzymes [184], or isolated rat hepatocytes [181]. When no such data were available, uninformed, uniform priors were used.

4.6.4 Comparing parameter and endpoint values between the groups

To determine which of the parameters and pharmacokinetic measures were significantly different between Group A and Group B, a Mann-Whitney U test was used. The simulated population size (N=100) approximated that from the experimental studies utilized in model development and verification (Table A). For the statistical tests, the null hypothesis was that there was no difference in the distribution for a parameter, measure, or endpoint of interest between Group A and Group B.

4.6.5 Software and computing platform

Data available from the literature in graphical form were digitized using DigitizeIt v.1.5.8 [124]. Simulations of the PBPK model equation system, including MCMC and MC analyses, were conducted using MCSim v5.4 [77]. Processing and analysis of data and simulation results was carried out using custom scripts written in Python v.2.7.2 [125], utilizing the numpy [126], scipy [66], and matplotlib [127] packages. All calculations were performed on a computational cluster running the 64-bit CentOS Linux operating system on six-gigabit linked Dell 2950 serves, each containing two quad-core 2.5-GHz Xeon processors and 64 GB of RAM.

TABLE 4.2.1. Summary of population and group parameter distributions

Description	Parameter (units)	Population	Group A	Group B
Acetaminophen Absorption				
gastric emptying time constant	T_G (hr)	N(0.33, 0.36)	N(0.385, 0.29)	N(0.401, 0.33)
G.I. perfusion time constant	T_P (hr)	N(0.0474, 0.32)	N(0.053, 0.28)	N(0.051, 0.33)
Phase I metabolism				
cytochrome P450 K_M	$K_{M\text{-}cyp}$ (μM)	N(123, 0.29)	N(124, 0.27)	N(121, 0.27)
cytochrome P450 V_{max}	$V_{M\text{-}cyp}$ (μmol/hr-$BW^{0.75}$)	N(2.69, 0.74)	N(2.54, 0.69)	N(2.84, 0.78)
Phase II metabolism: sulfation				
sulfation pathway acetaminophen K_M	$K_{M\text{-}sult}$ (μM)	N(1.14E3, 0.40)	N(1.19E3, 0.43)	N(1.23E3, 0.40)
sulfation pathway substrate inhibition K_i	$K_{I\text{-}sult}$ (μM)	N(475, 0.24)	N(465, 0.29)	N(465, 0.29)
sulfation pathway PAPS K_M	$K_{M\text{-}PAPS}$ (unitless)	N(0.348, 0.38)	N(0.284, 0.43)	N(0.316, 0.46)
sulfation pathway acetaminophen V_{max}	$V_{M\text{-}sult}$ (μmol/hr-$BW^{0.75}$)	N(443, 0.39)	N(492, 0.35)	N(386, 0.35)
Phase I metabolism: glucuronidation				
glucuronidation pathway acetaminophen K_M	$K_{M\text{-}ugt}$ (μM)	N(6.07E3, 0.35)	N(5.72E3, 0.32)	N(6.18E3, 0.34)
glucuronidation pathway substrate inhibition K_i	$K_{I\text{-}ugt}$ (μM)	N(4.95E4, 0.25)	N(4.89E4, 0.33)	N(4.88E4, 0.33)
glucuronidation pathway UDPGA K_M	$K_{M\text{-}UDPGA}$ (unitless)	N(0.335, 0.36)	N(0.275, 0.39)	N(0.299, 0.45)
glucuronidation pathway acetaminophen V_{max}	$V_{M\text{-}ugt}$ (μmol/hr-$BW^{0.75}$)	N(5.08E3, 0.32)	N(5.23E3, 0.27)	N(4.83E3, 0.29)
Active hepatic transporters				
APAP-G hepatic transporter K_M	$K_{M\text{-}APAP\text{-}G}$ (μM)	N(1.73E4, 0.27)	N(1.43E4, 0.35)	N(1.55E4, 0.36)
APAP-G hepatic transporter V_M	$V_{M\text{-}APAP\text{-}G}$ (μmol/hr)	N(3.50E4, 0.43)	N(3.63E, 0.35)	N(3.31E4, 0.37)
APAP-S hepatic transporter K_M	$K_{M\text{-}APAP\text{-}S}$ (μM)	N(2.21E4, 0.20)	N(1.94E4, 0.30)	N(2.1E4, 0.3)
APAP-S hepatic transporter V_M	$V_{M\text{-}APAP\text{-}S}$ (μmol/hr)	N(2.32E7, 0.75)	N(2.23E7, 0.73)	N(2.48E7, 0.68)
Cofactor synthesis				
UDPGA synthesis	$k_{syn\text{-}UDPGA}$ (1/hr)	N(3.63E4, 0.67)	N(3.55E4, 0.61)	N(3.62E4, 0.71)
PAPS synthesis	$k_{syn\text{-}PAPS}$ (1/hr)	N(3.71E3, 0.59)	N(3.7E3, 0.50)	N(3.6E3, 0.58)
Clearance				
acetaminophen clearance	$k_{CLC\text{-}APAP}$ (L/hr-$BW^{0.75}$)	N(0.0125, 0.34)	N(0.012, 0.23)	N(0.13, 0.26)
acetaminophen-glucuronide clearance	$k_{CLC\text{-}APAP\text{-}G}$ (L/hr-$BW^{0.75}$)	N(0.155, 0.21)	N(0.137, 0.12)	N(0.169, 0.13)
acetaminophen-sulfate clearance	$k_{CLC\text{-}APAP\text{-}S}$ (L/hr-$BW^{0.75}$)	N(0.138, 0.27)	N(0.13, 0.16)	N(0.14, 0.18)

N(a,b) denotes a normal distribution with a mean, a, and a coefficient of variation, b.

4.7.1 Model parameter values and testing

Figure 4.2.1 illustrates simulations of Group A and Group B pharmacokinetics of APAP and two of its key metabolites, acetaminophen-glucuronide (APAP-G) and acetaminophen-sulfate (APAP-S), versus data from the literature for a 20 mg/kg dose. This dose was chosen because of the relatively large amount of pharmacokinetic data available for both Group 'A' and Group 'B' populations. These plots demonstrate the good agreement between model predictions and data for all three species and also show the envelopes of model predictions that account for interstudy and interindividual variability in the data.

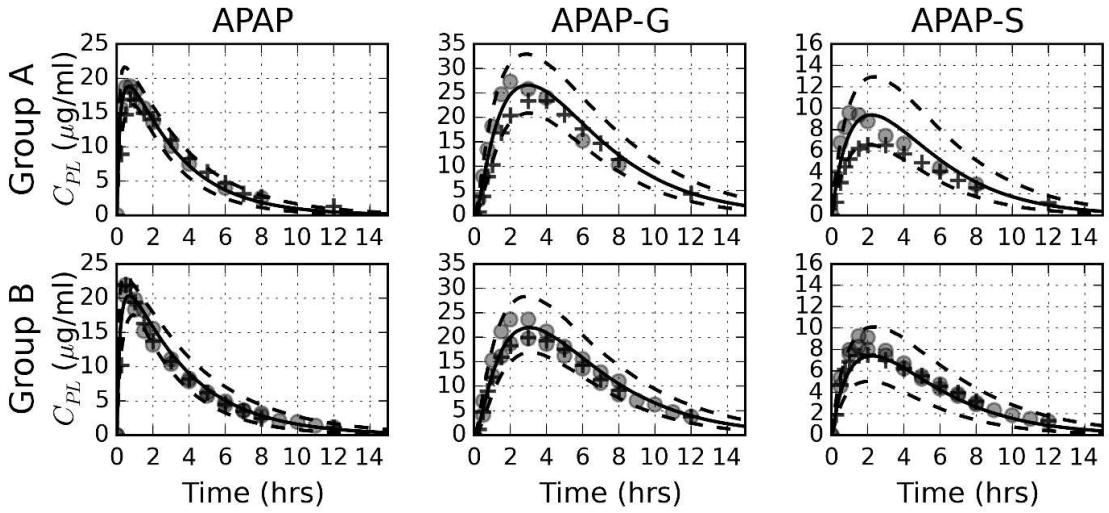

FIGURE 4.2.1. Time-course pharmacokinetics of APAP in the serum at a 20 mg/kg oral dose, where solid lines represent mean model predictions, dashed lines represent 95% confidence intervals of the predictions, circles (o) represent data used in model calibration, and the plus sign (+) represents data used for validation/testing.

Model parameter distributions leading to these predictions are listed in their respective group columns of Table 4.2.1. Using the statistical test described in §4.6.4, the null hypothesis was rejected ($p < 0.01$) for many of the model parameters associated with APAP metabolism and

clearance. In particular, there was a statistically-significant difference between the Group 'A' and Group 'B' distributions for the maximum reaction velocity, V_{max}, for sulfation and glucuronidation and the renal clearance rates for APAP-S and APAP-G.

4.7.2 Pharmacokinetic parameter comparison

To further validate the models, families of concentration-time curves were generated and analyzed numerically [38] to yield relevant pharmacokinetic measures, which were then compared to values from the literature.

Table 4.2.2 shows a comparison of several pharmacokinetic measures, including maximum concentration (C_{max}), area under the curve ($AUC_{0-\infty}$), mean residence time (MRT), clearance rate (CL_R), and percent recovery in the urine. It is important to note that the experimental results [137] were not part of the training set for the model and all parameters, with the exception of the mean residence time, were taken directly from Critchley et al. 2005. In general, there was very good agreement between the pharmacokinetic measures derived from simulations and those from experimental data for both groups.

TABLE 4.2.2. Comparison of experiment- and simulation-derived pharmacokinetic measures.

	Group A		Group B	
APAP	Experiments [137]	Simulations	Experiments [137]	Simulations
C_{max} (µg/ml)	18.7 (14.4 – 22.9)	18.99 (12.18 – 28.32)	23.8 (17.9 – 32.3)	20.56 (13.72 – 31.29)
AUC (µg-h/ml)	83.0 (56.7 – 117.1)	84.71 (42.04 – 124.97)	83.3 (50.8 – 112.6)	91.13 (49.33 – 160.67)
MRT* (hr)	3.28 (3.05 – 3.51)	3.25 (2.11 – 4.61)	3.15 (3.01 – 3.29)	3.71 (2.40 – 5.49)
CL_R (ml/min)	11.9 (4.5 – 16.4)	12.68 (7.57 – 21.24)	11.2 (5.6 – 18.1)	11.45 (6.52 – 20.10)
Recovery (%)	4.7 (2.4 – 7.6)	3.98 (1.31 – 10.26)	5.3 (3.1 – 9.0)	5.27 (1.58 – 12.33)
APAP-G				
C_{max} (µg/ml)	11.2 (7.7 – 15.1)	12.41 (6.38 – 18.62)	9.5 (5.8 – 14.8)	10.33 (5.42 – 17.20)
AUC (µg-h/ml)	90.6 (60.9 – 119.5)	94.87 (55.57 – 156.43)	76.2 (50.9 – 110.5)	79.89 (38.30 – 141.36)
MRT* (hr)	6.19 (5.69 – 6.68)	5.77 (4.38 – 7.44)	6.16 (5.18 – 6.77)	5.90 (4.29 – 7.82)
CL_R (ml/min)	140 (87 – 185)	155.8 (117.1 – 207.4)	129 (82 – 187)	142.09 (90.07 – 207.4)
Recovery (%)	59.9 (47.3 – 68.3)	57.62 (39.62 – 72.26)	55 (40.7 – 68.6)	57.61 (39.05 – 76.60)
APAP-S				
C_{max} (µg/ml)	4.43 (3.18 – 6.02)	6.24 (3.10 – 11.85)	5.8 (3.15 – 7.41)	4.90 (2.39 – 9.07)
AUC (µg-h/ml)	36.7 (24.2 – 50.0)	41.81 (16.18 – 97.13)	40.4 (25.2 – 62.0)	34.55 (11.30 – 72.36)
MRT* (hr)	5.92 (5.35 – 6.49)	4.85 (3.49 – 6.32)	5.90 (5.38 – 6.33)	5.12 (3.25 – 7.09)
CL_R (ml/min)	160 (85 – 217)	150.4 (110.6 – 204.4)	148 (117 – 196)	140.2 (98.2 – 200.1)
Recovery (%)	27.7 (19.8 – 41.9)	24.78 (12.82 – 43.29)	34.2 (22.3 – 46.4)	22.98 (8.61 – 39.46)

*Calculated from *in vivo* data

Results are presented as mean (95% confidence interval range).

4.7.3 Model predictions

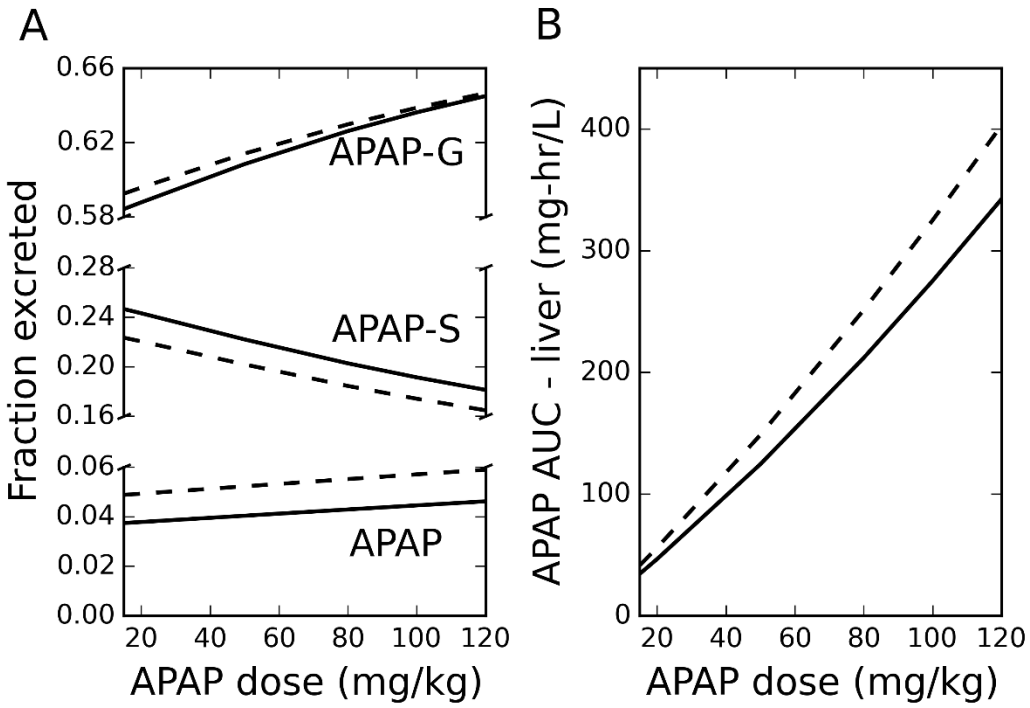

FIGURE 4.2.2 Simulation results: a fraction excreted for the acetaminophen (APAP) and its two conjugates: acetaminophen-glucuronide (APAP-G) and acetaminophen-sulfate (APAP-S), with APAP-G and APAP-S presented as acetaminophen equivalents, and b the area under the concentration–time curve extrapolated to infinity (AUC) of APAP in the liver. For both panels, solid and dashed lines represent population means for Group A and Group B, respectively.

Beyond recapitulating results from existing studies, a key feature of the models is that they can be used to estimate pharmacokinetic quantities beyond those available experimentally. One key indicator of APAP metabolism is fraction excreted. Figure 4.2.2A shows this measure as a function of dose for APAP and two of its metabolites. Because of hepatic elimination of APAP through phase I metabolism, these fractions do not sum to one.

It is known that APAP can undergo cytochrome P450-mediated bioactivation to the glutathione depleting, putative toxicant *N*-acetyl-*p*-benzoquinone imine (NAPQI). Because this

metabolic process occurs in the liver, quantifying concentrations of species in this organ are important in understanding toxicity. Thus, the PBPK models were employed to make liver-specific pharmacokinetic predictions, where parent APAP was used as a surrogate for the toxic species NAPQI. Figure 4.2.2B shows the AUC of APAP in the liver (AUC_{liver}) as a function of dose for the two groups. With increasing dose, there is a increase in the divergence between AUC_{liver} for the two groups, and at a dose of 120 mg/kg, this difference is statistically significant ($p < 0.01$).

To ascertain which of the model parameters were most influential in this difference in AUC_{liver} between the groups, a sensitivity analysis was carried out and a Pearson correlation coefficient, *r*, computed for each model parameter. Results from this analysis indicated that parameters most influencing this endpoint ($|r| > 0.2$) were all related to APAP metabolism, including the Michaelis-Menten parameters associated with the glucuronidation and sulfation pathways and the rate parameter for UDPGA synthesis.

4.8 DISCUSSION

As illustrated in Figure 4.2.1 and Table 4.2.1, the PBPK models developed in this study produce predictions for time-course concentrations and summary parameters that are in good agreement with experimental measurements for both ethnic groups across numerous pharmacokinetic studies in humans.

Using the validated PBPK models, predictions were made for two pharmacokinetic quantities useful in characterizing APAP ADME. First, as shown in Figure 4.2.1A, the urinary excretion of APAP and two key metabolites was simulated as a function of dose. The convergence of the Group A and B curves for excretion of the APAP-G conjugate at higher doses is indicative of the saturation of the glucuronidation pathway. Comparable lines for parent

APAP and APAP-S do not converge at higher doses, indicating differences in metabolism between the groups, even at higher doses.

Second, the AUC of APAP in the liver was estimated as an indicator of toxicity potential. As seen in Figure 4.2.1B, the AUC for the groups increasingly diverges as the dose increases. This difference in AUC is in agreement with results found experimentally [137]. These predicted differences in both urinary fate and APAP AUC could be due to a number of factors, including disparities in diet, nutritional status, alcohol consumption, and gender. However, such a disparity could be attributable to the diminished glucoronidation capacity of Group B subjects relative to those in Group A owing to differences in allele abundance for the UGT enzyme between the two groups. Specifically, for APAP glucuronidation, UGT1A6 is a high-affinity, low capacity isozyme [200] and consists of three alleles, with the wild-type UGT1A6*1 allele having the highest affinity towards phenols [197], like APAP. On the other hand, UGT1A9 is a low-affinity, high-capacity isozyme [200] for APAP glucuronidation, with UGT1A9*1 representing the wild-type allele. The difference in abundances of these allozyme between ethnically diverse groups can contribute to the divergence in the resulting APAP pharmacokinetics between these groups. It has been found that Group B subjects are more likely to contain the wild-type allele compared to their Group A counterparts [197]. This suggests that, at lower APAP doses, Group B subjects may metabolize a larger percentage of APAP to APAP-G compared to those in Group A, while at higher doses, glucuronidation may be diminished owing to saturation of the UGT1A6 isozyme [200]. Conversely, Group A subjects have a higher percentage of the wild-type UGT1A9 allele [199], allowing for greater glucuronidation at high doses, resulting in lower APAP liver concentrations compared to those in the Group B subpopulation.

Knowledge of group-specific APAP AUC in the liver has implications for targeted treatment of susceptible populations. In this study, the Group B subjects generally showed lower metabolizing capacity compared to those in Group A due to the differences in the glucuronidation pathway, suggesting that the former group may be more susceptible to APAP-induced toxicity. While these differences in glucuronidation are subtle, the use of a hierarchical Bayesian methodology allowed quantitation of these effects on the tissue-specific pharmacokinetics. These methods could be extended to patients with an even greater reduction in UGT activity, such as those with Gilbert's Syndrome [192,193,197]. Using available pharmacokinetic data, additional populations can be introduced to the hierarchical framework to determine APAP toxicity risks and recommended dosing regimens for a given population.

Lastly, predictions of the concentrations of the two APAP conjugates, APAP-G and APAP-S, can be useful clinically because these compounds have longer half-lives in the serum than the parent drug. In particular, monitoring of potential acetaminophen toxicities are based on a determination of APAP concentration in the serum [174]. However, due to the relatively short mean residence time of APAP in the blood, this indicator can become uninformative at longer times post dosing, whereas the half-lives of APAP-G and APAP-S are almost twice as long, providing potentially more informative measures related to possible adverse health effects [39].

Though the study detailed here provided evidence that a hierarchical PBPK modeling approach could be used to characterize subtle changes in pharmacokinetics between ethnic groups, the results should be interpreted in light of several limitations in the data and methodology. First, actual allele frequencies and abundances for individuals in each group were not available. While members of Group A were *more likely* to express the wild-type UGT1A9 allele, genetic testing information was not available to test this assumption. Second, in many cases, the ethnicities of

study participants were assumed based solely on study location. Lastly, it was assumed that disparities in measured pharmacokinetic characteristics between the groups was due to differences in metabolism, as opposed to factors such as lifestyle, diet, and nutritional status.

4.9 CONCLUSION

The objective of this research was to develop subpopulation-specific PBPK models to help clarify the ADME of APAP for two groups expected to differ in alleles relevant to the metabolism of this drug. To our knowledge, this is one of the first usages of PBPK modeling to quantify the pharmacokinetic implications of these types of differences. This modeling approach was used to estimate distinct metabolism and clearance parameter sets for each of the groups and predict pharmacokinetics and pharmacokinetic measures that were in good agreement with those from the literature.

Although experiments are vital in elucidating pharmacokinetics, the use of validated PBPK models can aid in predicting the tissue-specific disposition of drugs and their metabolites and rigorously interpolating and extrapolating between and across doses and dosing regimens. The use of subpopulation-specific models can further enhance this understanding by providing results with less uncertainty than generalized models through the use of data and model parameters particular for the group(s) of interest. Additionally, by utilizing a hierarchical Bayesian approach, interindividual, interstudy, and intergroup variability can be quantified and used to direct the design of additional experiments and inform a more rational interpretation of model results.

Ultimately, although the models described here do not directly compute measures or biomarker concentrations indicative of APAP-induced liver injury (e.g., levels of alanine aminotransferase, glutathione *S*-transferase alpha, or arginase 1), they could be linked with

appropriate pharmacodynamic models [163,165,194] to make toxicity predictions in a manner that rationally incorporates differences in APAP ADME between individuals and susceptible subpopulations of interest and predicts population-specific pharmacodynamic outcomes.

4.10 A Novel Approach for Estimating Ingested Dose Associated with Acetaminophen Overdose

As described earlier, acetaminophen (paracetamol, *N*-acetyl-para-aminophenol, APAP) is one of the most widely used analgesic and antipyretics in the world. Owing to its abundant usage, APAP is the principle cause of acute liver failure in both the United Kingdom [88,90] and United States [88,89]; moreover, ingestion of this drug is the most common, non-opioid poisoning that results in admission to the hospital in the US, with the majority of these ingestions involving self-harm attempts [90,201].

The current standard for evaluating acute APAP overdose begins with risk stratification using the Rumack-Matthew nomogram [174]. To use the nomogram, parent APAP is measured in the serum, plotted against the time of ingestion, and compared to the "150 μg/ml" line; if the concentration falls above the line, the patient is considered at risk for liver injury and treatment with *N*-acetylcysteine (NAC) is indicated [202]. There are several commonly used NAC treatment protocols, including the 21 hour intravenous protocol, the 72 hour oral protocol, and "patient tailored" protocols where treatment is continued until laboratory and clinical endpoints are met.

While treatment for APAP overdose in an emergency setting does not absolutely require knowledge of the ingested dose, this information can be important for long-term, individualized

---

This work was performed jointly with the full list of co-authors available in [39]

management of patients. Occasionally, a patient may claim to have ingested a therapeutic dose, while the serum concentration suggests overdose [203,204]; however, the pharmacokinetic parameters that have been used to calculate the dose were derived from studies of therapeutic dosing, which may not accurately portray APAP pharmacokinetics in an overdose scenario. Similarly, there are currently no methods for validation of history for case reports claiming APAP toxicity following therapeutic dosing. Recent studies [204,205] noted that, while there is an overall correlation between reported dose and serum concentration, some patients reported ingesting doses that are not consistent with the measured concentrations based the standard pharmacokinetic parameters for APAP. Moreover, a retrospective study of over 1200 APAP overdose patients [206] concluded that self-reported dose alone is a poor assessment tool in determining the need for overdose treatment. In sum, knowledge of the ingested APAP dose following self-harm poisoning could help inform treatment plans, aid in validating the history in reports of toxicity, and identify patients who have overdosed, but have provided inaccurate dosing histories.

Here we propose a method for estimating administered dose using APAP serum concentration and a computational method based on physiologically-based pharmacokinetic (PBPK) modeling. PBPK modeling is commonly used to predict time-course tissue-specific concentrations of species based on a specified input dose or exposure [160,207]. This mode of utilizing the model is often called *concentration prediction* (or *forward dosimetry*). In contrast, for dose estimation (also known as *dose reconstruction* or *reverse dosimetry*), measured levels of the biomarker of interest (e.g., concentration of the parent drug in the blood) are specified as the known quantities and the ingested dose is treated as the unknown. By using Bayesian inference to compute model parameters, inter-study and inter-subject variability can be included in the

specified data, and uncertainties in model outputs can be quantified [77,208]. Bayesian approaches have been used previously in a few similar contexts: with PBPK models to calculate exposures to environmental toxicants [183,209,210] and with compartmental models to incorporate estimates of the veracity of the patients' dosing history to estimate the dose of a drug [211].

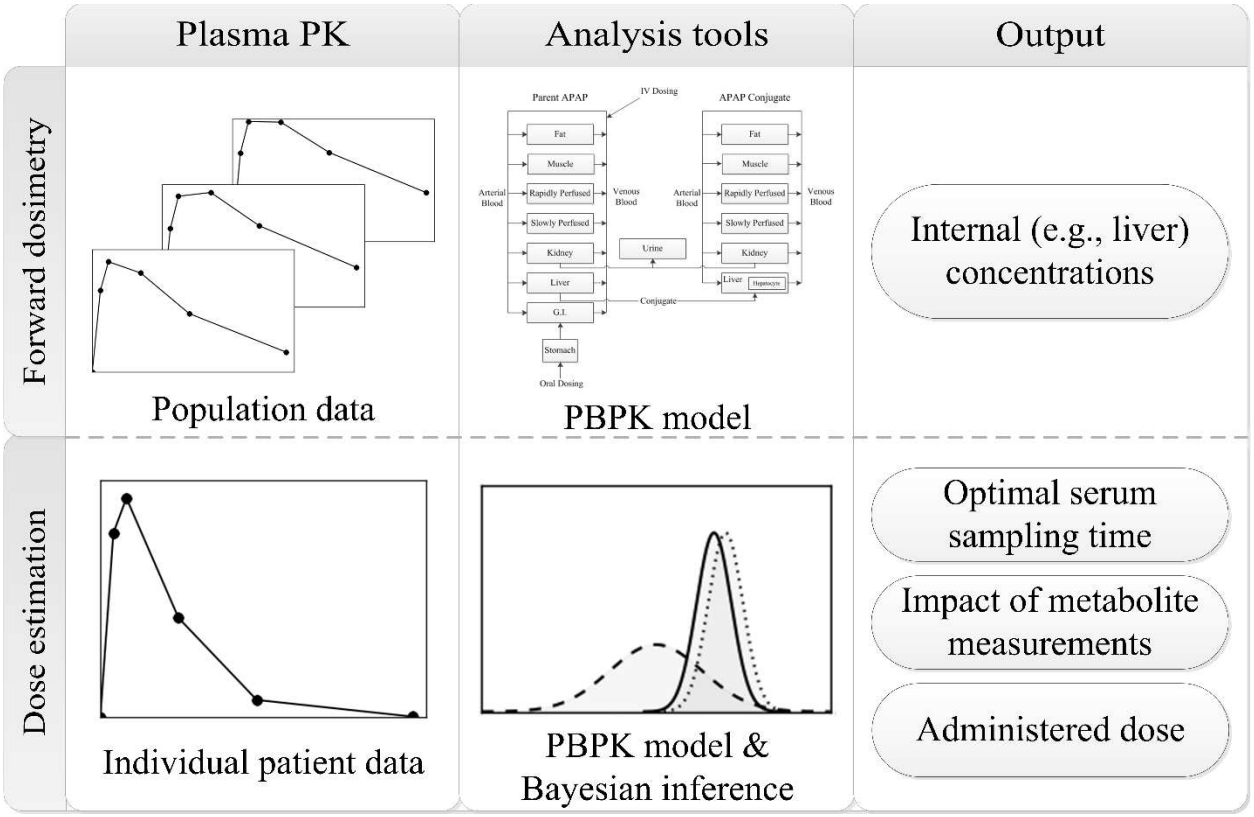

FIGURE 4.3.1. Overview of the analysis framework. The horizontal rows represent the two different modes of analysis, with the input data, analysis tools, and simulation output portrayed in the left-hand, center, and right-hand panels, respectively. In particular, the upper row represents the methodology for the concentration prediction studies. Here, pharmacokinetic data from multiple studies are used to determine relevant parameter distributions in the PBPK model. Using the model, internal concentrations in the tissue of interest can be estimated and population variability characterized. The lower row illustrates the approach used for the dose estimation studies. Here, a blood sample from an individual patient is obtained. Using the calibrated PBPK model and Bayesian inference, the administered dose, along with optimal sampling times and measurable biomarkers, can be determined.

In this study, we extended our PBPK model created previously for therapeutic doses of APAP [36] to overdoses and developed a Bayesian inferential framework for the two distinct modes of analyses described above (Figure 4.3.1). Specifically, we first used the framework in *concentration prediction* mode to (i) predict parent APAP and metabolite concentrations in plasma and compare these predictions to data from clinical measurements over a range of dosing conditions and (ii) relate predicted APAP concentrations in the plasma and liver over time. We then employed the computational tool in *dose estimation* mode to (i) determine the optimal time for blood sampling to minimize the error in a dose estimate, (ii) quantify the potential role of inclusion of metabolite concentration on dose estimates, and (iii) predict APAP doses and compare them to patient data collected in an emergency setting [39].

4.11 METHODS

4.11.1 Physiologically-based pharmacokinetic modeling

4.11.1.1 Acetaminophen overdose data

We utilized human pharmacokinetic data from a number of high-dose (23 to 41 g) studies [141,212–214] and a comprehensive set of therapeutic-level (250 mg to 5.5 g) studies [36] to re-parameterize the model from Zurlinden and Reisfeld [36], allowing the resulting model to have applicability over a wide range of doses. The data were divided into two distinct sets: (i) a training set, used for model parameter estimation, and (ii) a test set, reserved for evaluation and comparison to model predictions. A summary of the data sets used in the analyses is contained in Table A of the appendix.

Additionally, APAP overdose data from the Rocky Mountain Poison and Drug Center [215] were used for model verification and comparison to predicted dose estimates. These data were collected from patients admitted to the hospital for overdose treatment following an acute

ingestion of APAP. Because the doses were self-reported and the time of ingestion was not precisely known, these data were held out of the training set. These self-reported doses ranged from 9-100 grams of orally administered APAP and served as realistic case studies for model testing.

4.11.1.2 Model Formulation

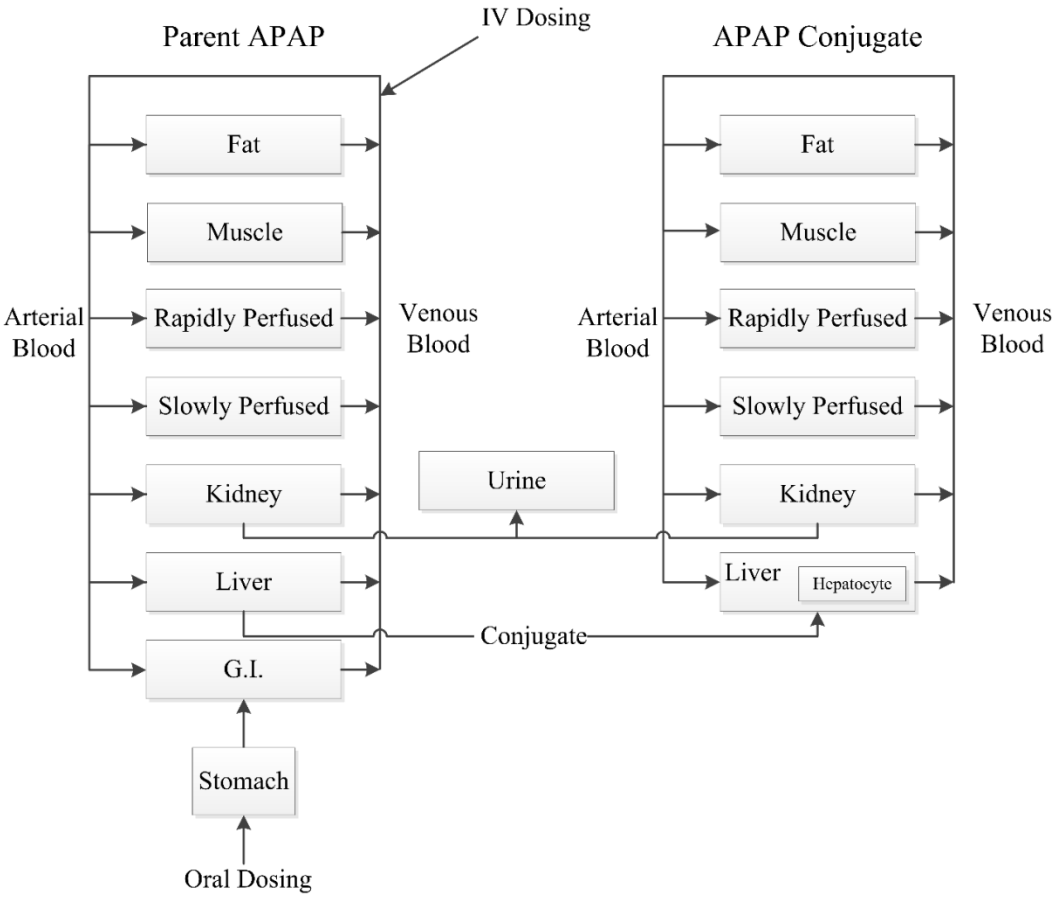

FIGURE 4.3.2. APAP Overdose PBPK model structure

The PBPK model structure used in this study (Figure 4.3.2) and most of the model equations were the same as those developed previously for therapeutic dosing [36]. The full set of governing equations is available in Table B of the appendix.

TABLE 4.3.1. Model parameters. N(a,b) denotes a normal distribution with a mean, a, and a coefficient of variation, b; U(a, b) denotes a uniform distribution with minimum and maximum values a and b, respectively. When a prior was not available in the literature (indicated by a dash in the reference column), a broad distribution was used to bound the likely parameter value.

Description	Parameter(units)	Prior	Posterior	Reference
Absorption				
drug dissolution rate	a_o (1//hr)	U(1, 10)	N(4.82, 0.26)	[216]
body weight absorption scaling factor	α (unitless)	U(1E-3, 1)	N(0.16, 0.71)	[168]
gastric emptying time constant(fasted state)	$T_{G\text{-}fast}$ (hr)	N(0.23, 0.5)	N(0.15, 0.20)	[168]
gastric emptying time constant(fed state)	$T_{G\text{-}fed}$ (hr)	-	1	[217]
Phase I metabolism				
cytochrome P450 K_M	(μM)	N(130, 1)	N(125,0.21)	[184]
cytochrome P450 V_{max}	(μmol/hr-$BW^{0.75}$)	U(0.14, 2900)	N(3.68,0.76)	–
Phase II metabolism: sulfation				
sulfation pathway K_M	(μM)	N(300, 1)	N(460,0.22)	[185]
sulfation pathway substrate inhibition K_i	(μM)	N(526, 1)	N(498,0.21)	[176]
sulfation pathway PAPS K_M	(unitless)	N(0.5, 0.5)	N(0.37,0.25)	–
sulfation pathway V_{max}	(μmol/hr-$BW^{0.75}$)	U(1, 3.26E6)	N(224,0.25)	–
Phase I metabolism: glucuronidation				
glucuronidation pathway K_M	(μM)	N(6.0E4, 1)	N(6.57E3,0.19)	[185]
glucuronidation pathway substrate inhibition K_i	(μM)	N(5.8E4, 0.25)	N(5.25E4,0.22)	[175]
glucuronidation pathway GA K_M	(unitless)	N(0.5, 0.5)	N(0.36,0.24)	–
glucuronidation pathway V_{max}	(μmol/hr-$BW^{0.75}$)	U(1, 3.26E6)	N(5.21E3,0.17)	–
Active hepatic transporters				
APAP-G hepatic transporter K_M	(μM)	N(1.99E4, 0.3)	N(1.57E4,0.23)	[181]
APAP-G hepatic transporter V_M	(μmol/hr)	U(1.09E3, 3.26E6)	N(1.02E5,0.51)	–
APAP-S hepatic transporter K_M	(μM)	N(2.29E4, 0.22)	N(2.01E4,0.22)	[181]
APAP-S hepatic transporter V_M	(μmol/hr)	U(1.09E3, 3.26E6)	N(1.03E7,1.23)	–
Cofactor synthesis				
UDPGA synthesis	(1/hr)	U(1, 4.43E5)	N(5.32E4,0.55)	–
PAPS synthesis	(1/hr)	U(1, 4.43E5)	N(3.14E3,0.45)	–
Renal elimination				
clearance	(L/hr-$BW^{0.75}$)	U(2.48E-3, 2.718)	N(0.012,0.27)	–
glucuronide clearance	(L/hr-$BW^{0.75}$)	U(2.48E-3, 2.718)	N(0.13,0.17)	–
sulfate clearance	(L/hr-$BW^{0.75}$)	U(2.48E-3, 2.718)	N(0.16,0.19)	–

The differences are related to the mechanistic and mathematical description of APAP absorption and the estimated parameters associated with the model equations (Table 4.3.1). As confirmed previously [36], under therapeutic conditions, absorption following oral administration of APAP is well described using the "averaged model" (i.e., a well-stirred compartmental model) from Levitt [168]; however, under overdose conditions, there is a significant delay in T_{max} [150] that cannot be accounted for with this model. A biologically-plausible mathematical description for APAP absorption that accounts for this lag consists of terms accounting for drug dissolution in the stomach, first order gastric emptying to the GI tract, and passive diffusion over the gut lumen [218]:

$$\begin{aligned}
\frac{dA_{ST,S}^{APAP}}{dt} &= I(t) - k(t)\cdot A_{ST,S}^{APAP} \\
\frac{dA_{ST,Aq}^{APAP}}{dt} &= k(t)\cdot A_{ST,S}^{APAP} - \left(\frac{1}{T_G}\right) A_{ST,\mathrm{Aq}}^{APAP} \\
\frac{dA_{G}^{APAP}}{dt} &= \left(\frac{1}{T_G}\right) A_{ST,\mathrm{Aq}}^{APAP} + Q_G\left(C_A^{APAP} - C_{V-G}^{APAP}\right)
\end{aligned} \tag{4C.1}$$

Here, $A_{ST,S}^{APAP}$ and $A_{ST,Aq}^{APAP}$ represents the amount of APAP in the stomach in solid and aqueous phases, respectively, *I(t)* is the initial rate of dosing to the stomach and T_G is the gastric emptying time. The function *k(t)* is the time-dependent rate of APAP dissolution, which was extensively studied *in vitro by* Özkan et al [216] who found that dissolution rates were best described using the Hixson-Crowell (HC) model [219,220]:

$$k(t) = \begin{cases} \dfrac{3a}{1-a\,t} & , \quad t \le \dfrac{1}{a} \\ 0 & , \quad t > \dfrac{1}{a} \end{cases} \tag{4C.2}$$

with $a = \sqrt[3]{a_0\left(\frac{D}{BW^{\alpha}}\right)}$, where D is the ingested APAP dose, BW is the body weight of the subject, and a_0 and α are constants that were fit in this study to available data [141,212,214]. This specification for drug dissolution describes the release rate of a drug with a constantly changing surface area. For a large amount of drug in the stomach, this dissolution rate will be governed by the surface area exposed to the aqueous solution and will be proportional to the cubed-root of the initial mass. In addition, drug formulation will impact the rate of dissolution, and in this study, only immediate release (IR) APAP formulations were considered. The amount of APAP in the gut compartment, A_G^{APAP}, is described through a simple gut-to-blood perfusion description using a blood flow rate, Q_G, arterial blood concentration, C_A^{APAP}, and venous gut concentration, C_{V-G}^{APAP}. The venous gut concentration is determined using the gut:blood partition coefficient, where $C_{V-G}^{APAP} = C_G^{APAP} / P_{gut:blood}$. This tissue:blood partitioning ratio assumes that equilibrium has been reached between the venous blood and tissue. Equipartitioning of species between the serum and red blood cells was assumed and the effect of clotting factors and protein binding in the blood were neglected. Finally, by adjusting the gastric emptying time, T_G, simulations for fasted and fed states could be conducted. Because APAP pharmacokinetic studies generally occur when the patient is in a fasted state, T_G under those conditions was determined through the Bayesian calibration methodology, while that for the fed state was assumed to be one hour [217].

4.11.1.3 Parameter estimation

Parameters for the PBPK model were determined using a hierarchical Bayesian model utilizing a Markov chain Monte Carlo sampling procedure [36,123,183,221], which facilitates quantitation of inter-study and inter-subject variability. The specific prior and posterior parameter distributions are presented in (Table 4.3.). Five Markov-chains were run for 100,000

iterations per chain. Posterior parameter distributions were determined by combining the final 30,000 iterations of each chain. Convergence was assessed using a Gelman-Rubin reduction factor [73] with a maximum threshold of R = 1.05.

4.11.1.4 Dose estimation studies

Similar to previous exposure estimation studies [183,209,210], APAP dose reconstruction was cast into the form of a parameter estimation problem. In this scenario, rather than determining population distributions for PBPK model parameters such as enzyme V_{max} or drug clearance rate constants, the Bayesian methodology was used to determine a posterior distribution for the ingested APAP dose, given a biomarker concentration, such as APAP concentration measured in the serum. APAP dose reconstruction was investigated for two applications: (i) determining the optimal sampling time for dose reconstruction with and without APAP conjugate measurements, and (ii) reconstructing APAP doses based on measured serum concentrations and comparing them to known or self-reported dose values from patients.

4.11.2 Optimal sampling time

As represented in Figure 4.3.3, the procedure for determining optimal sampling time for dose reconstruction was as follows. Following verification and evaluation, the PBPK model was used to simulate time-course serum concentrations for the parent drug and two metabolites, *N*-acetyl-para-aminophenol glucuronide (APAP-G) and *N*-acetyl-para-aminophenol sulfate (APAP-S), following a single oral 400 mg/kg dose in a 70 kg person. serum concentrations were numerically sampled from these synthetic data and used to reconstruct a probability distribution for the initial dose.

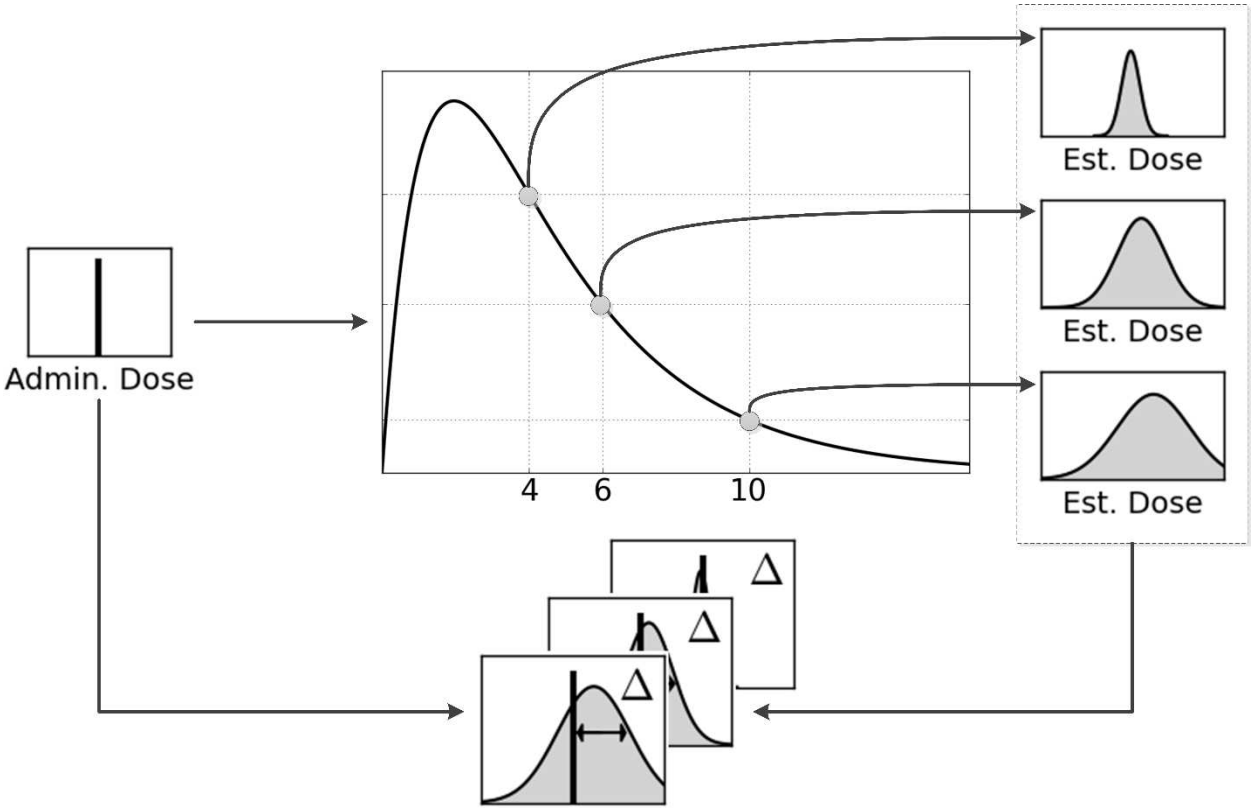

FIGURE 4.3.3. Overview of the dose reconstruction methodology

These simulation results were aggregated to create a set of well-characterized "synthetic data" to be used subsequently. Next, For a given time point, serum APAP was either sampled alone or in combination with APAP-G and/or APAP-S. This represents a scenario in which a single blood sample is taken and analyzed for parent APAP alone or with either or both of the conjugates. Lastly, the reconstructed probability distribution for APAP dose was compared to the known initial dose to generate a measure of reconstruction accuracy. This method is similar to studies in which results from a population PBPK model are sampled numerous times to determine an optimal blood sampling time for PBPK model parameter estimation [222–224]; however, rather than comparing a predicted pharmacokinetic endpoint, such as area under the curve or C_{max}, the resulting dose prediction was compared to a known ingested dose.

In addition to blood sampling at a single time point, this methodology was also used to investigate how utilizing multiple blood samples would impact the error in the APAP dose prediction. In this scenario, two time points comprised the data for the Bayesian inference. In this series of simulations, a serum sample taken at four hours served as the initial point, and a second sample was taken at a variable time interval after that. As in the previous study, the effect of sampling metabolites in addition to the parent APAP was systematically investigated.

4.11.3 Determining the administered dose

The final aspect of this study involved estimating the ingested APAP dose based on measurements from therapeutic/supratherapeutic trials [36], well-controlled clinical overdose studies [214], and an emergency setting [215]. The dataset from the emergency setting included many cases where the patient did not know the quantity of APAP ingested. However, in a substantial number of the cases (N=61), the patient could approximate the amount of APAP ingested and these values could be compared to those from the computational dose reconstruction.

4.11.4 Statistical analysis

The Bayesian inference method results in a posterior probability distribution for the administered dose prediction. However, the true initial dose is a single point parameter. We used the mean square error (MSE), Δ, as a measure of the difference between the predicted probability distribution and the "true dose",

$$\Delta = \frac{1}{N}\sum_{i=1}^{N}\left(\hat{D}_i - D\right)^2 \tag{4C.3}$$

where $\hat{D}_i$ represents the distribution of predicted doses, *i* represents an iteration of the posterior chain, *N* is the number of values comprising the distribution, and *D* is the actual dose taken by

the patient. Based on the MSE, Δ quantifies the uncertainty in the dose prediction by accounting for the variance in the resulting dose distribution [224]. In this study, the MSE was used principally to help identify optimal blood sampling times. For this optimization application, the MSE was preferable to measures such as the mean absolute error because of its favorable mathematical and computational properties, such as its continuity and differentiability.

4.11.5 Software and computing platform

Concentration prediction and dose estimation simulations were conducted using MCSim v5.4 [77], an open source package for the solution of statistical and dynamic models, Monte Carlo stochastic simulations, and Bayesian inference simulations. Processing, analysis, and visualization of data and simulations results were carried out using scripts written in Python v.2.7.2 [125], utilizing the numpy [126], scipy [66], and matplotlib [127] packages. All calculations were performed on a compute cluster running the 64 bit CentOS Linux operating system on six gigabit-linked Dell 2950 servers, each containing two quad-core 2.5 GHz Xeon processors and 64 GB of RAM.

4.12 RESULTS

4.12.1 Concentration prediction studies

To assess the accuracy of the PBPK model, predictions of plasma concentrations, C_{PL}, of parent APAP and two major metabolites, APAP-G and APAP-S, were compared to serum concentration data acquired in clinical studies. Figure 4.3.4 displays the comparison at 20 mg/kg (therapeutic), 80 mg/kg (supratherapeutic), and 400 mg/kg (overdose) for a 70 kg adult human, including the uncertainty in the model predictions. Within the PBPK model, serum and plasma concentrations were assumed to be identical (see *Methods*, §4.11).

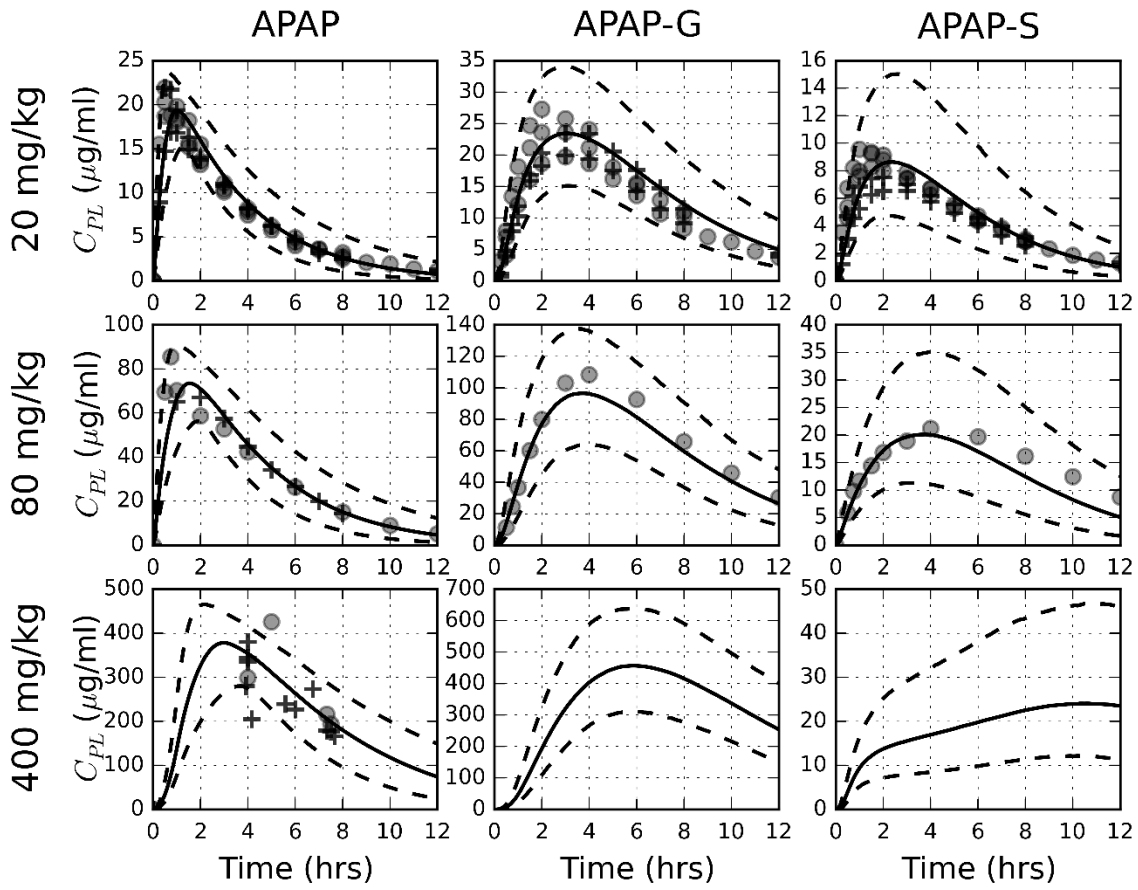

FIGURE 4.3.4. Comparison of model simulations to serum concentration data following a single oral dose of APAP administered to an adult patient weighing 70 kg. The solid and dashed lines represent mean and 95% prediction interval simulation results, respectively. Data from the training set are represented by filled circles (o), while data from the test set are denoted by the plus sign (+). Metabolite data were not available for doses greater than 80 mg/kg.

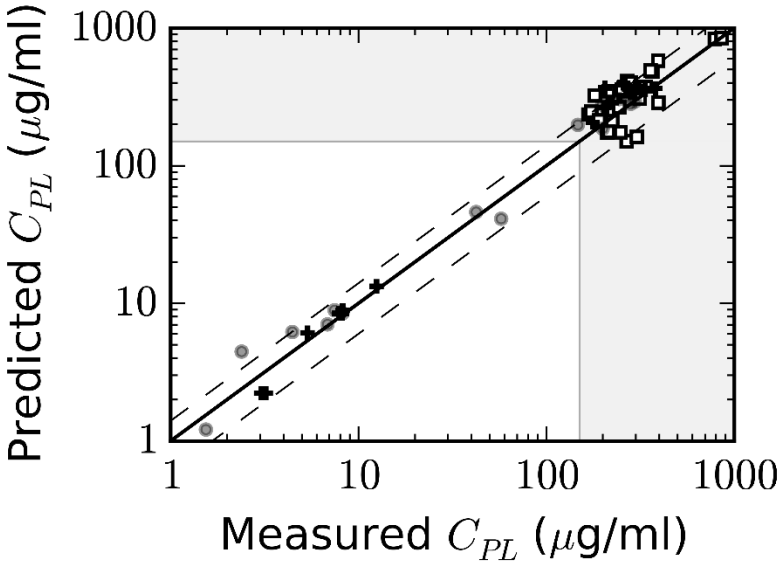

FIGURE 4.3.5. Comparison of model predictions and experimental data for APAP serum concentrations at four hours post dosing, where APAP overdose is demarcated with the dashed lines at 150 µg/ml, with concentrations in the shaded area representing potential overdoses. Data from the training and test set are represented as filled circles (o) and plus signs (+), respectively. Open squares (□) represent data from the self-reported overdose data set.

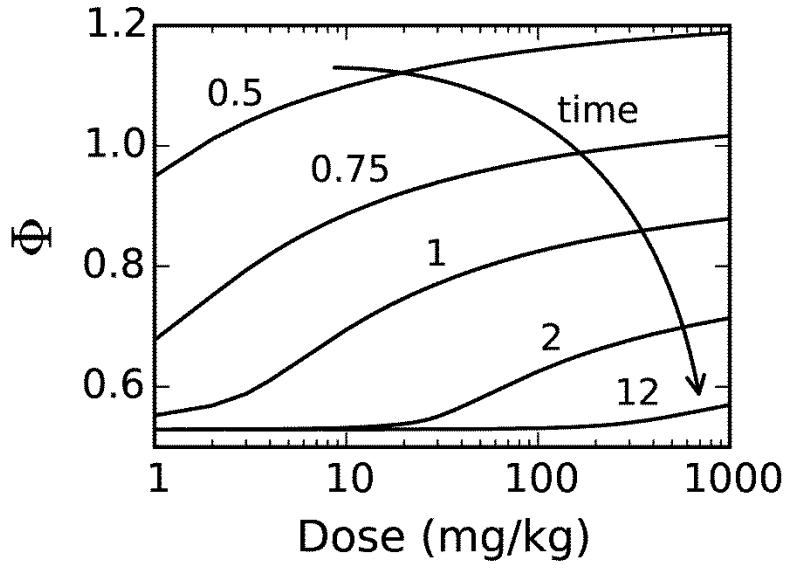

FIGURE 4.3.6. Model simulation results quantifying the ratio of liver-to-plasma APAP concentrations as a function of the APAP dose

Because a four-hour APAP serum sample is the most widely used for assessing potential APAP overdose [174], simulations were conducted and results compared to clinical and emergency setting data available across three orders of magnitude of doses at this time point (Figure 4.3.5).

Finally, one of the primary attributes of the PBPK methodology is the ability to predict and characterize tissue-specific concentrations of species of interest. Using the PBPK model, time-course simulations for APAP concentrations in both the liver and serum were conducted over the range of doses presented in Figure 4.3.6. Figure 4.3.6 depicts the dose-response curve for the ratio of liver-to-plasma APAP concentrations, $\Phi = C_{liver} / C_{plasma}$, at several times following APAP administration.

4.12.2 Dose estimation studies

4.12.2.1 Optimal sampling time

The first dose estimation study concentrated on quantifying the effect of sampling time and choice of analytes on the accuracy of the APAP dose estimation. To estimate the optimal time at which to draw a blood sample, doses were reconstructed by computationally sampling APAP and/or APAP-G and APAP-S at a single time point or at two time points. When two time points were used, the first was fixed at four hours and the second was sampled at a specified time point after that, with a range for the second time point of 4.5 to 11 hours post-dosing. Results from these reconstructions are shown in Figure 4.3.7. Here, 400 mg/kg served as the known dose, and a smaller mean squared error, Δ, represents less error in the reconstructed dose. APAP-S results were not included, as they did not alter the error for the reconstructions. Through a large set of additional simulation studies, it was found that the overall pattern for these results did not change at when the initial dose was varied.

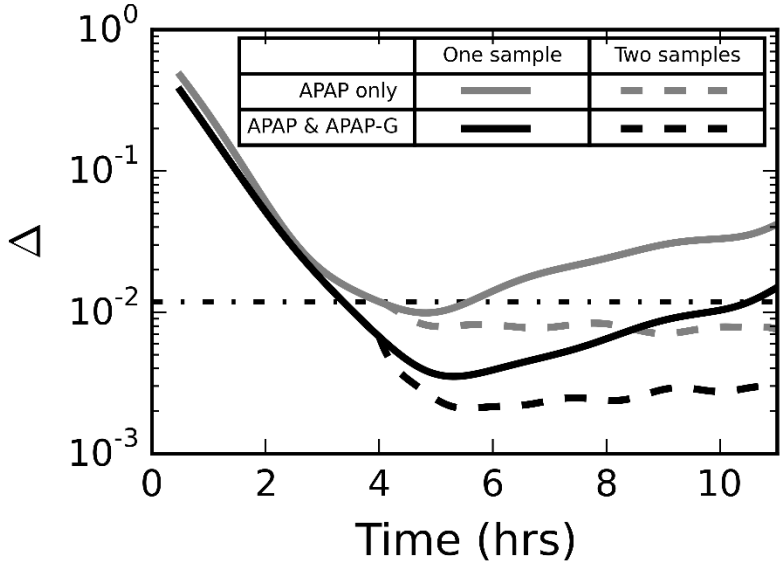

FIGURE 4.3.7. Accuracy of dose reconstruction as a function of time at which the blood is sampled. Light grey lines represent samples where only parent acetaminophen is measured, while black lines represent both APAP and APAP-G being used for dose reconstruction. Solid lines represent the dose reconstruction for a single time point and dashed lines represent reconstructions where two serum time points are used, one at four hours and one at some time later time. The dot-dashed line represents the estimated mean squared error for the standard sample protocol (acetaminophen alone measured at four hours post dosing).

4.12.2.2 Determining the administered dose

The second dose estimation study focused on dose estimation using data from both a well-controlled clinical environment and an emergency setting. As discussed previously, the current protocol for treating APAP overdose involves measuring APAP concentrations in the serum at four hours post dosing. Figure 4.3.8 shows the comparison between the reported APAP dose and the mean predicted dose using the computational model. These comparisons include data from well-controlled clinical studies and self-reported doses from an emergency room setting.

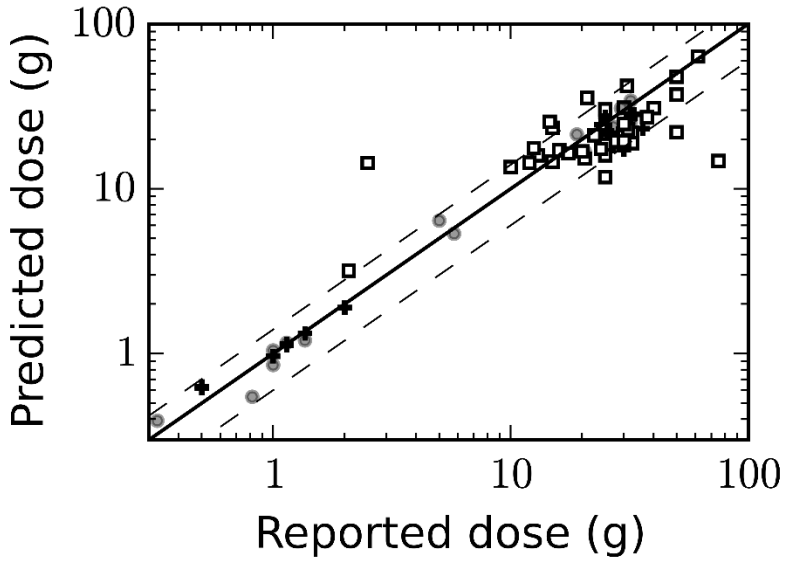

FIGURE 4.3.8. Predicted ingested dose and self-reported patient dose at four hours post dosing. Data from the training set are represented by filled circles (o), data from the test set are denoted by the plus sign (+), and values from self-reported acetaminophen overdose cases are represented by open squares (□)

4.13 DISCUSSION

Two significant objectives were achieved in this study that have potential applications to clinical pharmacology and therapeutics: first, a PBPK model was developed and evaluated to predict APAP pharmacokinetics in humans under overdose conditions; and second, this model was utilized as part of a methodology to estimate ingested dose and its uncertainty based on the measured concentration of APAP and/or its metabolites in a serum sample.

4.13.1 Concentration prediction studies

Because the PBPK model was calibrated using an extensive set of human pharmacokinetic data and incorporated mechanistically-based descriptions of physiological processes, it was capable of providing accurate simulations of APAP pharmacokinetics over a large range of ingested doses. This is demonstrated in Figure 4.3.4, in which model predictions

for APAP pharmacokinetics show good agreement with data from not only the training (calibration) data set, but also a large independent test set.

In addition to parent APAP, the model was used to make time-course predictions for two significant metabolites, APAP-G and APAP-S. At the 20 mg/kg and 80 mg/kg APAP dosing levels, model predictions agreed well with measured values for the metabolite concentrations. At 400 mg/kg, no metabolite data were available; however, owing to the metabolism mechanism implemented in the model [36], which included bi-substrate enzyme kinetics coupled with cofactor depletion and synthesis, model predictions show that APAP-S concentrations do not decrease at later times. This reduction in the rate of APAP-S formation is in accord with results from experimental studies[185,189] and is consistent with the depletion of the PAPS cofactor seen in APAP dosing studies in rodents[187,225].

As noted above, when assessing potential APAP toxicity, a four-hour serum APAP concentration conventionally serves as the biomarker for hepatotoxicity risk. Thus, verification of model predictions at this time point is critical for establishing the clinical utility of the model. Figure 4.3.7 illustrates the accuracy of the model in predicting parent APAP concentrations for a wide range of doses at this time point, demonstrating reasonable-to-very good agreement over three orders of magnitude of APAP doses.

Although APAP serum concentration is useful as an indicator of hepatotoxicity risk, a more appropriate measure would be the concentration at the site of action. Thus, the PBPK model was employed to make liver-specific pharmacokinetic predictions, where parent APAP was used as a surrogate for the putative toxicant NAPQI. Figure 4.3.6 shows the ratio of liver-to-plasma APAP concentration, Φ, as a function of administered dose. Unlike a first-order kinetic model where Φ would remain constant at each time point, nonlinearities in the metabolism and

absorption mechanisms, coupled with non-equilibrium conditions embodied in the PBPK model led to a consistent increase in Φ as a function of dose, especially during the absorption phase. At relatively long times, absorption is no longer significant and dose-dependence is seen only at overdose conditions. Importantly, these results indicate that predictions of hepatotoxicity risk based on pharmacokinetic parameters derived under therapeutic dosing conditions can be misleading and may grossly underestimate the relative liver-to-plasma concentration ratio of APAP, especially at early time points.

4.13.2 Dose estimation studies

4.13.2.1 Optimal sampling time

The first dose estimation study concentrated on quantifying the effect of sampling time and choice of analytes on the accuracy of the APAP dose estimation. Figure 4.3.7 depicts results from this study and illustrates several significant findings. First, measuring both the parent APAP and APAP-G conjugate concentrations in a sample can significantly reduce the error for dose reconstruction compared to that for APAP concentration alone. One of the principal reasons for this is that following high, acute APAP doses, the APAP-S pathway becomes saturated and APAP metabolism shifts toward APAP-G production[141,148]. By including the APAP-G conjugate in the measurement, the total amount of the APAP dose accounted for increases from 7% (APAP alone) to 77% (APAP and APAP-G). Second, *for the purposes of dose estimation*, blood should be sampled at about four-and-a-half hours (APAP only) or five hours (APAP & APAP-G), which is somewhat later than that specified in the standard overdose assessment protocol. Third, if a second blood sample is taken after the initial sample at four hours, error is reduced, but this error does not depend on when the second measurement occurs. In addition, as in the single-sample case, measuring both APAP and APAP-G substantially decreases the error

in the reconstructed dose relative to that when only parent APAP is measured. Finally, knowledge of APAP-S concentration does not help inform dose reconstruction for overdose cases because, as noted earlier, the APAP-S metabolism pathway becomes saturated at large APAP doses, reducing the sensitivity of APAP-S concentration to administered dose.

4.13.2.2 Determining the administered dose

The second dose estimation study focused on dose estimation using data from both a well-controlled clinical environment and an emergency setting. As seen in Figure 4.3.8, the dose reconstruction method accurately predicted the administered APAP dose for the test and training set data from the clinical studies. However, for the data acquired in the emergency setting, the agreement between model predictions and self-reported dose range was not as consistent and was much poorer in several cases. This inconsistency in these instances is likely attributable to uncertainty in the patient's self-reported dose and the difficulty in establishing a reliable estimate of the time of APAP ingestion. In some instances, such a discrepancy could indicate a case where the patient intentionally reported an inaccurate dose or dosing time.

4.13.2.3 Implications for acetaminophen overdose treatment

As noted earlier, knowledge of the ingested APAP dose can have significant implications for managing a patient following an overdose. In this study, we demonstrated that an APAP dose can be estimated using the computational framework and a single serum APAP measurement. We also found that incorporating knowledge of the APAP-G concentration in that same blood sample would reduce the error in that prediction.

Current assessment and treatment plans for APAP overdose cases generally rely on a *generic* methodology involving the use of a clinical nomogram. By using the computational framework developed in this study, serum sample data, and the individual patient's

anthropometric and physiological information, it would be possible to quickly generate personalized serum and liver pharmacokinetic profiles and a dose estimate that should prove useful in developing an *individualized* overdose treatment and follow-up plan.

Finally, the PBPK model from this study is expected to provide a more accurate description of internal concentrations in the liver compared to previous models derived using therapeutic dosing data [162,163,194]. This information is essential in estimating further predictors of toxicity, such as levels of NAPQI and rates of glutathione depletion in the liver. Thus, if properly integrated, the present model has the potential to enhance the predictive capability of existing pharmacodynamic models used to predict and assess APAP toxicity [163,165,166,194].

It is worth noting that although the focus of this work has been on APAP overdoses, we expect that the general methodology and framework could be applied to overdoses for a broad range of drugs and toxicants, provided that relevant biomarkers of exposure can be measured and an appropriate PBPK model developed and evaluated.

CHAPTER 5

DEVELOPMENT OF ENVIRONMENTAL PUBLIC HEALTH INDICATORS FOR MONITORING CHLORPYRIFOS EXPOSURE

5.1 INTRODUCTION

Organophosphorus (OP) insecticides are among the most widely used synthetic chemicals used to control agriculture and domestic insect pests. About 70% of the insecticides in current use in the United States are OP insecticides, which amounts to a total of about 33 million kilograms of these chemicals applied each year [91]. OP insecticides phosphorylate numerous enzymes including a large number B-esterases whose primary function is to hydrolyze choline-based esters such as acetylcholinesterase (AChE) and butyrylcholinesterase (BuChE) [226]. These esterases are present throughout the body, with high abundances in the plasma, hematocrit, and brain. The primary mechanism of action of OP insecticide-induced toxicity is the inhibition of AChE by active oxon metabolites, resulting in the accumulation of acetylcholine neurotransmitter within the cholinergic synapses [227]. This accumulation of acetylcholine results in cholinergic toxicity due to continuous stimulation of cholinergic receptors throughout the central and peripheral nervous system. Symptoms of acute exposure to organophosphates or similar cholinesterase-inhibiting compounds may include headache, dizziness, numbness, tremor, nausea, sweating, blurred vision, respiratory depression, and slow heartbeat [228,229]. Very high doses may result in unconsciousness, incontinence, and convulsions or fatality [229].

Currently, the most sensitive effect observed in both animal and human studies from exposure to a variety of OP insecticides is the inhibition of cholinesterases [93,230,231]. With

This work was supported by the United States Environmental Protection Agency Science to Achieve Results (STAR) fellowship: FP – 91730301.

cholinergic biochemical changes as the primary endpoint of toxicity, point of departure (PoD) risk assessments have been conducted to determine benchmark doses corresponding to a given percentage of cholinesterase inhibition. For their most recent update, the 2006 OP insecticide cumulative risk assessment, The United States Environmental Protection Agency (USEPA) elected to use 10% AChE inhibition in the brain (BMD_{10AChE}) as the PoD response level, stating that "The 10% response level is health protective in that no functional or behavioral effects have been noted below this level in adult of juvenile animals" [92]. In addition to the formal 10% brain inhibition guideline set by USEPA, 20% red blood cell (RBC) AChE inhibition has also be considered as a reasonable effect level for protection against OP insecticide toxicity [93]. However, this same study concluded that RBC AChE inhibition is inherently variable, especially in larger doses, which requires a higher cutoff threshold for percent inhibition [93].

The conventional method for determining PoD benchmark doses involves developing the cholinesterase inhibition dose-response curve following OP exposure in rats. Specifically, using an appropriate pharmacodynamic relationship between known external dose and resulting cholinesterase inhibition, a benchmark dose, usually oral mg/kg/day, is estimated based on the designated biomarker of effect level, e.g., 10% AChE inhibition in the brain. While these estimates are extrapolated to humans to derive acceptable exposure thresholds, this PoD method ultimately relies on a benchmark doses corresponding to the dose-response in rodents.

Though 10% inhibition of brain AChE, a surrogate for cholinergic toxicity, serves as the current endpoint for protection against adverse health effects, there is mounting evidence that there may exist more sensitive adverse health endpoints. Multiple, meta-analyses concluded that low-dose, chronic exposure to OP insecticides in occupational settings adversely affects neurobehavioral performance in the vast majority of human subjects exposed [94,232]. In these

studies, neuropsychological testing uncovered impairments to a variety of neurobehavioral functions, such as memory (visual, working, and auditory), perception, and information processing [96,233–236]. Furthermore, these performance deficits occurred at OP insecticide exposure levels that did not produce overt signs of cholinergic toxicity, and biomonitoring indicated that cohort exposure fell below the BMD_{10AChE}. While these studies have developed a weight of evidence for cognitive deficits associated with long-term exposure to OP insecticides, there is significant uncertainty in the dose, frequency, and duration of exposure that give rise to the observed deficits [94]. This lack of exposure characterization has prohibited the creation of a source-to-outcome model that would link OP exposure to observed changes in cognition, ultimately allowing the development of a BMD based on this potentially more sensitive endpoint.

Despite a lack of detailed dosimetry data in humans, several studies have been conducted in the rat to investigate neurobehavioral dose-responses following known low-dose, chronic exposure to OP insecticides. These studies have employed a variety of neurobehavioral assessments during the course of the OP exposure, including the Morris water maze, which utilizes the delay-to-platform measurement to assess spatial memory deficits [97,100,237–241], the 5-choice serial reaction time test (5C-SRTT) to determine sustained attention deficits [98,99,242], and repeated acquisition tasks for assessing the ability to learn and maintain new information [243]. In all of these studies, dose-dependent neurobehavioral deficits were observed during or following low-dose, chronic exposure to OPs, with the majority of doses administered at levels below the PoD threshold for 10% AChE inhibition in the brain; moreover, in none of these cases were overt signs of cholinergic toxicity observed. The results from these studies

suggest that changes in cognition related to memory, attention, and learning, may serve as a more sensitive adverse health effect endpoint than that based on AChE inhibition.

To quantify the implications of this hypothesis and to better understand how a health-based endpoint can be used to estimate a benchmark dose, a methodology was developed, and computational framework implemented, that integrated a validated PBPK model, a new pharmacodynamic dose response model, and both pharmacokinetic and pharmacodynamic data in rats and humans. As illustrated in Figure 5.1, the workflow behind this framework is in contrast to the current PoD benchmark dose modeling procedures, which utilizes animal studies to make benchmark dose predictions based on a biochemical effect rather than an observable health outcome. In addition to the benchmark dose estimate, outputs from the analysis included the specification of threshold environmental public health indicators and benchmark external exposure conditions.

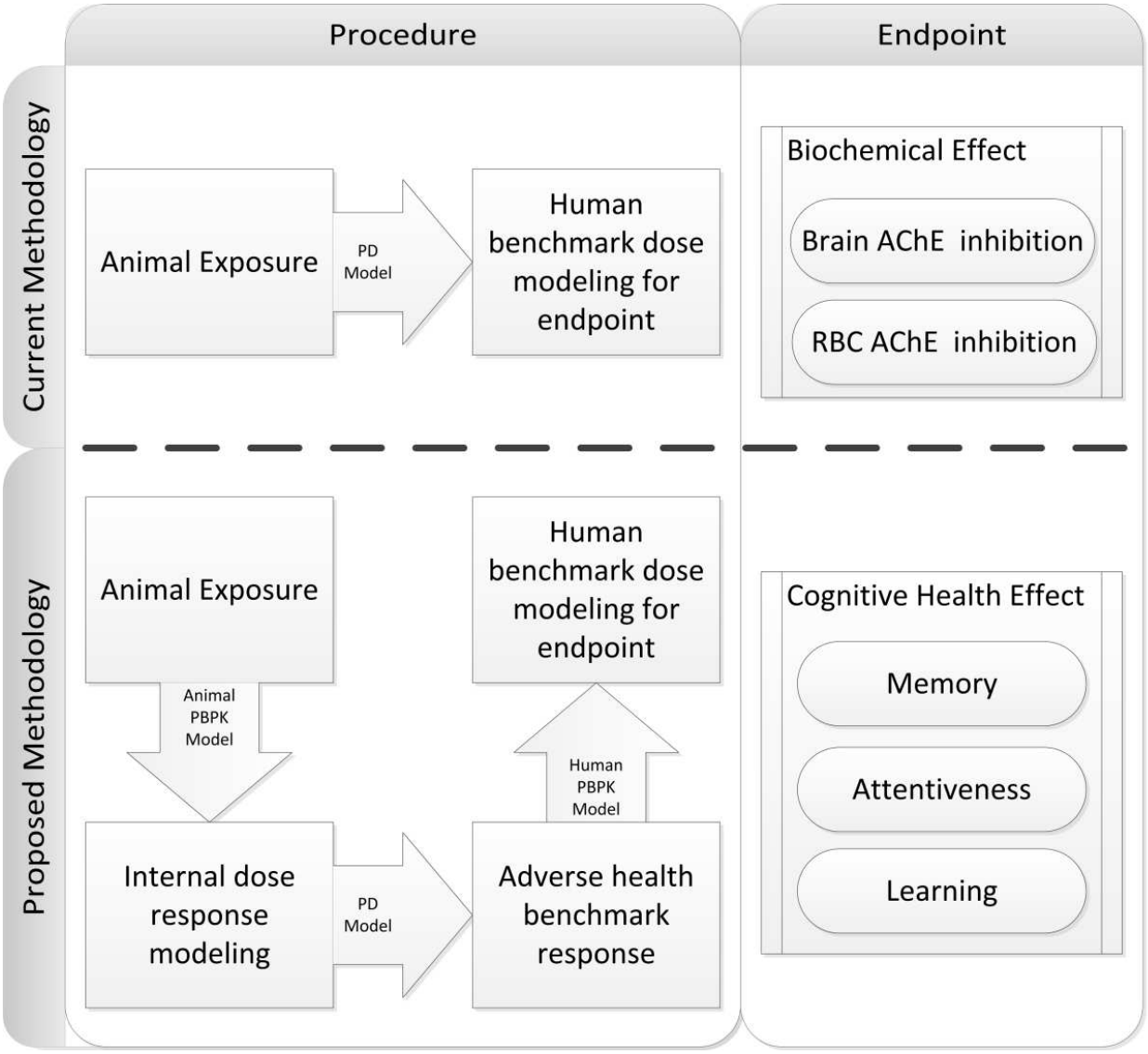

FIGURE 5.1. Overview of the procedure used to develop dose-response relationship for cognitive. The top row shows the current methodology for determining point-of-departure estimates of AChE inhibition while the bottom row illustrates the proposed methodology for using internal dose metrics to predict cognitive health endpoints.

5.2 MATERIALS AND METHODS

As shown in Figure 5.2, there were four fundamental analysis steps used in achieving the above outputs. In Step 1, dosing parameters corresponding to a large *exposure space* were used as input to a PBPK model for CPF. The term *exposure space* means exposures resulting from

variations in dose magnitude, duration, and frequency, as well as route of exposure, that could occur over a broad range of low-dose chronic exposure scenarios. This large series of model simulations produced a database of pharmacokinetic and pharmacodynamic results for each exposure condition. These results included measures such as CPF concentrations in the brain and plasma and various biomarkers of exposure, such as percent inhibition of RBC AChE and plasma BuChE. The PBPK/PD model used in this analysis was that developed by Poet and coworkers [48] and has been extensively verified and tested using both human and rat data over a broad dosing range. In Step 2, results from this exposure space database (ESD) corresponding to dosing conditions reported in a neurobehavioral study in rats [100] were used to develop a dose response model relating peak CPF concentrations in the brain to cognitive deficits in rats. In Step 3, data from the ESD were input to the dose response model to create a mathematical correlation between measurable biomarkers of exposure and cognitive effects. These biomarkers could serve as environmental public health indicators [244–246] (EPHIs) to relate readily measurable chemical species to the health status of a population with respect to CPF exposure. Finally, in Step 4 the exposure space was subdivided into risk categories based on the predicted resulting level of cognitive deficit.

The following sections give a more extensive description of each stage of the analysis. However, a more comprehensive description of model development is provided in the appendix of this chapter (§5.5).

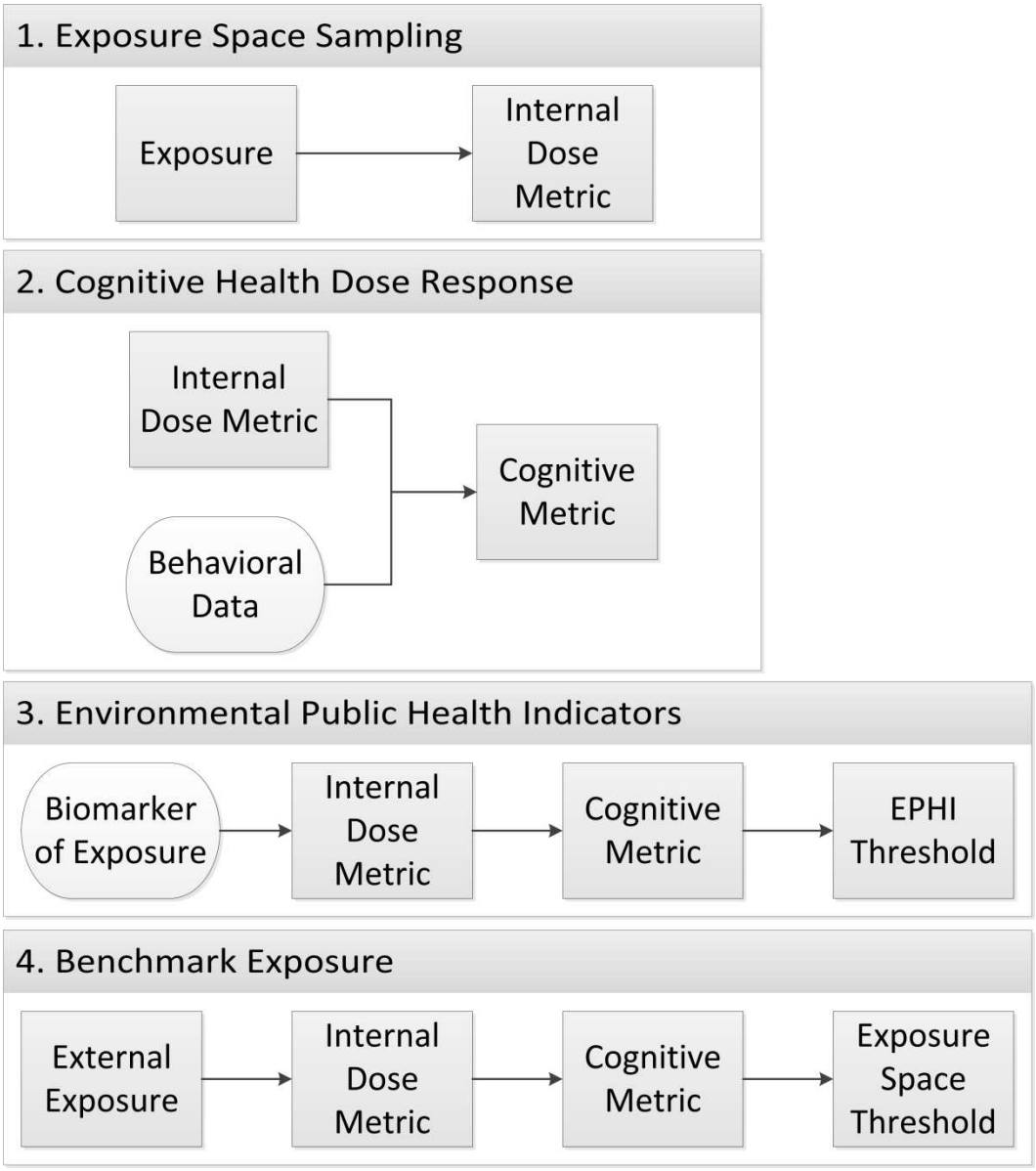

FIGURE 5.2. Methodology for determining EPHI and Exposure Space Thresholds. Rounded rectangles represent data measurable through biomonitoring or neurobehavioral studies while square rectangle represent values predicted from the proposed methodology.

5.2.1 Exposure space sampling

Four independent variables defined the exposure space: route of exposure, dose amount (D), exposure frequency (τ), duration of exposure (Δ). Exposure frequency represents the hours

between an exposure event, while the duration of exposure represents the amount of time over which the exposure event occurred. With the exception of the route of exposure, uniform parameter distributions were used for the parameters (Table 5.1), which were sampled using a Monte-Carlo (MC) algorithm and then input to the PBPK/PD model for a total of 10,000 sample draws. One month of exposure was simulated for each MC simulation with the final simulated day representing the steady-state window over which PK/PD endpoints were calculated.

TABLE 5.1. Sampled exposure space parameters. D is the administered dose, τ represents the time between dosing events, and Δ represents the duration of exposure.

Route of Exposure	D (units)	τ (hrs)	Δ (hrs)
Oral	$1x10^{-5}$ – 10 (mg/kg)	4 – 24	0.001 – τ
Dermal	$1x10^{-4}$ – 100 (mg/kg)	4 – 24	0.1 – τ
Inhalation	$1x10^{-5}$ – 10 (mg/m^3)	4 – 24	0.05 – τ

5.2.2 Cognitive health dose-response development

Though the exact source of the observed neurobehavioral deficits is currently under investigation, a consensus of the literature points to OP-induced changes in cognitive pathways resulting from localized oxidative stress and inflammation in the brain [229,232,247–250]. Because of this, peak CPF concentrations in the rat brain served as the internal-dose metric.

Using this metric, a cognitive dose-response relationship was developed through an E_{max} model [44,56] to describe the relationship between these predicted peak CPF concentrations, C_B, and the observed fractional cognitive deficit, E:

$$E = \left(\frac{C_B^{\gamma}}{E_{50} + C_B^{\gamma}} \right) \tag{5.1}$$

Here, the maximum effect level represents a 100% deficit in cognitive ability. Here, γ and E_{50} represent the Hill coefficient and peak CPF concentration to produce half of the effect, respectively. Parameters in this dose response model were estimated using data obtained using

the Morris water maze latency to platform tests [100], in which a delay in platform discovery relative to control indicates a cognitive deficit in spatial learning [251,252].

While additional forms for the above relationship were tested, as specified by benchmark dose methods outlined by the U.S. Environmental Protection Agency [253], the current formulation of the E_{max} model was deemed most appropriate due to the goodness of fit and relative model simplicity (two parameters). In addition, as a direct effect model, the current formulation best exemplified the currently hypothesized biological mechanism for OP insecticide-induced changes in neurobehavioral deficits.

Once the parameters for Eq. (5.1) were computed, the peak CPF concentration in the brain giving rise to a 15% cognitive deficit in spatial memory performance served as the PoD benchmark dose or BMD_{15CD}. The 15% threshold was chosen as it represented the smallest statistically significant departure in cognitive deficit from control. The lower limit benchmark dose ($BMDL_{15CD}$) was also computed using the lower 95% confidence interval from the peak CPF brain concentration.

Using the above dose-response model and results from the ESD, two outputs relevant to CPF biomonitoring were developed. The first involved predictions for the cognitive health endpoint using measurable biomarkers of exposure. As noted earlier, such biomarkers could be used as EPHIs in tracking the health status of a target population. In this study, three EPHIs were characterized for humans (peak CPF concentrations in the plasma, minimum red blood cell AChE inhibition, and minimum plasma BuChE inhibition), and one was analyzed for rats (peak CPF plasma concentration). Using the dose-response equation above, a predicted cognitive deficit was be determined from the peak brain CPF concentration predicted from the biomarkers

of effect. This approach led to the derivation of analytical relationships to predict the cognitive deficit from the specific EPHI.

The second output relevant for biomonitoring was a characterization of the external exposure conditions based on the resulting predicted peak CPF concentration and BMD_{15CD}/$BMDL_{15CD}$. Exposures giving rise to a predicted peak brain concentration below the BMD_{15CD} were deemed safe while exposures resulting in peak brain CPF concentrations above the $BMDL_{15CD}$ were characterized as hazardous. In addition, temporal parameters such as dosing frequency and fraction of day exposed for a chronic dose were utilized in deriving this benchmark exposure assessment.

Further details related to the governing equations and model development can be found in the appendix.

5.2.3 Software and computing platform

The CPF PBPK/PD model simulations and Monte-Carlo sampling were conducted using MCSim (v.5.6) [77]. Parameter estimation of the E_{max} model was performed using lsqfit (v.7.1) [254]. Determining the model structure for correlating biomarkers of exposure to peak CPF concentrations in the brain was carried out in Eureqa [255].

5.3 RESULTS

5.3.1 Internal-dose prediction from known exposure

Using the methodology described in §5.2.1, peak CPF concentrations in the brain were estimated (Table 5.2) and were subsequently used in the determination of the dose-response model with reported cognitive deficit as the endpoint.

TABLE 5.2. Predicted peak brain CPF concentrations

Dose (mg/kg)	Peak brain CPF (μM)
0	0
1	9.13×10^{-4}
5	4.62×10^{-3}
10	1.02×10^{-2}

5.3.2 Dose-response modeling

5.3.2.1 Dose-response curve

Using the results in Table 5.2, a non-linear least squares approach was utilized to determine the unknown parameters in Eq. (5.1), resulting in mean (CV) values of EC_{50}= 0.035 (0.47) and γ=0.31 (0.18). Using these parameters, the fit of data to the model equation, and resulting uncertainty envelope, is shown in Figure 5.3.

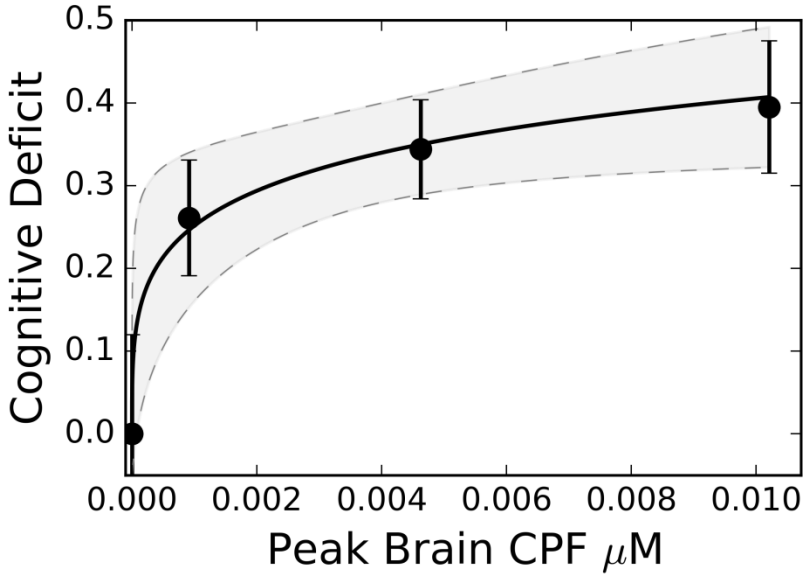

FIGURE 5.3. Dose-response curve for spatial memory fractional deficit. Solid and dashed lines represent the mean and 95% prediction intervals respectively. Circles represent reported fractional cognitive deficit [100]. Peak CPF concentrations for these data are the values predicted from the PBPK/PD model based on the reported exposure.

5.3.2.2 Benchmark dose calculation

Using the calibrated E_{max} model, benchmark internal doses were determined for a 15% deficit in spatial memory function. Table 5.3 lists these BMD_{15CD} and $BMDL_{15CD}$ for a spatial memory deficit using peak CPF concentrations in the brain as the internal dose metric. Also in this table are the current BMD/BMDL for 10% brain AChE inhibition and 20% RBC AChE Inhibition [93].

TABLE 5.3. Comparison of benchmark doses for various endpoints.

Endpoint	**Peak Brain CPF Concentration**	
	BMD (μM)	**BMDL (μM)**
15% Cognitive Deficit	$1.23x10^{-4}$	$8.82\ x10^{-6}$
20% RBC AChE Inhibition	$1.91\ x10^{-4}$	$1.73\ x10^{-4}$
10% Brain AChE Inhibition	$6.11\ x10^{-4}$	$4.83\ x10^{-4}$

5.3.3 Biomarkers of exposure as EPHIs

Environmental public health indicators were derived by correlating measurable biomarkers of exposure to predicted cognitive deficits. This correlation took the form of a polynomial describing fractional cognitive deficit as a function of peak CPF plasma concentrations in the rat. Coefficients [mean (CV] of this correlation were as follows α_1 = 0.55 (0.24), α_2 = 0.087 (0.34), α_3 = 4.12E-3 (0.45), α_4 = 5.91E-6 (0.36). A full description of the polynomial can be found in the appendix of this chapter (§5.5). The resulting curves are presented in Figure 5.4 where mean and 95% prediction intervals are presented, along with reported spatial memory deficits and measured peak CPF plasma concentrations from an *in vivo* experiment [97].

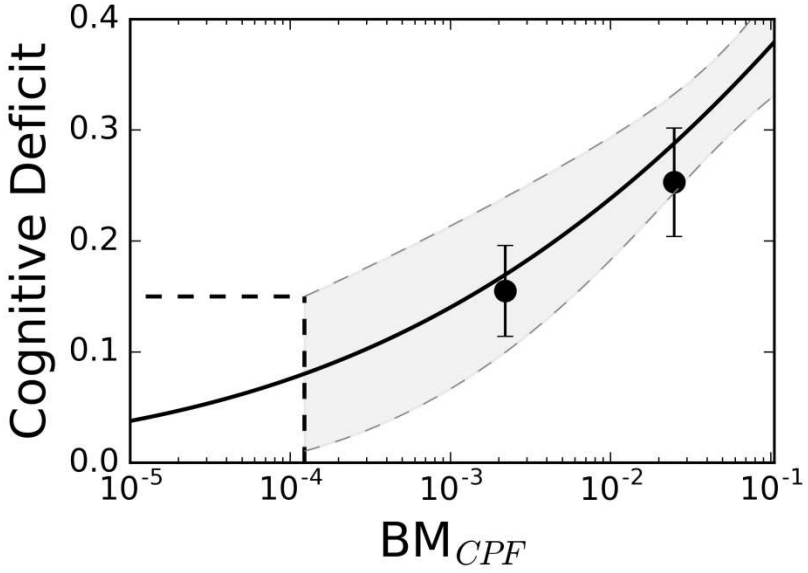

FIGURE 5.4. Predictions of cognitive deficit for the rat. Dashed lines represent 95% prediction intervals, solid circles (●) represent data from Terry et al. [97]. Horizontal and vertical dashed lines demonstrate the threshold biomarker of exposure for a 15% cognitive deficit.

This same correlation method was then applied to humans using three different biomarkers of exposure. Parameter values for the governing correlations in this case are presented in Table 5.4 and resulting predictions based on levels of biomarkers of exposure are presented in Figure 5.5. Using each BM_i curve developed in Figure 5.5, threshold biomarker of exposure levels were determined using the upper 95% confidence interval ensuring that health indicators provided the maximum protection for a given population. After transforming each BM_{AChE} and BM_{BuChE} back to percent enzyme available, the following exposure thresholds were determined: 1.03E-4 μM for peak CPF plasma concentrations, 99% available RBC AChE, and 90% available plasma BuChE.

TABLE 5.4. Model parameter values for each biomarker of exposure. Values for each α are presented as mean (CV).

Biomarker	α_1	α_2	α_3	α_4
BM_{CPF}	0.68 (0.28)	0.12 (0.32)	5.8×10^{-3} (0.4)	-4.81×10^{-6} (0.33)
BM_{AChE}	0.3 (0.26)	0.031 (0.15)	4.41×10^{-4} (0.57)	1.52×10^{-6} (0.32)
BM_{BuChE}	0.14 (0.31)	0.022 (0.15)	2.61×10^{-4} (0.41)	1.01×10^{-5} (0.35)

Results from Farahat et al. [235] were utilized to test the prediction of cognitive deficits from measurable biomarkers of exposure. This study involved long-term occupational exposure in humans and measured a multitude of neurobehavioral performance deficits. One of these tests was the Benton visual retention test (BVRT) which is a human-equivalent test for assessing spatial memory deficits [256]. While this neurophysiological test is not identical to the Morris water maze test in rats, it tests the same parts of the brain, specifically hippocampal sub-regions, which are responsible for processing information related to spatial memory [257]. In this study, the biomarker of exposure used to assess CPF exposure was red blood cell AChE inhibiton and investigators reported an approximate 17% deficit in the BVRT for exposed groups compared to control. Corresponding RBC AChE was determined to be about 80% of activity compared to control. Using the measured RBC AChE activity as the biomarker of exposure, reported cognitive deficits are compared to predictions in Figure 5.5. Because 80% activity of RBC AChE was reported, the biomarker of exposure used for cognitive prediction was 0.25 (see §5.5).

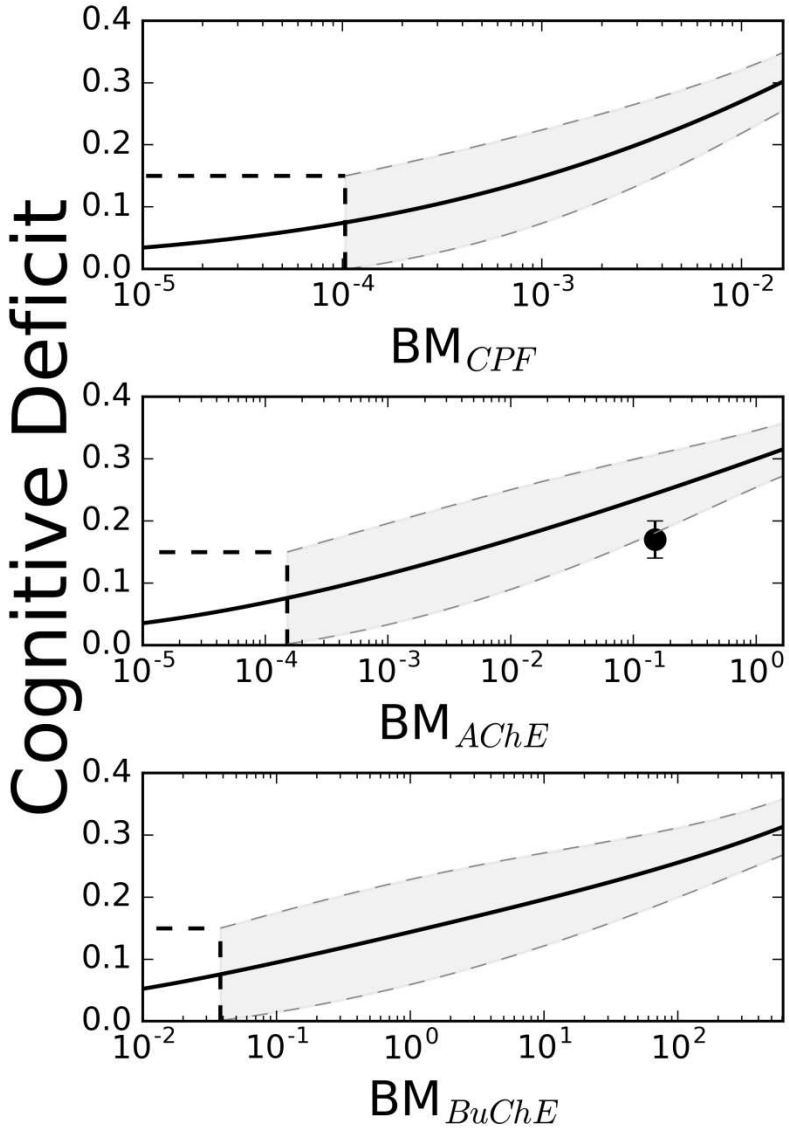

FIGURE 5.5. Predictions of cognitive deficit for humans using peak CPF concentrations in the plasma, minimum red blood cell AChE inhibition, and minimum plasma BuChE inhibition as the biomarkers of exposure. Dahsed lines represent 95% prediction intervals and the solid circle (●) represents measured data from Farahat et al. [235].

5.3.4 Exposure space

Using the effective internal dose metric calculated from the dose-response modeling in the rat, the exposure space resulting in concentrations below the BMD_{15CD} and $BMDL_{15CD}$ was determined. Figure 5.6 depicts this space for oral, dermal, and inhalation routes of exposure for the rat where "total absorbed dose" represents the total amount of CPF administered over the duration of exposure.

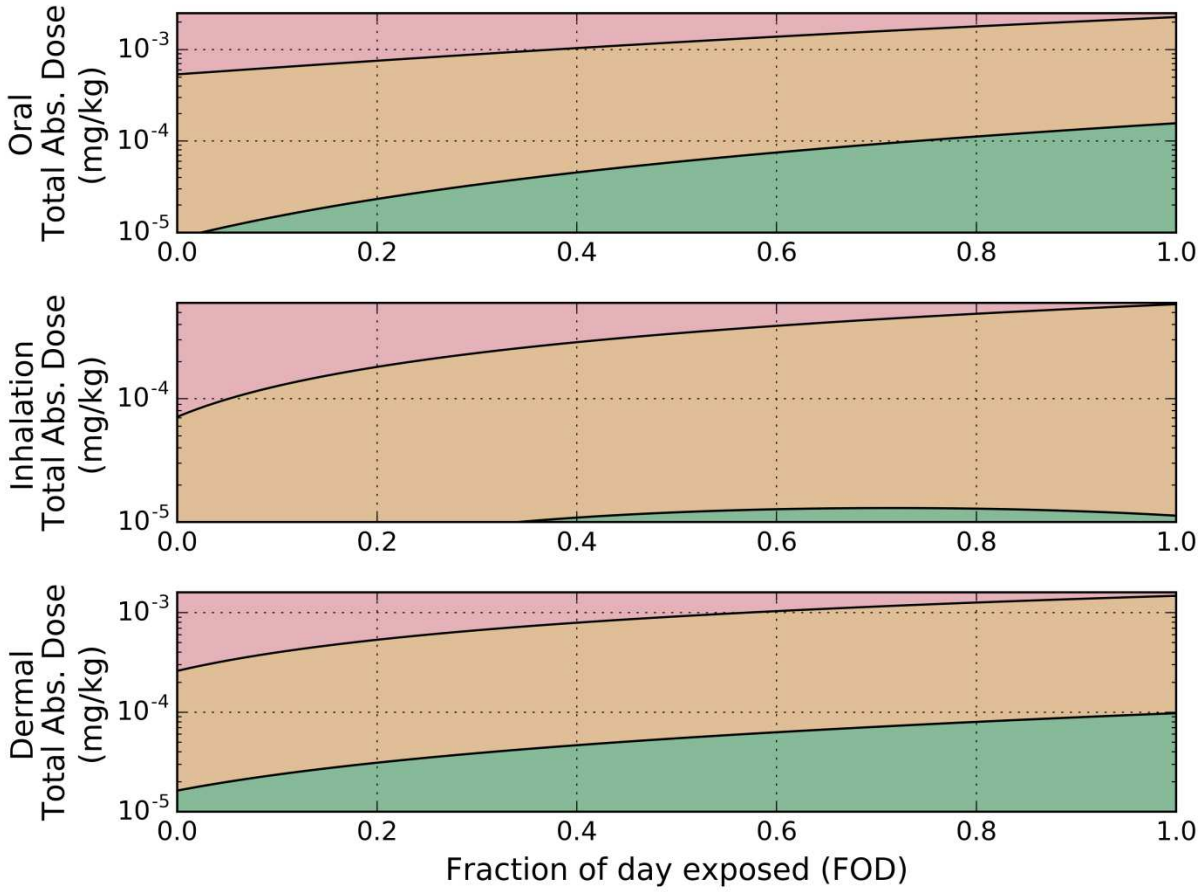

FIGURE 5.6. External exposure space for rats. Red, yellow, and green shading indicate exposure scenarios that fall above the BMD_{15CD}, between the BMD_{15CD} and $BMDL_{15CD}$, and below the $BMDL_{15CD}$ respectively.

From these results, the rat-equivalent oral exposure resulting in peak brain CPF concentrations equal to the BMD_{15CD} and $BMDL_{15CD}$ was determined and fit using a second order polynomial (see §5.5), where relevant model parameters for the rat are presented in Table 5.5.

As an example of the application of this methodology, for a once daily, oral gavage exposure, $\Delta = 0.083$ (five-minute exposure) and $\tau = 24$ (once daily exposure). Therefore, the fraction of day exposed for this exposure scenario is $FOD = 0.0035$ hrs and the threshold repeated oral exposure based on the BMD_{15CD} is 0.148 mg/kg/day with a $BMDL_{15CD}$ of 0.0024 mg/kg/day.

TABLE 5.5. External exposure space parameters for model fit for the simulated exposure space

Derived BMD	Route of Exposure	Species	β_1	β_2	β_3
BMD_{15CD}	Oral	Rat	0.148	0.253	0.227
		Human	0.00848	0.0106	0.00787
	Inhalation	Rat	0.779	6.052	-0.423
		Human	1.334	3.386	-2.151
	Dermal	Rat	68.564	372.216	-47.535
		Human	0.288	1.619	-0.249
$BMDL_{15CD}$	Oral	Rat	0.00241	0.0148	0.0262
		Human	5.807×10^{-4}	3.325×10^{-5}	1.105×10^{-3}
	Inhalation	Rat	0.022	0.334	-0.232
		Human	0.0694	0.133	-0.059
	Dermal	Rat	4.299	18.99	2.718
		Human	0.069	0.133	-0.059

The analogous analysis was then conducted using results for humans, and in this case, exposures resulting in the BMD_{15CD} and $BMDL_{15CD}$ are displayed in Figure 5.7.

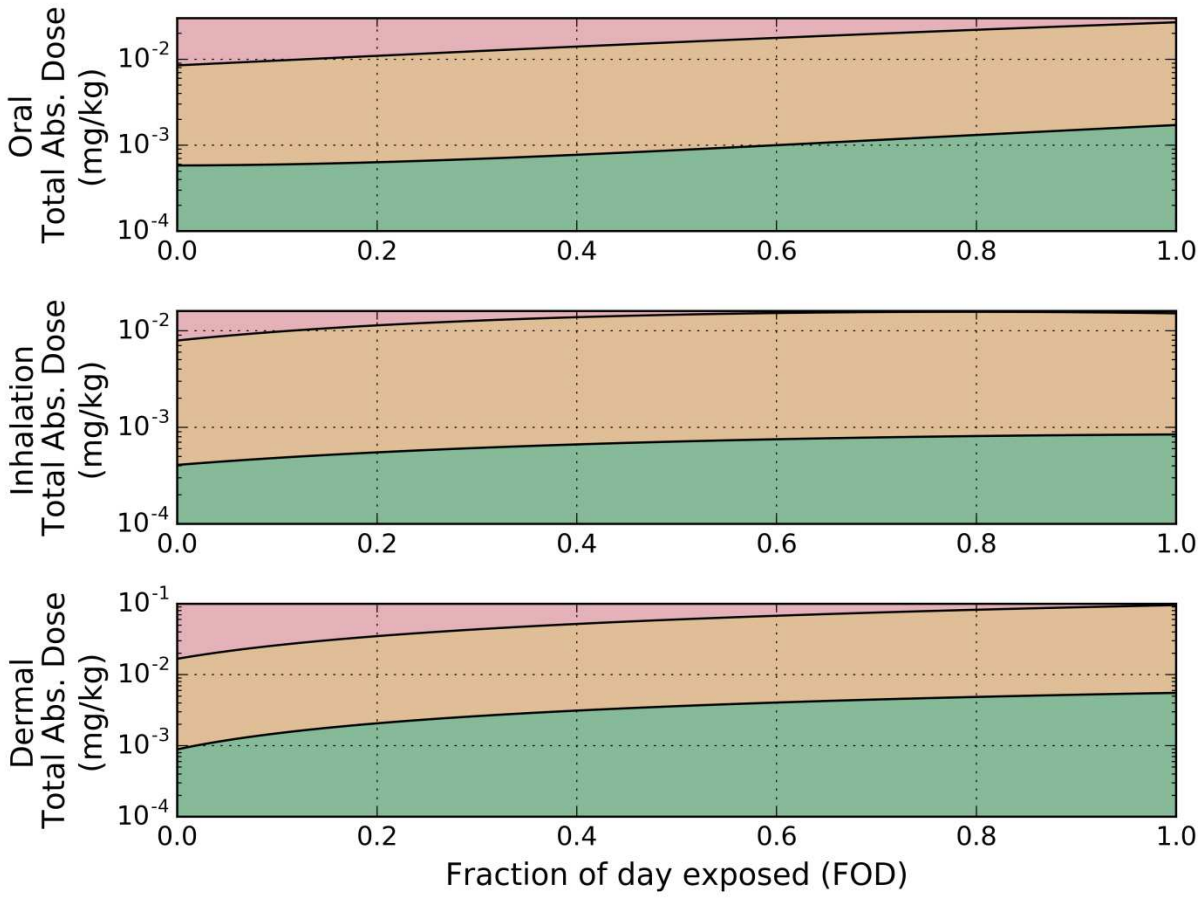

FIGURE 5.7. External exposure space for humans. Red, yellow, and green shading indicate exposure scenarios that fall above the BMD_{15CD}, between the BMD_{15CD} and $BMDL_{15CD}$ and below the $BMDL_{15CD}$ respectively.

As with the analysis for the rodent data, the human equivalent oral exposure resulting in peak brain CPF concentrations equal to the BMD_{15CD} and $BMDL_{15CD}$ was determined and fit using a second order polynomial with respect to the fraction of day exposed (see §5.5) and the best-fit model parameters presented in Table 5.5. In this case of human exposure, assuming a once daily, oral exposure, $FOD = 0.0035$, the benchmark exposure for this scenario is 0.0085 mg/kg/day.

5.4 DISCUSSION

5.4.1 Methodology

The current study provided a method for not only determining a point-of-departure for cognitive deficits through benchmark dose modeling, but also utilization of measurable biomarkers of exposure to develop public health indicators for monitoring this cognitive health outcome. The use of a neurobehavioral endpoint offer several advantages to that based on cholinesterase inhibition. First, the neurobehavioral endpoint represents an overt change in health of the individual, whereas the inhibition of cholinesterase merely represents a biochemical change that may or may not represent an adverse health effect. Second, a variety of neurobehavioral endpoints can be used, depending on the application and availability of data. For example, coordination and motor deficits could be the metric of interest instead of spatial memory as was illustrated here.

Utilizing the dose-response for a given cognitive deficit allowed for the construction of environmental public health indicators from measurable biomarkers of exposure, which serve as a tool for determining a source-to-outcome continuum for monitoring health outcomes from exposure to CPF to neurobehavioral changes for a given cohort. In specifying a threshold for the given cognitive deficit, e.g. 15% deficit in spatial memory, biomonitoring data from a population can be used to determine in the given cohort is protected.

Finally, external exposure benchmarks were derived based on the internal dose BMD_{15CD} and $BMDL_{15CD}$. Specifically, the predicted BMD_{15CD} for repeated oral exposure was determined to be 0.0085 mg/kg/day: similar in magnitude to the exposure estimated in the farm family exposure study [258], which estimated a CPF dose of 0.0021 mg/kg/day for applicators. Thus,

the new BMDs, which are significantly lower than those recommended by the USEPA, are highly relevant, and would be more protective, under many realistic exposure conditions.

5.4.2 Novel features and advantages of the present methodology

By utilizing a well-validated PBPK/PD model coupled with appropriate pharmacodynamic data, exposures resulting in neurobehavioral changes were linked using internal concentrations at the proposed site of action, rather than using external exposure metrics. This is meaningful because the amount of organophosphate that reaches the brain will differ based on the route, frequency, and duration of exposure. In addition, the methodology developed for determining EPHIs is not specific to the endpoint illustrated here; it is easily applied to a variety of studies where a dose-response neurobehavioral change is observed. For example, although not detailed in this work, this method was applied to the CPF dose-response data reported in Cohn et al. [243].

In addition, the current methodology allows for the determination of a meaningful exposure space to quantify how exposure to CPF compares to the target endpoint. Many of the current point-of-departure benchmark doses are determined for a single route of exposure and assume the same dosing frequencies, i.e. an oral dose administered repeatedly once per day. Figure 5.6 and Figure 5.7 illustrate how exposure parameters are collapsed into a two-dimensional space for each route of exposure. Therefore, exposure thresholds for oral, dermal, and inhalation routes of exposure can be determined based on the fraction of day exposed.

5.4.3 Limitations and deficiencies of the present EPHI approach

The current method for developing EPHIs and determining a safe exposure space suffers from several limitations. First, behavioral endpoints in the rats, such as spatial memory deficits from the Morris water maze and repeated acquisition results, are not adequately correlated to

cognitive deficits in humans. Results from the Morris water maze and the corresponding changes due to exposure are indicative of a hippocampal synaptic plasticity and receptor function [252]. Though the Benton visual retention test in humans is also correlated strongly with changes in the denate gyrus hippocampal subregion [257], results from the Morris water maze in the rat have not been correlated to those from this related test. Second, the mechanism of action of CPF on cognitive deficits is unknown. Hypotheses from studies reviewed in §5.1 suggest a non-cholinergic affinity for the OP insecticide in various parts of the brain. Differences in OP-induced effects between cognitive tests demonstrate the OP's affinity to different regions of the brain. However, further *in vivo* and *in vitro* tests will further elucidate this mechanism of action and be used to update the current dose-response model.

5.4.4 Future directions

Using the present method detailed herein as a foundation, testing of additional sensitive neurobehavioral endpoints can be undertaken. Because CPF concentrations in the brain will have localized effects in different regions, the degree of damage to one cognitive pathway may be different from that to a different pathway. Therefore, establishing EPHI thresholds for different types of learning and memory will allow for a better protection of exposed populations. In addition, mechanistically-based pharmacodynamic models for CPF induced receptor inhibition will enable pathway-specific predictions to be made.

In order to characterize CPF effect on additional cognitive pathways, animal studies must be completed using explicit exposure conditions with doses much lower than those current used to elicit cholinergic responses. In addition, the route of exposure chosen for these studies must be incorporated into the PBPK/PD model for the determination of internal dose metrics, such as peak CPF concentrations in the brain. Using the PBPK/PD model, internal pharmacokinetic

endpoints, such as peak CPF brain concentrations, can be determined simultaneously with predicted biomarkers of exposure, and the dose-response curve for the desired cognitive deficit can be determined. Finally, the measurement of relevant biomarkers of exposure and corresponding neuropsychological endpoints in the cohort of interest is critical. This work demonstrates that by measuring peak CPF concentrations in the plasma, minimum RBC AChE inhibition, or minimum plasma BuChE inhibition, predictions related to relevant cognitive deficits can be made under a variety of exposure conditions.

5.5 Appendix: Model Development

5.5.1 Environmental public health indicators

Using the dose-response curve derived for a spatial memory deficit, possible biomarkers of exposure from the sampled exposure space were correlated to peak CPF concentrations in the brain. This correlation allowed for the determination of the cognitive deficit metric as a function of a measurable biomarker, as opposed to unmeasurable brain concentrations. Predicted peak CPF brain concentrations for each sampled exposure scenario were inputs in predicting a corresponding cognitive deficit using Eq. (5.1). Biomarkers of exposure in each case were fit to the following equation for the selected cognitive endpoint, *CM*:

$$CM = \alpha_1 + \alpha_2\left[\log\left(BM_i\right)\right] + \alpha_3\left[\log\left(BM_i\right)\right]^2 + \alpha_4\left[\log\left(BM_i\right)\right]^4 , \tag{5.2}$$

where BM_i represents the measured biomarker of exposure, and α_i are the parameters to be fit. Biomarkers of exposure can be both measurable concentrations and percent enzyme inhibitions. If red blood cell AChE or plasma BuChE served as the biomarker of exposure, BM_i was transformed according to: $BM_i = \left(100 - \psi\right)/\psi$ where ψ is the percent of enzyme available for reaction; however, if peak plasma CPF was chosen, BM_i was simply the measured CPF concentration. In terms of nomenclature, predicted biomarkers of exposure were denoted by

BM_{CPF} for peak plasma CPF concentrations, BM_{AChE} for transformed RBC AChE inhibition, and BM_{BuChE} for transformed plasma BuChE inhibition. The functional form for Eq. (5.2) was chosen as it adequately predicted the fractional cognitive deficit using all three biomarkers of exposure and minimal degrees of freedom. Using Eq. (5.2), EPHI thresholds were determined for each biomarker of exposure based on the BMD_{15CD}. With the parameterization of Eq. (5.2), cognitive deficit predictions were made in both the rat and human using studies where both reported biomarkers of exposure and neurobehavioral deficits were reported [97,235]. In these studies, the route of exposure was either unknown or utilized a route of exposure not parametrized in the original PBPK/PD model.

5.5.2 Benchmark exposure

5.5.2.1 Exposure space mapping

To calculate the rat-equivalent and human-equivalent external exposure threshold dosing scenarios, the exposure space from the initial Monte Carlo draw on the PBPK/PD model was used to map external exposure to the CPF brain concentrations for the two species. This mapping allowed for a given external dosing scenario to be compared directly to the BMD_{15} and $BMDL_{15}$ derived earlier. The independent exposure parameters (duration, periodicity, and dose) were transformed to allow for a two-dimensional representation of Total Absorbed Dose (*TAD*) vs. Fraction of Day (*FOD*) exposed, with *FOD* defined as

$$FOD = \frac{\Delta}{\tau}, \tag{5.3}$$

where Δ is the duration of exposure, τ is the time between exposure events. Therefore, *FOD* ranged from 0 to 1 and represented the fraction of the day over which the total absorbed dose was administered. *TAD* denoted the cummulative amount of CPF administered to the organism over the duration period. The *TDA* metric (mg/kg) is characteristic of the total amount of external

exposure applied to the organism over the course of a single day. Based on these two exposure parameters, predicted peak CPF brain concentrations from the PBPK/PD model were used to classify the total dose and fraction of day exposed.

5.5.2.2 Benchmark CPF exposure

Peak CPF concentrations were determined for these two independent exposure parameters. Exposure cutoffs, based on the BMD_{15} and $BMDL_{15}$, were determined as a function of *FOD* using a second order polynomial:

$$TAD_r = \beta_1 + \beta_2 (FOD) + \beta_3 (FOD)^2 \quad (5.4)$$

where TAD_r is the calculated total absorbed dose for a given route of exposure, *FOD* is the fraction of day exposed, and β_i are the parameters for fitting. Therefore, for a given *FOD* and route of exposure, the total external dose can be determined based on either the BMD_{15} or $BMDL_{15}$. A second order polynomial was chosen for the interpolation as it was the polynomial with the fewest degrees of freedom allowing for the entire space of *FOD* to be predicted.

CHAPTER 6

MODELING TOXICODYNAMIC EFFECTS OF TRICHLOROETHYLENE ON LIVER IN THE MOUSE MODEL OF AUTOIMMUNE HEPATITIS

6.1 INTRODUCTION

Trichloroethylene (TCE) is a chlorinated hydrocarbon that has been used as a degreasing agent since the 1920s. Because of inappropriate disposal over the years TCE is now a common pollutant at Superfund toxic waste sites and at many industry and government facilities. It is found in soil and surface water as a result of direct discharges and in groundwater due to leaching from disposal operations. As noted by a recent National Research Council report, evidence on human health hazards from TCE exposure, either occupational or environmental, has strengthened in recent years [259]. One of the predominant non-cancer outcomes associated with TCE exposure in humans is immunotoxicity, most notably the development of hypersensitivity responses including autoimmune scleroderma and autoimmune liver diseases [101–104,260–264]. TCE is still widely used in Asia, where it has become a serious work-related health concern due to the induction of dermal and systemic hypersensitivity diseases often accompanied by non-viral, immune-mediated hepatitis [105].

Using a mouse model, Gilbert and coworkers in this study [42], along with others, have found that long-term exposure to TCE in drinking water at concentrations lower than sanctioned occupational exposure levels generated a T cell-mediated liver disease commensurate with human idiopathic autoimmune hepatitis (AIH) [20,265,266]. This TCE-induced liver inflammation was not usually accompanied by markers of acute liver injury such as increased

This work was performed jointly with Dr. Kathleen Gilbert's lab in the Department of Microbiology and Immunology at the University of Arkansas for Medical Sciences where the in vivo mouse experiments were undertaken. The full list of co-authors is available at [37].

blood levels of alanine transaminase or liver fibrosis, but was associated with the development of antibodies specific for liver microsomal proteins similar to those in patients with type 2 AIH.

The development of toxicant-induced immune pathology such as the autoimmune hepatitis caused by TCE exposure is almost certainly a complex multifactorial process. Developing conceptual models can be a way to delineate and quantify the contribution of different toxicant-induced alterations to the actual pathology. As a first step in this direction a model was developed here to describe a specific part of the process, namely IL-6-mediated liver events. IL-6 is one of the most important regulators of hepatic inflammation. The pathogenesis of AIH requires circumvention of the well-known propensity of the liver to induce T cell tolerance [267]. Pre-existing inflammation in the liver may subvert its tolerogenicity and help sustain an immune response by entering T cells [268]. The ability of toxicant exposure to generate such inflammation depends on opposing forces of tissue injury and tissue repair. Distress signals triggered during initiation of toxicant-induced liver injury (e.g. lipid peroxidation, reactive intermediate formation) can promote inflammation. However, they also stimulate protective (anti-apoptotic) and regenerative (cell division) mechanisms in the liver. One of the mechanisms that determine whether toxicant exposure ultimately leads to tissue repair or to injury-induced inflammation is regulated by IL-6.

Treatments to prevent or reverse immunological liver injury in mouse models have been associated with an increase in liver expression of IL-6 [269]. Disruption of IL-6, or its receptors IL-6R or Gp130, has been shown to promote liver inflammation and/or mortality following partial hepatectomy [270], ethanol-induced hepatic steatosis [271], carbon tetrachloride-induced liver necrosis [272] and obesity-associated insulin resistance [273]. Thus, IL-6 appears to prevent immunological liver injury. In addition to its documented ability to promote liver regeneration

and/or protection in the face of damage or trauma IL-6 also appears to be required for normal liver maintenance. Liver weight and total DNA and protein contents were decreased 26-28% in older (5-10month-old) female IL-6-deficient mice as compared to age-matched wild-type controls [274]. This suggests that IL-6 is needed for normal hepatocyte turnover, and that over time a loss of this cytokine is detrimental to liver function.

In an attempt to define why TCE-induced autoimmunity targets the liver, Gilbert and coworkers exposed mice to a single dose of TCE for 4, 10, 16, 22, 28, 34 or 40 weeks in the current study to determine time-dependent alterations in IL-6 as well as other pro-inflammatory mediators. This was complemented by a second study that examined the dose-dependent effects of TCE on these mediators at a single time point [42]. The development of autoimmune hepatitis in this mouse model of TCE exposure involved alterations in both the liver and the immune system. This multi-factorial process mimicked the complicated etiologies of human autoimmune diseases.

Developing conceptual models can be a way to delineate and quantify the contribution of different disease-induced alterations to actual pathology. As a first step in this direction, the results obtained through experimental TCE exposure in mouse drinking water were used to develop a computational toxicodynamic model to describe the element of the TCE-induced disease process revealed in the *in vivo* experiments, namely the effect of TCE on IL-6-mediated liver events. Taken together, the results suggest that later-occurring TCE-induced liver damage was due to an early decrease in IL-6-mediated hepatoprotection rather than an increase in pro-inflammatory events.

6.2 METHODS

6.2.1 Experimental mouse treatment

Dr. Gilbert's lab at the University of Arkansas for Medical Sciences completed the *in vivo* mouse treatment studies. In their study, eight week-old female MRL +/+ mice were exposed to TCE through drinking water. In one experiment, the mice (12 mice/group) received either 0, 0.02, 0.1, or 0.5 mg/ml TCE in their drinking water for 12 weeks. In a second experiment, the mice (8-9 mice/group) received 0 or 0.5 mg/ml TCE in their drinking water for 4, 10, 16, 22, 28, 34, or 40 weeks. The mice were studied weekly and water consumption was monitored. When the mice were euthanized at the different time points, adherent macrophages, isolated from pooled peritoneal exudates from 2 to 3 mice (n = 3-4/treatment group), were incubated for 20 h in the presence or absence of lipopolysaccharide (LPS) to stimulate cytokine production from the macrophage. Liver tissue harvested at the time of euthanasian was stained with H&E and examined for liver pathology. Liver and sections were examined microscopically and scored in a blinded manner by a veterinary pathologist for the severity of inflammation and fibrosis based on a four point scale (1-4), ranging from no change to severe, respectively as described in Gilbert et al. [20]. Finally, the macrophage culture supernatants were examined to quantitate expression of IL-1β, IL-6, and TNF-α.

6.2.2 Mechanistic toxicodynamic model

The effects of IL-6 signaling on liver events in TCE-treated mice were modeled to link changes in TCE mediated IL-6 signaling outcomes to the observed pathology following low-dose chronic exposure to TCE. The objective in developing a mathematical model for chronic, low dose exposure to TCE was to provide a means to quantitatively describe the role of IL-6 as a maintenance mechanism and predict downstream effects, such as changes in pathology, due to

modifications of this IL-6 repair pathway. To this end, a time-dependent mathematical description of the health state of discrete volumes of liver ("liver units") and the IL-6 and TCE-dependent transition between these health states was developed. Using *in* vivo results reported in this study, this toxicodynamic model will create a link between TCE exposure and the resulting histopathology. While not measurable *in vivo*, the state and number density of individual liver units serve as an intermediate measure to quantify the relationship between impaired cytokine signaling and the resulting autoimmune hepatitis.

6.2.2.1 Liver unit health model

TABLE 6.1. Description of LU states

LU State	**Distinguishing Characteristics**	**Relevant Pathology Score (PS)**
Healthy (H)	Normal liver function, homeostatic levels of IL-6 and IL-6r	1
Compromised (C)	Intermediate state, events initiate inflammatory pathways which are normally countered by IL-6 signaling.	2
Inflamed (I)	Contains markers for the early stages of auto-immune hepatitis, including inflammation and lymphoplasmacytic portal infiltration	4

For the purposes of mathematical modeling, the characteristics of the liver units (LUs) were as follows: the entire liver comprises LUs, each of which is of equal volume; an LU is relatively small in volume compared to that of the entire liver, but consists of a large enough number of cells to be represented as a continuum; each LU exists in one of three health states: healthy (H), compromised (C), and inflamed (I), and is homogeneous with respect to its properties and health state; and the health state of the entire liver may be estimated through a number-weighted average of the health states of the constituent LUs. Table 6.1 lists the characteristics and assumptions for each mathematical state.

The resulting transition between health states is described by

$$H \underset{k_{REP,H-C}}{\overset{k_{DAM,H-C}}{\rightleftharpoons}} C \underset{k_{REP,C-I}}{\overset{k_{DAM,C-I}}{\rightleftharpoons}} I \tag{6.5}$$

where the k's represent transition rates, the subscripts *DAM* and *REP* refer to damage- and repair-associated phenomena, respectively, and the subscripts H-C and C-I refer to their respective transition pathways.

The corresponding system of differential equations governing the time-dependent fraction of LUs in each state may be written as

$$\begin{aligned}
\frac{d[H]}{dt} &= -k_{DAM,H-C}[H] + k_{REP,H-C}[C] \\
\frac{d[C]}{dt} &= k_{DAM,H-C}[H] + k_{REP,C-I}[I] - \left(k_{REP,H-C} + k_{DAM,C-I}\right)[C] \\
\frac{d[I]}{dt} &= -k_{REP,C-I}[I] + k_{DAM,C-I}[C]
\end{aligned} \tag{6.6}$$

Here, t is time and [H], [C], and [I] are the fractions of LUs in the healthy, compromised, and inflamed states, respectively. It is assumed that initially (t=0), [H]=1 and [C]=[I]=0.

To complete the mathematical description of this system, four major assumptions were made:

1. LUs normally exist in a state of IL-6-mediated hepatocyte turnover and protection.
2. Events such as TCE exposure can initiate inflammatory processes and move the LUs into the "C" state. However, protective mechanisms mediated by IL-6 normally restore the LUs from the "C" to the "H" state. The rates of repair, $k_{REP,H-C}$ and $k_{REP,C-I}$, are dependent on the fraction of IL-6 produced from the macrophage and the IL-6r expressed by the hepatocyte. If homeostasis levels of IL-6 and IL-6r are present, these pathways operate at the optimal repair rates.

3. TCE initiates inflammatory processes (e.g. redox disequilibrium) that move the LUs from the "H" to "C" state. It also decreases the protective effects of IL-6-signaling that would normally restore the LUs to the "H" state. These dual effects of TCE allow the inflammatory processes to progress and to move the LUs from the "C" to the "I" state.
4. Autoimmune hepatitis pathology does not occur without TCE, even if the IL-6 pathway is impaired in some other way.

Consistent with these assumptions, the rate terms above can be further specified as follows:

$$k_{REP,H-C} = k_1 \cdot f_{IL6} \quad ; \quad k_{REP,C-I} = k_2 \cdot f_{IL6} \quad ; \quad k_{DAM,H-C} = k_3 \quad ; \quad k_{DAM,C-I} = k_4 \cdot f_{TCE} \qquad (6.7)$$

where k_1, k_2, k_3, and k_4 are constants to be estimated using experimental data, f_{TCE} represents the administered TCE dose normalized by the upper dose used in this study (0.5 mg/ml or a time-weighted average of approximately 54 mg/kg/day), and f_{IL6} is the fraction of IL-6 expressed by the macrophage compared to control levels. To express the dependence of f_{IL6} on TCE dose, a sub-model based on a saturation mechanism was used:

$$f_{IL6} = 1 - \frac{\alpha \cdot f_{TCE}}{\beta + f_{TCE}} \qquad (6.8)$$

where α and β are constants to be derived from experimental data.

6.2.2.2 Predicting liver pathology scores

To compute overall liver pathology scores, the [H], [C], and [I] calculated from equations (2), (3), and (4) at the desired time point were used as weighting factors for the individual PS values corresponding to each of the model states. Mathematically, this can be expressed as

$$PS = \sum_{s=H,C,I} PS_s \cdot [s] \qquad (6.9)$$

where PS_s is the pathology score of a LU in states (see Table 6.1).

6.2.2.3 Software and modeling tools

The system of differential equations were solved using a fourth-order Runge-Kutta method implemented in the Python programming language (v2.7.6) [https://www.python.org/]. Parameter estimation was conducted using lsqfit (v4.6.1) [https://github.com/gplepage/lsqfit], a software package for non-linear least-squares fitting of noisy data.

6.3 RESULTS

6.3.1 *In vivo* mouse experiments

In this study, Gilbert and coworkers determined a multitude of *in vivo* results that were utilized for the toxicodynamic model. The following sections summarize these experimental findings, which were used in the development of the toxicodynamic model.

6.3.1.1 Dose-dependent effects of TCE on peritoneal macrophage activity

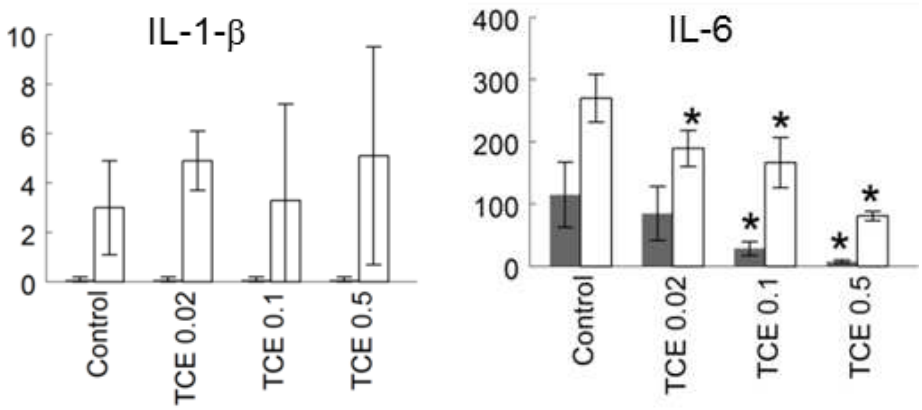

FIGURE 6.1. TCE inhibits macrophage IL-6 production in dose-dependent manner. Peritoneal macrophages were incubated with (open bars) or without LPS (shaded bars) following isolation from untreated control mice or from mice exposed to TCE at different concentrations for 12 weeks. Culture supernatants were examined for cytokines (mean ± SD). *Significantly different ($\alpha<0.05$) compared to control values.

Peritoneal macrophages from the mice exposed to different concentrations of TCE for 12 weeks were examined in Dr. Gilbert's lab for the production of macrophage-derived cytokines

IL-6 and IL-1β (Figure 6.1). Macrophage secretion of IL-1β is linked to a number of autoinflammatory diseases and an increase in this cytokine production following TCE exposure would indicate a possible mechanism for the observed AIH progression. However, secretion of IL-1β was unchanged by exposure to TCE. Comparatively, Figure 6.1 demonstrates that peritoneal macrophages collected from control mice secreted low but measurable levels of IL-6. Stimulation with LPS increased IL-6 production in all groups. However, both LPS-dependent and LPS-independent IL-6 production was suppressed in a dose-dependent manner in peritoneal macrophages from mice treated for 12 weeks with TCE. For example, LPS-induced IL-6 production in mice exposed to 0.5 mg/ml TCE was 70% lower than that of controls.

6.3.1.2 Time-dependent effects of TCE on peritoneal macrophage

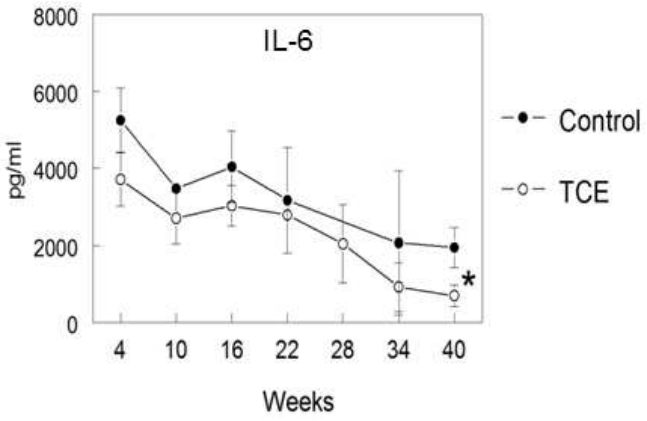

FIGURE 6.2. TCE inhibition IL-6 production is maintained over time. Peritoneal macrophages were incubated with LPS following isolation from untreated control mice or from mice exposed to TCE (0.5 mg/ml) for up to 40 weeks. Culture supernatants were examined for cytokines (mean ± SD). *Significantly different ($\alpha<0.05$) compared to control values.

In a second study designed to examine time-dependency of TCE-induced effects, mice were given drinking water alone or with 0.5 mg/ml TCE for 4, 10, 16, 22, 28, 34 or 40 weeks. Once again, TCE suppressed production of IL-6 (Figure 6.2). Also evident, but as yet

unexplained, was the general time-dependent decrease in IL-6 production in both treatment and control groups. A longitudinal evaluation of cytokine gene expression showed that the TCE-induced decrease in IL-6 expression by peritoneal macrophages was evident by 16 weeks of exposure. The time-dependent expression of several other genes for macrophage-derived cytokines, IL-1β, IL-12, IL-10, and Mmp12, were for the most part unaltered by exposure to TCE Thus, the primary effects of exposure to TCE on peritoneal macrophages was a decrease in IL-6 that was maintained for the duration of the study.

6.3.1.3 Time-dependent effects of TCE on liver events

Most of the protective and/or regenerative events in T cell-mediated liver injury are triggered by IL-6 signaling that is initiated when IL-6 binds to a complex comprised of the transmembrane protein gp130 and the IL-6R on hepatocytes [275]. In addition, experiments investigated hepatoprotection transcription factors such as EGR-1 [276] and demonstrated that the expression of EGR-1 in the liver was suppressed midway through the TCE exposure. In addition, increased expression of pro-inflammatory cytokines/chemokines such as TNF-α, osteopontin, serum amyloid A (SAA) and CXCL1, which have been implicated in the induction or progression of chronic liver inflammation [277–279]. Hepatic expression of these proteins remained unchanged throughout the exposure for TCE until the last 40-week time point in the TCE-exposed mice. At this last time point, hepatic expression of osteopoeitin increased dramatically. Using the dose-dependent and time-course results involving IL-6 secretion and gene expression alteration due to TCE exposure, Gilbert and coworkers determined that during most of the exposure, TCE appeared to negatively influence liver repair rather than directly promote inflammation. Only at the last time point was this reversed when several pro-

inflammatory cytokines/chemokines increased expression while the negative effect on hepatoprotective genes was overturned.

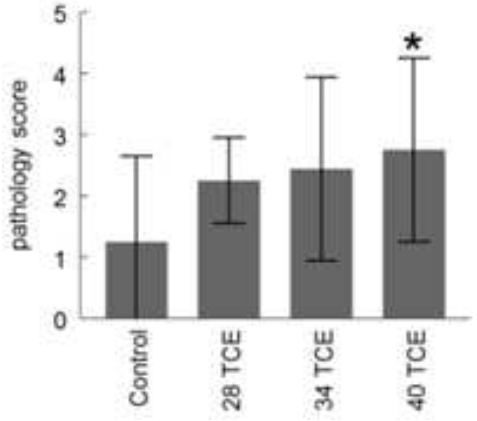

FIGURE 6.3. Liver pathology based on immune cell infiltration and inflammation was assessed in mice exposed to TCE (0.5mg/ml) for 28, 34 or40 weeks.

Finally, histopathology in the form of lymphoplasmacytic portal infiltrate and lobular inflammation in the liver was not noted until week 28 of TCE exposure, and became more robust during the course of the 40-week experiment (Figure 6.3). This pathology was characteristic of the early stages of autoimmune hepatitis; hepatocellular necrosis was only noted in a couple of instances. The mice were also examined for the generation of anti-liver antibodies as another readout of immune-mediated liver disease. MRL+/+ mice are noted for their age-dependent increase in the production of autoantibodies such as anti-nuclear antibodies, even in the absence of toxicant exposure [280]. In accord with this predisposition, the baseline production of anti-liver antibodies became more abundant in control mice at the 40 week time point. However, exposure to TCE further increased the levels and diversity of the anti-liver antibodies. Thus, the MRL+/+ mice treated with TCE for 40 weeks demonstrated liver inflammation and anti-liver autoantibody production consistent with AIH.

6.3.2 Toxicodynamic model for liver response to TCE exposure

Using the results from our collators, the computational aspect of this study aimed to develop a model to describe the effect of TCE on IL-6-mediated liver events. In order to develop this model, certain required parameters were estimated based on the results described above.

6.3.2.1 Parameter estimation

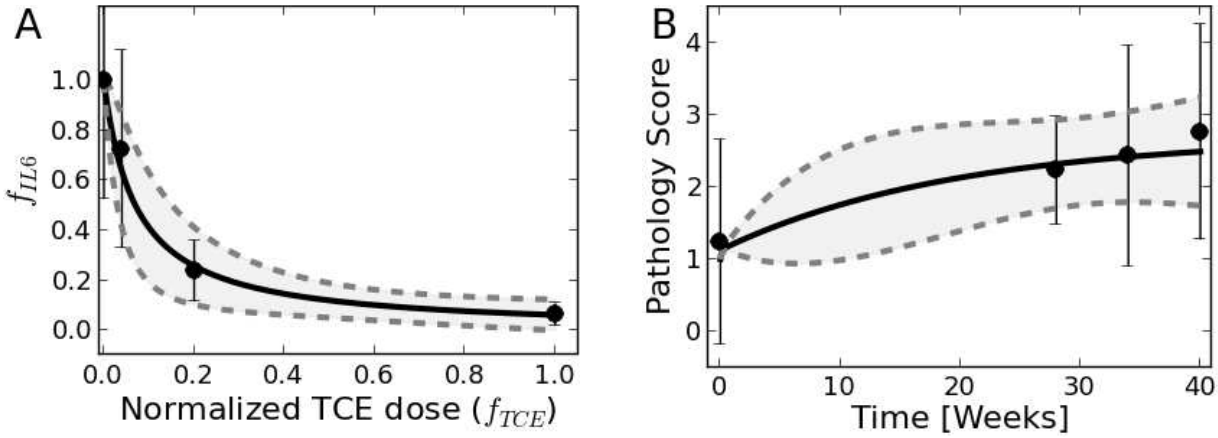

FIGURE 6.4. Submodel for parameter estimation. A) An IL-6 submodel was developed for estimating dose-dependent reduction in the fraction of IL-6 expressed by the macrophage. Points and error bars represent data and uncertainty, while solid and dashed lines are the mean and 95% confidence intervals from model predictions. B) Time-course pathology scores were used to extrapolate liver pathology based on time of TCE exposure. Points and error bars represent data and uncertainty, while solid and dashed lines are the mean and 95% confidence intervals from model predictions.

In order to fit a curve that could be used to extrapolate IL-6 effects across a range of TCE doses, values of α and β in the IL-6 submodel, Eq. (6.8), were estimated using a nonlinear least-squares approach with the non-LPS induced IL-6. The resulting parameter values, mean (variance), were found to be α = 1.01 (0.01) and β = 0.071 (0.003). Figure 6.4A illustrates the resulting fit of the experimental data to the IL-6 submodel.

It was similarly necessary to fit a curve to extrapolate liver pathology based on time of TCE exposure. The rate constants, k_i, defined in Eq. (6.7), were estimated based on experimental

time-course pathology scores to be k_1 = 101.5 (98.0), k_2 = 0.39 (0.18), k_3 = 1.02 (0.08), and k_4 = 0.21 (0.16). The resulting fit of the data to the mathematical model is depicted in Figure 6.4B. The uncertainty shown in model simulations results from both the uncertainty in the parameters associated with the IL-6 submodel and that from *in vivo* pathology scores.

6.3.2.2 Simulations of liver unit health states and the dose response

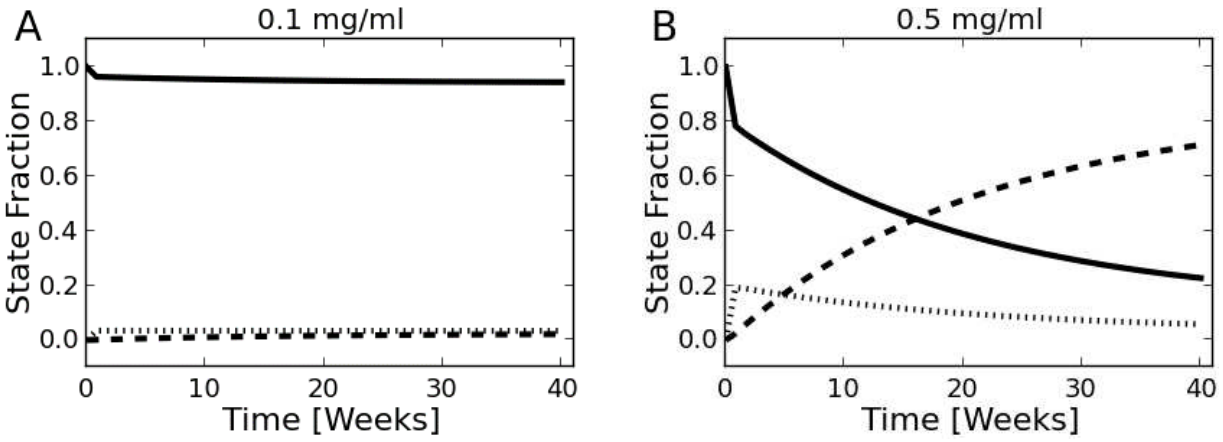

FIGURE 6.5. Liver unit state predictions based on the model. Fraction of liver units in each state for the 0.1 (A) and 0.5 (B) mg/ml experimental doses. Solid lines represent the H state, while vertical (||) and dashed (--) lines correspond to the C and I states, respectively.

Following parameter estimation, simulations of time-course LU health were conducted. Figure 6.5 illustrates results from several such studies, where the fraction of LUs in a particular health state are shown as a function of time at the two highest doses used in the experimental study. For the 0.1 mg/ml dose (Figure 6.5A), almost all of the LUs are in a healthy state. However, as the external TCE dose is increased to 0.5 mg/ml (Figure 6.5B), the abundance of healthy LUs decreases while those in the compromised/inflamed state increase in a non-linear manner. At doses less than 0.1 mg/ml, simulations indicated that virtually all of the LUs were in the healthy (H) state over time.

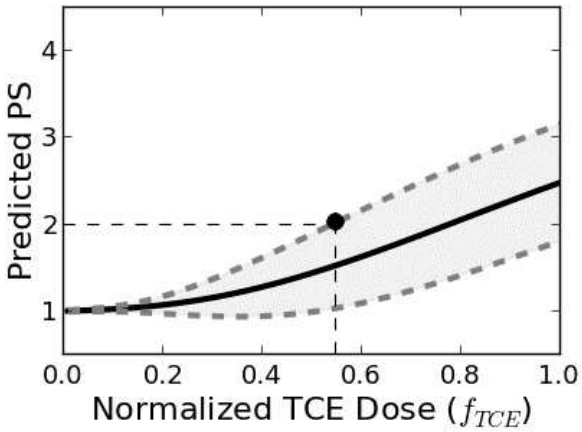

FIGURE 6.6. Dose response curve for current study. Predicted dose response curves for pathology scores (PS) 40 weeks post TCE exposure. The mean values and 95% confidence intervals are shown as solid and dashed lines, respectively. The point represents the value of the benchmark dose (BMD) corresponding to the benchmark response level (BMR) described in the text.

One of the benefits of the mathematical model is the prediction of system variables and endpoints not directly measured during the course of the studies. For instance, using 40-week pathology scores as an endpoint, the model was used to generate a dose-response curve (Figure 6.6). This curve can be used to relate this endpoint to any dose within the predicted range. As an example, for a benchmark response level (BML) corresponding to mild inflammation of 25% or less of the portal regions of the liver (PS=2), the benchmark dose (BMD) was estimated to be f_{TCE} = 0.55, corresponding to a 0.27 mg/ml dose, or approximately 37 mg/kg/day, of continuous TCE exposure.

6.3.2.3 Examining the impact of varying relative rates of damage and repair

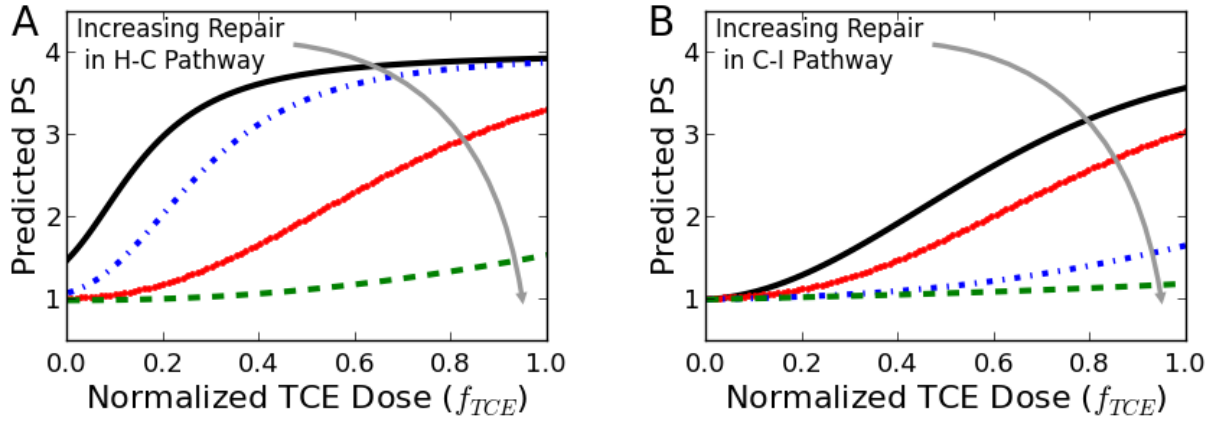

FIGURE 6.7. Simulations illustrate the effects of relative rates of repair and damage on liver damage. Model predictions for varying relative levels of repair in (A) the H-C pathway ($\kappa_{H-C}=[1,10,100,1000]$, $\kappa_{C-I}=1$) and (B) the C-I pathway ($\kappa_{H-C}=100$, $\kappa_{C-I}=[0.1,1,10,100]$). $\kappa_{H-C}=100$ and $\kappa_{C-I}=1$ are the values that that relate to the pathology scores from the current study.

Another important benefit to the mathematical modeling is the ability to vary system parameters and observe the effects on system states of interest. Here, the effects of varying the relative rates of damage and repair in the H-C and C-I state transitions were investigated through a parametric study. Since each damage and repair pathway is first order with respect to the abundance of LUs, ratios of rate constants were defined:

$$\kappa_{H-C}=\frac{k_{REP,H-C}}{k_{DAM,H-C}} \quad ; \quad \kappa_{C-I}=\frac{k_{REP,C-I}}{k_{DAM,C-I}} \tag{6.10}$$

By conducting simulations with varying values for κ (Figure 6.7), the effects of relative rates of repair and damage in the system could be examined. If $\kappa >> 1$, the repair mechanism dominates and the LUs tend toward a relatively low value of PS, even at higher TCE dose; conversely, if $\kappa << 1$, the damage mechanism dominates for the given pathway and LUs may acquire high values of PS values, even at relatively low doses. As can be seen, the shape and

nonlinearity of the dose-response curve is highly dependent on the relative rates of repair and damage in both of the health state transitions. Overall, such predictions can help in the understanding of the interactions in this system and lend insight into the effects of non-TCE mediated events, such as additional oxidative stress from hepatotoxicants or impaired IL-6 repair mechanisms.

6.4 DISCUSSION

MRL+/+mice can spontaneously develop autoimmune diseases such as lupus nephritis, pancreatitis, and Sjogren's syndrome late in life (after 1-year of age) [281,282]. However, before they reach one year of age most female MRL+/+mice do not exhibit autoimmune tissue pathology, and are often used to examine the autoimmune-promoting capacity of a toxicant such as TCE. Based on water consumption and TCE degradation in the water bottles, the mice given water containing TCE at 0.02, 0.1 or 0.5 mg/ml for 12 weeks were exposed to TCE at time-weighted levels of approximately 3, 14 or 64 mg/kg/day, respectively. Even the highest exposure is lower than the current 8-hour Permissible Exposure Limit [established by the Occupational Safety and Health Administration (OSHA)] for TCE of 100 ppm or approximately 76 mg/kg/day. The results of the current study showed that oral exposure to TCE suppressed IL-6 at the level of protein production and gene expression in macrophages.

IL-6 is a pleiotropic cytokine, which can make it difficult to predict the cumulative impact of its altered production. Elevated levels of IL-6 in the blood have been observed in a number of pathological conditions associated with chronic inflammation including rheumatoid arthritis [283], systemic lupus erythematosus [284], and active disease in Guillain-Barre syndrome [285]. While local levels of IL-6 increased from peritoneal macrophages, circulating levels of IL-6 did not reach detectable levels in the blood of control or TCE-treated mice in the

current experimental study conducted by Gilbert and coworkers. However, some studies of idiopathic autoimmune disease in humans have found increased levels of IL-6 in liver biopsies [278], while other studies of AIH have demonstrated decreased expression of hepatic IL-6 in the liver [286]. On the other hand, treatments to prevent or reverse immunological liver injury in mouse models have been associated with an increase in liver expression of IL-6 [269]. Thus, the majority of studies suggest that in the liver, IL-6 is a primary protective cytokine. The *in vivo* experiments completed in this study demonstrated a decrease in macrophage-derived IL-6 following chronic exposure to TCE.

The complexity of chronic inflammatory diseases, whether idiopathic or chemically-induced, can make it difficult to identify lynchpin events best targeted for prevention or reversal. Toxicodynamic modeling can be a way to describe and quantify the contribution of these different disease-induced alterations to actual pathology. The contribution of TCE to AIH in the present model is multidimensional; the healthy-to-inflamed state model described here can be amended to include more immune parameters such as the contribution of CD4+ T cells as they are characterized. However, even in its present state, the model facilitated point-of-departure predictions based on dose-dependent changes in liver pathology. The model stemmed from the linear regression analyses showing that liver pathology in TCE-treated mice was best correlated with the decreased liver expression of macrophage Il-6r. We now have the tools to predict liver pathology based on relative rates of liver repair and damage.

In addition to its predicted effect on IL-6 signaling the model also infers that TCE initiates inflammatory processes that transition LUs from “H” to “C”. These processes were not investigated in this study, but probably include, but are not restricted to, alterations in redox equilibrium. In a previous study conducted by Dr. Gilbert’s lab, a metabolomics analysis

following chronic 32 week exposure to 0.5 mg/ml in MRL+/+mice revealed significant alterations in several metabolites (e.g., cystathionine) involved in the generation of glutathione, which functions as the major intracellular antioxidant against oxidative stress and plays an important role in the detoxification of reactive oxygen species and subsequent oxidative damage from pro-oxidant environmental exposures. Others have shown the functional significance of oxidative stress in TCE-induced liver pathology [287,288]. IL-6 has been shown to inhibit oxidative stress and steatosis in the liver [271]. Consequently, a TCE-induced loss of IL-6 signaling in the liver would be expected to exacerbate associated oxidative-stress and resulting inflammation. The first stage model development described here (i.e. generation of equations and description of parameters) was based on data from two different experiments, albeit with some differences in experimental design. Obtaining new data to validate and extend this model will be included in the design of future chronic TCE exposure studies.

CHAPTER 7

CONCLUSIONS AND PERSPECTIVES

The research presented throughout this dissertation centered on the development, validation, and application of novel computational tools for determining biological endpoints for real-world problems pertaining to toxicology and pharmacology. While each chapter contained its own set of conclusions specific to the xenobiotic of interest, ultimately, this research demonstrated how *in silico* modeling can serve as a third pillar in solving biological problems by complementing *in vivo* and *in vitro* experimentation. The following summarizes each project and suggests how these results could be applied to future endeavors in computational pharmacology and toxicology.

The first two chapters of this research presented physiologically-based pharmacokinetic models to predict the absorption, distribution, metabolism, and elimination of two important pharmaceutical agents: rifapentine and acetaminophen. In contrast to traditional PBPK models, these analyses were conducted using a Bayesian population methodology for parameter estimation. In addition to the determination of concentration distributions in various parts of the body, the Bayesian hierarchical framework allowed for the characterization of population variability and model uncertainty for each drug. In this context, chapters three and four illustrated the ability of such models to (i) predict numerous biological endpoints, such as tissue-specific drug concentrations to evaluate drug safety or efficacy, (ii) quantify changes in pharmacokinetics arising from genetic differences in various subpopulations, (iii) estimate ingested dose from measurable biomarkers, and (iv) the optimize biomarker sampling times to increase certainty in predictions of ingested dose.

In addition to the above, this dissertation highlighted the utility of biologically-based modeling to develop environmental public health indicators that can be used to protect against adverse health outcomes following exposure to the environmental toxicant chlorpyrifos. In this case, the modeling approach opened up multiple possibilities for predicting neurobehavioral deficits using internal-dose concentration predictions in the brain as well as the correlation of measurable biomarkers of exposure to these neurobehavioral deficits. For example, this research led to an innovative methodology for establishing a source-to-outcome pathway model for predicting cognitive deficits following exposure to an organophosphate insecticide.

The final aspect of this dissertation was a demonstration of how a validated pharmacodynamic model can be used to predict biological responses following exposure to the toxicant, trichloroethylene. The approach used facilitated hypothesis testing and allowed for different mechanisms of toxicity to be compared and quantified to arrive at a plausible mechanism for TCE-induce autoimmune hepatitis. It is anticipated that this general approach will be useful to a variety of researchers interested in predicting pathology endpoints following low-dose, chronic exposure to trichloroethylene.

The current literature indicates a shift in the landscape for determining biological outcomes following xenobiotic exposure. As stated in the introduction, there is mounting pressure from many regulatory agencies, non-governmental agencies, and private companies to move toxicity and efficacy studies away from animal testing to more resource efficient, and humane, approaches. Fortunately, this shift is being facilitated by significant advances in *in vitro* and *in silico* technologies. The advances in *in vitro* technologies include stem-cell derived human cells, three-dimensional tissue scaffolds, and high-throughput cellular assays, while those in the *in silico* domain include significant computational efficiency improvements and cost reductions

in hardware coupled with advances in areas such as bioinformatics, machine learning, network and pathway analysis, and whole-cell and tissue-scale modeling. Through this shift, resources and costs associated with toxicological and pharmacological research can be significantly reduced and the space of chemicals being studied dramatically expanded.

Overall, this dissertation highlighted research focused on the development and application of *in silico* methods underpinned by results from *in vitro* and *in vivo* systems. These methods ultimately improved predictions of xenobiotic fate and effect and specifically addressed needs in the fields of toxicology and pharmacology related to pharmacokinetics across populations, susceptible populations, dose reconstruction, environmental public health indicators for risk estimation, and complex toxicant-mediated adverse health effects. Ultimately, the development and use of such mathematical and computational models is expected to dramatically increase over time, resulting in more cost-effective approaches in fields ranging from environmental health to pharmaceutical research.

BIBLIOGRAPHY

1. Johnson CH, Patterson AD, Idle JR, Gonzalez FJ (2012) Xenobiotic metabolomics: major impact on the metabolome. Annu Rev Pharmacol Toxicol 52: 37–56. Available: http://www.ncbi.nlm.nih.gov/pubmed/21819238.
2. Eaton DL, Gilbert SG (2008) Principles of Toxicology. In: Klaassen CD, editor. Casarett and Doull's toxicology: The basic science of poisons. New York: McGraw-Hill. pp. 11–43.
3. Allen DD, Caviedes R, Cárdenas AM, Shimahara T, Segura-Aguilar J, et al. (2005) Cell lines as in vitro models for drug screening and toxicity studies. Drug Dev Ind Pharm 31: 757–768. Available: http://www.ncbi.nlm.nih.gov/pubmed/16221610.
4. Soldatow VY, Lecluyse EL, Griffith LG, Rusyn I (2013) In vitro models for liver toxicity testing. Toxicol Res (Camb) 2: 23–39. Available: http://www.ncbi.nlm.nih.gov/pubmed/23495363.
5. Jia L, Liu X (2007) The conduct of drug metabolism studies considered good practice (II): in vitro experiments. Curr Drug Metab 8: 822–829. Available: http://www.ncbi.nlm.nih.gov/pubmed/18220563.
6. De Buck SS, Sinha VK, Fenu LA, Gilissen RA, Mackie CE, et al. (2007) The prediction of drug metabolism, tissue distribution, and bioavailability of 50 structurally diverse compounds in rat using mechanism-based absorption, distribution, and metabolism prediction tools. Drug Metab Dispos 35: 649–659. Available: http://www.ncbi.nlm.nih.gov/pubmed/17267621.
7. Rotroff DM, Dix DJ, Houck KA, Knudsen TB, Martin MT, et al. (2013) Using in vitro

high throughput screening assays to identify potential endocrine-disrupting chemicals. Environ Health Perspect 121: 7–14. Available: http://www.ncbi.nlm.nih.gov/pubmed/23052129.

8. Rastogi N, Goh KS, Berchel M, Bryskier a (2000) Activity of rifapentine and its metabolite 25-O-desacetylrifapentine compared with rifampicin and rifabutin against Mycobacterium tuberculosis, Mycobacterium africanum, Mycobacterium bovis and M. bovis BCG. J Antimicrob Chemother 46: 565–570. doi:10.1093/jac/46.4.565.

9. Grigore L, Norata GD, Catapano AL (2008) Combination therapy in cholesterol reduction: focus on ezetimibe and statins. Vasc Health Risk Manag 4: 267–278. Available: http://www.ncbi.nlm.nih.gov/pubmed/18561502.

10. Shen J, Burgess DJ (2013) In Vitro Dissolution Testing Strategies for Nanoparticulate Drug Delivery Systems: Recent Developments and Challenges. Drug Deliv Transl Res 3: 409–415. Available: http://www.ncbi.nlm.nih.gov/pubmed/24069580.

11. Andrews JM (2001) Determination of minimum inhibitory concentrations. J Antimicrob Chemother 48 Suppl 1: 5–16. Available: http://www.ncbi.nlm.nih.gov/pubmed/11420333.

12. Eldefrawi AT, Jett D, Eldefrawi ME (1992) Direct actions of organophosphate anticholinesterases on muscarinic receptors. In: Chambers JE, Levi PE, editors. Organophosphates: Chemistry, Fate, and Effects. New York: Academic Press. pp. 257–270.

13. Peter JV, Sudarsan TI, Moran JL (2014) Clinical features of organophosphate poisoning: A review of different classification systems and approaches. Indian J Crit Care Med 18: 735–745. Available: http://www.ncbi.nlm.nih.gov/pubmed/25425841.

14. Chambers HW (1992) Organophosphorus compunds: An overview. In: Chambers JE, Levi

PE, editors. Organophosphates: Chemistry, Fate, and Effects. New York: Academic Press. pp. 3–17.

15. Judson RS, Houck KA, Kavlock RJ, Knudsen TB, Martin MT, et al. (2010) In vitro screening of environmental chemicals for targeted testing prioritization: the ToxCast project. Environ Health Perspect 118: 485–492. Available: http://www.ncbi.nlm.nih.gov/pubmed/20368123.

16. Auerbach S, Filer D, Reif D, Walker V, Holloway AC, et al. (2016) Prioritizing Environmental Chemicals for Obesity and Diabetes Outcomes Research: A Screening Approach Using ToxCast™ High-Throughput Data. Environ Health Perspect 124: 1141–1154. Available: http://www.ncbi.nlm.nih.gov/pubmed/26978842.

17. Hartung T, Daston G (2009) Are in vitro tests suitable for regulatory use? Toxicol Sci 111: 233–237. doi:10.1093/toxsci/kfp149.

18. Ferdowsian HR, Beck N (2011) Ethical and scientific considerations regarding animal testing and research. PLoS One 6: e24059. Available: http://www.ncbi.nlm.nih.gov/pubmed/21915280.

19. Veldman MB, Lin S (2008) Zebrafish as a developmental model organism for pediatric research. Pediatr Res 64: 470–476. Available: http://www.ncbi.nlm.nih.gov/pubmed/18679162.

20. Gilbert KM, Przybyla B, Pumford NR, Han T, Fuscoe J, et al. (2009) Delineating liver events in trichloroethylene-induced autoimmune hepatitis. Chem Res Toxicol 22: 626–632. Available: http://www.ncbi.nlm.nih.gov/pubmed/19254012.

21. Faustman EM, Omenn GS (2008) Risk assessment. In: Klaassen CD, editor. Casarett and Doull's toxicology: The basic science of poisons. New York: McGraw-Hill. pp. 107–128.

22. Coecke S, Pelkonen O, Leite SB, Bernauer U, Bessems JG, et al. (2013) Toxicokinetics as a key to the integrated toxicity risk assessment based primarily on non-animal approaches. Toxicol In Vitro 27: 1570–1577. Available: http://www.ncbi.nlm.nih.gov/pubmed/22771339.

23. Sauer JM, Kleensang A, Peitsch MC, Hayes AW (2016) Advancing Risk Assessment through the Application of Systems Toxicology. Toxicol Res 32: 5–8. Available: http://www.ncbi.nlm.nih.gov/pubmed/26977253.

24. Basketter DA, Clewell H, Kimber I, Rossi A, Blaauboer B, et al. (2012) A roadmap for the development of alternative (non-animal) methods for systemic toxicity testing - t4 report*. ALTEX 29: 3–91. Available: http://www.ncbi.nlm.nih.gov/pubmed/22307314.

25. Shanks N, Greek R, Greek J (2009) Are animal models predictive for humans? Philos Ethics Humanit Med 4: 2. Available: http://www.ncbi.nlm.nih.gov/pubmed/19146696.

26. Knight A (2007) Systematic reviews of animal experiments demonstrate poor human clinical and toxicological utility. Altern Lab Anim 35: 641–659. Available: http://www.ncbi.nlm.nih.gov/pubmed/18186670.

27. Greek R, Menache A (2013) Systematic reviews of animal models: methodology versus epistemology. Int J Med Sci 10: 206–221. Available: http://www.ncbi.nlm.nih.gov/pubmed/23372426.

28. Seok J, Warren HS, Cuenca AG, Mindrinos MN, Baker H V, et al. (2013) Genomic responses in mouse models poorly mimic human inflammatory diseases. Proc Natl Acad Sci U S A 110: 3507–3512. Available: http://www.ncbi.nlm.nih.gov/pubmed/23401516.

29. European Commission (2013) COMMUNICATION FROM THE COMMISSION TO THE EUROPEAN PARLIAMENT AND THE COUNCIL on the animal testing and

marketing ban and on the state of play in relation to alternative methods in the field of cosmetics: 1–15.

30. Registration, Evaluation, Authorisation and Restriction of Chemicals (REACH) (2006).

31. Frank R. Lautenberg Chemical Safety for the 21st Century Act (2015).

32. Knudsen TB, Keller DA, Sander M, Carney EW, Doerrer NG, et al. (2015) FutureTox II: in vitro data and in silico models for predictive toxicology. Toxicol Sci 143: 256–267. Available: http://www.ncbi.nlm.nih.gov/pubmed/25628403.

33. Dearfield KL, Gollapudi BB, Bemis JC, Benz RD, Douglas GR, et al. (2016) Next generation testing strategy for assessment of genomic damage: A conceptual framework and considerations. Environ Mol Mutagen. Available: http://www.ncbi.nlm.nih.gov/pubmed/27650663.

34. Lin JH, Wong BK (2002) Complexities of glucuronidation affecting in vitro in vivo extrapolation. Curr Drug Metab 3: 623–646. Available: http://www.ncbi.nlm.nih.gov/pubmed/12369890.

35. Hartung T (2007) Food for thought... on cell culture. ALTEX 24: 143–152. Available: http://www.ncbi.nlm.nih.gov/pubmed/17926373.

36. Zurlinden TJ, Reisfeld B (2016) Physiologically based modeling of the pharmacokinetics of acetaminophen and its major metabolites in humans using a Bayesian population approach. Eur J Drug Metab Pharmacokinet 41: 267–280. Available: http://www.ncbi.nlm.nih.gov/pubmed/25636597.

37. Zurlinden TJ, Eppers GJ, Reisfeld B (2016) A physiologically-based pharmacokinetic model of rifapentine and 25-desacetyl-rifapentine disposition in humans. Antimicrob Agents Chemother. Available: http://www.ncbi.nlm.nih.gov/pubmed/27270284.

38. Lyons M, Reisfeld B, Yang RSH, Lenaerts AJ (2013) A physiologically based pharmacokinetic model of rifampin in mice. Antimicrob Agents Chemother 57: 1763–1771. Available: http://www.pubmedcentral.nih.gov/articlerender.fcgi?artid=3623338&tool=pmcentrez&rendertype=abstract. Accessed 5 November 2013.

39. Zurlinden TJ, Heard K, Reisfeld B (2015) A novel approach for estimating ingested dose associated with paracetamol overdose. Br J Clin Pharmacol 81: 634–645. Available: http://www.ncbi.nlm.nih.gov/pubmed/26441245.

40. Zurlinden TJ, Reisfeld B (2016) Characterizing the Effects of Race/Ethnicity on Acetaminophen Pharmacokinetics Using Physiologically Based Pharmacokinetic Modeling. Eur J Drug Metab Pharmacokinet. Available: http://www.ncbi.nlm.nih.gov/pubmed/26972700.

41. Yoon M, Kedderis GL, Yan GZ, Clewell HJ (2015) Use of in vitro data in developing a physiologically based pharmacokinetic model: Carbaryl as a case study. Toxicology 332: 52–66. Available: http://www.ncbi.nlm.nih.gov/pubmed/24863738.

42. Gilbert KM, Reisfeld B, Zurlinden TJ, Kreps MN, Erickson SW, et al. (2014) Modeling toxicodynamic effects of trichloroethylene on liver in mouse model of autoimmune hepatitis. Toxicol Appl Pharmacol 279: 284–293. Available: http://www.ncbi.nlm.nih.gov/pubmed/25026505.

43. Shargel L, Wu-Pong S, Yu ABC (2012) Applied biopharmaceutics and pharmacokinetics. 6th ed. New York: McGraw-Hill Medical.

44. Reisfeld B, Mayeno AN, Lyons MA, Yang, Raymond SH (2007) Physiologically based pharmacokinetic and pharmacodynamic modeling. In: Ekins S, editor. Computational

Toxicology: Risk assessment for pharmaceutical and environmental chemicals. Hoboken, NJ, USA: John Wiley & Sons, Inc. pp. 33–69.

45. Campbell JL, Clewell RA, Gentry PR, Andersen ME, Clewell HJ, et al. (2012) Physiologically Based Pharmacokinetic/Toxicokinetic Modeling. In: Reisfeld B, Mayeno AN, editors. Computational Toxicology. Methods in Molecular Biology. Totowa, NJ: Springer, Vol. 929. pp. 439–499. Available: http://www.ncbi.nlm.nih.gov/pubmed/23007440. Accessed 11 July 2014.

46. Woltosz WS, Bolger MB, Lukacova V (2012) Modeling of Absorption. In: Reisfeld B, Mayeno AN, editors. Computational Toxicology. Methods in Molecular Biology. Totowa, NJ: Humana Press, Vol. 929.

47. Dancik Y, Miller MA, Jaworska J, Kasting GB (2013) Design and performance of a spreadsheet-based model for estimating bioavailability of chemicals from dermal exposure. Adv Drug Deliv Rev 65: 221–236. Available: http://www.ncbi.nlm.nih.gov/pubmed/22285584.

48. Poet TS, Timchalk C, Hotchkiss J a., Bartels MJ (2014) Chlorpyrifos PBPK/PD model for multiple routes of exposure. Xenobiotica 44: 868–881. Available: http://www.ncbi.nlm.nih.gov/pubmed/24839995.

49. Rodgers T, Rowland M (2006) Physiologically based pharmacokinetic modelling 2: predicting the tissue distribution of acids, very weak bases, neutrals and zwitterions. J Pharm Sci 95: 1238–1257. Available: http://www.ncbi.nlm.nih.gov/pubmed/16639716. Accessed 13 November 2013.

50. Poulin P, Theil FP (2000) A priori prediction of tissue:plasma partition coefficients of drugs to facilitate the use of physiologically-based pharmacokinetic models in drug

discovery. J Pharm Sci 89: 16–35. Available: http://www.ncbi.nlm.nih.gov/pubmed/10664535.

51. Ballard P, Arundel PA, Leahy DE, Rowland M (2003) Prediction of in vivo tissue distribution from in vitro data. 2. Influence of albumin diffusion from tissue pieces during an in vitro incubation on estimated tissue-to-unbound plasma partition coefficients (Kpu). Pharm Res 20: 857–863. Available: http://www.ncbi.nlm.nih.gov/pubmed/12817888.

52. Knaak JB, Dary CC, Zhang X, Gerlach RW, Tornero-Velez R, et al. (2012) Parameters for pyrethroid insecticide QSAR and PBPK/PD models for human risk assessment. Rev Environ Contam Toxicol 219: 1–114. Available: http://www.ncbi.nlm.nih.gov/pubmed/22610175. Accessed 13 November 2013.

53. Madan AK, Dureja H (2013) Prediction of pharmacokinetic parameters. In: Reisfeld B, Mayeno AN, editors. Computational Toxicology. Methods in Molecular Biology. Totowa, NJ: Humana Press, Vol. 930. pp. 337–357. Available: http://link.springer.com/10.1007/978-1-62703-059-5.

54. Rollins DE, Klaassen CD (n.d.) Biliary excretion of drugs in man. Clin Pharmacokinet 4: 368–379. Available: http://www.ncbi.nlm.nih.gov/pubmed/389528.

55. Brown RP, Delp MD, Lindstedt SL, Rhomberg LR, Beliles RP (1997) Physiological parameter values for physiologically based pharmacokinetic models. Toxicol Ind Health 13: 407–484. Available: http://www.ncbi.nlm.nih.gov/pubmed/9249929. Accessed 19 February 2014.

56. Felmlee MA, Morris ME, Mager DE (2013) Mechanism-based pharmacodynamic modeling. In: Reisfeld B, Mayeno AN, editors. Computational Toxicology. Methods in Molecular Biology. Totowa, NJ: Humana Press, Vol. 930. pp. 583–600. Available:

http://link.springer.com/10.1007/978-1-62703-059-5.

57. Tam VH, Schilling AN, Lewis RE, Melnick DA, Boucher AN (2004) Novel approach to characterization of combined pharmacodynamic effects of antimicrobial agents. Antimicrob Agents Chemother 48: 4315–4321. Available: http://www.ncbi.nlm.nih.gov/pubmed/15504858.

58. Hope WW, Warn PA, Sharp A, Reed P, Keevil B, et al. (2005) Surface response modeling to examine the combination of amphotericin B deoxycholate and 5-fluorocytosine for treatment of invasive candidiasis. J Infect Dis 192: 673–680. Available: http://www.ncbi.nlm.nih.gov/pubmed/16028137.

59. Lyons M a., Lenaerts AJ (2015) Computational pharmacokinetics/pharmacodynamics of rifampin in a mouse tuberculosis infection model. J Pharmacokinet Pharmacodyn 42: 375–389. Available: http://link.springer.com/10.1007/s10928-015-9419-z.

60. Dayneka NL, Garg V, Jusko WJ (1993) Comparison of four basic models of indirect pharmacodynamic responses. J Pharmacokinet Biopharm 21: 457–478. Available: http://www.ncbi.nlm.nih.gov/pubmed/8133465.

61. Gordi T, Xie R, Jusko WJ (2005) Semi-mechanistic pharmacokinetic/pharmacodynamic modelling of the antimalarial effect of artemisinin. Br J Clin Pharmacol 60: 594–604. Available: http://www.ncbi.nlm.nih.gov/pubmed/16305583.

62. Jordan P, Gieschke R (2005) Explicit solutions for a class of indirect pharmacodynamic response models. Comput Methods Programs Biomed 77: 91–97. Available: http://www.ncbi.nlm.nih.gov/pubmed/15652631.

63. Rencher AC, Christensen WF (2012) Multivariate Regression. Methods of Multivariate Analysis. pp. 339–383. Available: http://doi.wiley.com/10.1002/9781118391686.ch10.

64. Chapra SC, Canale RP (2006) Linear Regression. Numerical Methods for Engineers. pp. 440–473.

65. Pedregosa F, Varoquaux G, Gramfort A, Michel V, Thirion B, et al. (2011) Scikit-learn: Machine learning in Python. J Mach Learn Res 12: 2825–2830.

66. Jones E, Oliphant TE, Peterson P (2001) SciPy: Open source scientific tools for Python: http://www.scipy.org/.

67. Statsmodel (2012). Available: http://statsmodels.sourceforge.net/.

68. R: A Language and Environment for Statistical Computing (2008). R Dev Core Team R Foundati. Available: http://www.r-project.org.

69. Lepage GP (2015) lsqfit. Available: https://github.com/gplepage/lsqfit.

70. NLopt Python Reference (n.d.). Available: http://ab-initio.mit.edu/wiki/index.php/NLopt_Python_Reference.

71. Bois FY (2013) Bayesian Inference. In: Reisfeld B, Mayeno AN, editors. Computational Toxicology. Methods in Molecular Biology. Totowa, NJ: Humana Press, Vol. 930. pp. 597–636. doi:10.1007/978-1-62703-059-5.

72. Gilks WR, Richardson S, Spiegelhalter DJ (1996) Markov chain Monte carlo in practice. New York: Chapman and Hall/CRC. 1-19 p.

73. Gelman A, Shirley K (2011) Inference from Simulations and Monitoring Convergence. In: Brooks S, Gelman A, Jones GL, Meng X-L, editors. Handbook of Markov Chain Monte Carlo. Chapman and Hall. pp. 163–174. doi:10.1201/b10905-7.

74. Jonsson F, Johanson G (2003) The Bayesian population approach to physiological toxicokinetic-toxicodynamic models - An example using the MCSim software. Toxicol Lett 138: 143–150. doi:10.1016/S0378-4274(02)00369-7.

75. Patil A, Huard D, Fonnesbeck CJ (2010) PyMC: Bayesian Stochastic Modelling in Python. J Stat Softw 35: 1–81. Available: http://www.ncbi.nlm.nih.gov/pubmed/21603108.

76. Plummer M (2003) JAGS: A program for analysis of Bayesian graphical models using Gibbs sampling.

77. Bois FY (2009) GNU MCSim: Bayesian statistical inference for SBML-coded systems biology models. Bioinformatics 25: 1453–1454. Available: http://www.ncbi.nlm.nih.gov/pubmed/19304877. Accessed 9 February 2012.

78. World Health Organization (2013) Global Tuberculosis Report. Available: http://www.who.int/tb/publications/global_report/en/.

79. D'Ambrosio L, Centis R, Sotgiu G, Pontali E, Spanevello A, et al. (2015) New anti-tuberculosis drugs and regimens: 2015 update. ERJ Open Res 1: 00010–02015. Available: http://openres.ersjournals.com/lookup/doi/10.1183/23120541.00010-2015.

80. Ma Z, Ginsburg AM, Spigelman M (2007) Antibacterial: anti-mycobacterial agents. In: Taylor JB, Triggle D, editors. Comprehensive Medicinal Chemistry II. Oxford: Elsevier.

81. Ma Z, Lienhardt C, McIlleron H, Nunn AJ, Wang X (2010) Global tuberculosis drug development pipeline: the need and the reality. Lancet (London, England) 375: 2100–2109. Available: http://www.ncbi.nlm.nih.gov/pubmed/20488518.

82. Dorman SE, Savic RM, Goldberg S, Stout JE, Schluger N, et al. (2015) Daily rifapentine for treatment of pulmonary tuberculosis. A randomized, dose-ranging trial. Am J Respir Crit Care Med 191: 333–343. Available: http://www.ncbi.nlm.nih.gov/pubmed/25489785.

83. Dooley KE, Savic RM, Park J-G, Cramer Y, Hafner R, et al. (2015) Novel dosing strategies increase exposures of the potent antituberculosis drug rifapentine but are poorly

tolerated in healthy volunteers. Antimicrob Agents Chemother 59: 3399–3405. Available: http://www.ncbi.nlm.nih.gov/pubmed/4432148.

84. Zhang T, Zhang M, Rosenthal IM, Grosset JH, Nuermberger EL (2009) Short-course therapy with daily rifapentine in a murine model of latent tuberculosis infection. Am J Respir Crit Care Med 180: 1151–1158. doi:10.1164/rccm.200905-0795OC.

85. Dooley KE, Bliven-Sizemore EE, Weiner M, Lu Y, Nuermberger EL, et al. (2012) Safety and pharmacokinetics of escalating daily doses of the antituberculosis drug rifapentine in healthy volunteers. Clin Pharmacol Ther 91: 881–888. Available: http://www.ncbi.nlm.nih.gov/pubmed/22472995.

86. Savic RM, Lu Y, Bliven-Sizemore E, Weiner M, Nuermberger E, et al. (2014) Population pharmacokinetics of rifapentine and desacetyl rifapentine in healthy volunteers: Nonlinearities in clearance and bioavailability. Antimicrob Agents Chemother 58: 3035–3042. doi:10.1128/AAC.01918-13.

87. Zurlinden TJ, Eppers GJ, Reisfeld B (2016) Physiologically Based Pharmacokinetic Model of Rifapentine and 25-Desacetyl Rifapentine Disposition in Humans. Antimicrob Agents Chemother 60: 4860–4868. Available: http://www.ncbi.nlm.nih.gov/pubmed/27270284.

88. Chun LJ, Tong MJ, Busuttil RW, Hiatt JR (2009) Acetaminophen hepatotoxicity and acute liver failure. J Clin Gastroenterol 43: 342–349. doi:10.1097/MCG.0b013e31818a3854.

89. Perkins JD (2006) Acetaminophen sets records in the United States: Number 1 analgesic and number 1 cause of acute liver failure. Liver Transplant 12: 682–683. doi:10.1002/lt.20735.

90. Hawkins LC, Edwards JN, Dargan PI (2007) Impact of restricting paracetamol pack sizes on paracetamol poisoning in the United Kingdom: A review of the literature. Drug Saf 30: 465–479. doi:10.2165/00002018-200730060-00002.

91. Grube A, Donaldson D, Kiely T, Wu L, US Environmental Protection Agency (2011) Pesticide Industry Sales and Usage: 2006 and 2007 Market Estimates. Washington, DC. Available: http://www.epa.gov/opp00001/pestsales/07pestsales/market_estimates2007.pdf.

92. US Environmental Protection Agency (2006) Organophosphate pesticides (OP) cumulative assessment – 2006 update. Available: http://www.epa.gov/oppsrrd1/.

93. Reiss R, Neal B, Lamb JC, Juberg DR (2012) Acetylcholinesterase inhibition dose-response modeling for chlorpyrifos and chlorpyrifos-oxon. Regul Toxicol Pharmacol 63: 124–131. Available: http://dx.doi.org/10.1016/j.yrtph.2012.03.008.

94. Ross SM, McManus IC, Harrison V, Mason O (2013) Neurobehavioral problems following low-level exposure to organophosphate pesticides: a systematic and meta-analytic review. Crit Rev Toxicol 43: 21–44. Available: http://www.ncbi.nlm.nih.gov/pubmed/23163581.

95. Meyer-Baron M, Knapp G, Schäper M, van Thriel C (2015) Meta-analysis on occupational exposure to pesticides--neurobehavioral impact and dose-response relationships. Environ Res 136: 234–245. Available: http://www.ncbi.nlm.nih.gov/pubmed/25460642.

96. Blanc-Lapierre A, Bouvier G, Gruber A, Leffondré K, Lebailly P, et al. (2013) Cognitive disorders and occupational exposure to organophosphates: results from the PHYTONER study. Am J Epidemiol 177: 1086–1096. Available:

http://www.ncbi.nlm.nih.gov/pubmed/23535900.

97. Terry A V, Gearhart DA, Beck WD, Truan JN, Middlemore M-L, et al. (2007) Chronic, intermittent exposure to chlorpyrifos in rats: protracted effects on axonal transport, neurotrophin receptors, cholinergic markers, and information processing. J Pharmacol Exp Ther 322: 1117–1128. Available: http://www.ncbi.nlm.nih.gov/pubmed/17548533.

98. Middlemore-Risher ML, Buccafusco JJ, Terry A V (n.d.) Repeated exposures to low-level chlorpyrifos results in impairments in sustained attention and increased impulsivity in rats. Neurotoxicol Teratol 32: 415–424. Available: http://www.ncbi.nlm.nih.gov/pubmed/20350597.

99. Samsam TE, Hunter DL, Bushnell PJ (2005) Effects of chronic dietary and repeated acute exposure to chlorpyrifos on learning and sustained attention in rats. Toxicol Sci 87: 460–468. Available: http://www.ncbi.nlm.nih.gov/pubmed/16033991.

100. Yan C, Jiao L, Zhao J, Yang H, Peng S (2012) Repeated exposures to chlorpyrifos lead to spatial memory retrieval impairment and motor activity alteration. Neurotoxicol Teratol 34: 442–449. Available: http://www.ncbi.nlm.nih.gov/pubmed/22640976.

101. Byers VS, Levin AS, Ozonoff DM, Baldwin RW (1988) Association between clinical symptoms and lymphocyte abnormalities in a population with chronic domestic exposure to industrial solvent-contaminated domestic water supply and a high incidence of leukaemia. Cancer Immunol Immunother 27: 77–81. Available: http://www.ncbi.nlm.nih.gov/pubmed/3260823.

102. Yáñez Díaz S, Morán M, Unamuno P, Armijo M (1992) Silica and trichloroethylene-induced progressive systemic sclerosis. Dermatology 184: 98–102. Available: http://www.ncbi.nlm.nih.gov/pubmed/1323354.

103. Hansen BL, Isager H (1988) [A scleroderma-resembling disease--exposure to trichloroethylene and trichloroethane, is there a causal connection?]. Ugeskr Laeger 150: 805. Available: http://www.ncbi.nlm.nih.gov/pubmed/3363711.

104. Lockey JE, Kelly CR, Cannon GW, Colby T V, Aldrich V, et al. (1987) Progressive systemic sclerosis associated with exposure to trichloroethylene. J Occup Med 29: 493–496. Available: http://www.ncbi.nlm.nih.gov/pubmed/3612322.

105. Kamijima M, Wang H, Huang H, Li L, Shibata E, et al. (2008) Trichloroethylene causes generalized hypersensitivity skin disorders complicated by hepatitis. J Occup Health 50: 328–338. Available: http://www.ncbi.nlm.nih.gov/pubmed/18540116.

106. Burman WJ, Gallicano K, Peloquin C (2001) Comparative pharmacokinetics and pharmacodynamics of the rifamycin antibacterials. Clin Pharmacokinet 40: 327–341. doi:10.2165/00003088-200140050-00002.

107. Munsiff SS, Kambili C, Ahuja SD (2006) Rifapentine for the treatment of pulmonary tuberculosis. Clin Infect Dis 43: 1468–1475. doi:10.1086/508278.

108. Keung AC, Eller MG, Weir SJ (1998) Single-Dose Pharmacokineticsof Rifapentine in Women. J Pharmacokinet Biopharm 26: 75–85.

109. Keung AC, Eller MG, Weir SJ (1998) Single-dose pharmacokinetics of rifapentine in elderly men. Pharm Res 15: 1286–1291. doi:10.1023/A:1011960428896.

110. Keung AC, Eller MG, McKenzie KA, Weir SJ (1999) Single and multiple dose pharmacokinetics of rifapentine in man: Part II. Int J Tuberc Lung Dis 3: 437–444.

111. Keung AC, Eller MG, Weir SJ (1998) Pharmacokinetics of rifapentine in patients with varying degrees of hepatic dysfunction. J Clin Pharmacol 38: 517–524.

112. Langdon G, Wilkins JJ, Smith PJ, McIlleron H (2004) Consecutive-dose

pharmacokinetics of rifapentine in patients diagnosed with pulmonary tuberculosis. Int J Tuberc Lung Dis 8: 862–867.

113. Langdon G, Wilkins J, Mcfadyen L, Smith P, Simonsson USH, et al. (2005) Population Pharmacokinetics of Rifapentine and Its Primary Desacetyl Metabolite in South African Tuberculosis Patients Population Pharmacokinetics of Rifapentine and Its Primary Desacetyl Metabolite in South African Tuberculosis Patients. 49: 4429–4436. doi:10.1128/AAC.49.11.4429.

114. Weiner M, Bock N, Peloquin CA, Burman WJ, Khan A, et al. (2004) Pharmacokinetics of rifapentine at 600, 900, and 1,200 mg during once-weekly tuberculosis therapy. Am J Respir Crit Care Med 169: 1191–1197. Available: http://www.ncbi.nlm.nih.gov/pubmed/14962821. Accessed 7 November 2013.

115. Reith K, Keung A, Toren PC, Cheng L, Eller MG, et al. (1998) Disposition and metabolism of 14C-rifapentine in healthy volunteers. Drug Metab Dispos 26: 732–738.

116. Dooley K, Flexner C, Hackman J, Peloquin CA, Nuermberger E, et al. (2008) Repeated administration of high-dose intermittent rifapentine reduces rifapentine and moxifloxacin plasma concentrations. Antimicrob Agents Chemother 52: 4037–4042. doi:10.1128/AAC.00554-08.

117. Reisfeld B, Metzler CP, Lyons MA, Mayeno AN, Brooks EJ, et al. (2012) A Physiologically Based Pharmacokinetic Model for Capreomycin. Antimicrob Agents Chemother 56: 926–934. doi:10.1128/AAC.05180-11.

118. Yue WY, Cohen SS (1966) Toxic nephritis with acute renal insufficiency caused by administration of capreomycin. Case report with necropsy findings. Dis Chest 49: 549–551. doi:10.1378/chest.49.5.549.

119. Assandri A, Ratti B, Cristina T (1984) Pharmacokinetics of rifapentine, a new long lasting rifamycin, in the rat, the mouse and the rabbit. J Antibiot (Tokyo) 37: 1066–1075.

120. Nakajima A, Fukami T, Kobayashi Y, Watanabe A, Nakajima M, et al. (2011) Human arylacetamide deacetylase is responsible for deacetylation of rifamycins: Rifampicin, rifabutin, and rifapentine. Biochem Pharmacol 82: 1747–1756. Available: http://dx.doi.org/10.1016/j.bcp.2011.08.003.

121. Egelund EF, Weiner M, Singh RP, Prihoda TJ, Gelfond JAL, et al. (2014) Protein Binding of Rifapentine and Its 25-Desacetyl Metabolite in Patients with Pulmonary Tuberculosis. Antimicrob Agents Chemother 58: 4904–4910. Available: http://aac.asm.org/cgi/doi/10.1128/AAC.01730-13.

122. Lumen A, McNally K, George N, Fisher JW, Loizou GD (2015) Quantitative global sensitivity analysis of a biologically based dose-response pregnancy model for the thyroid endocrine system. Front Pharmacol 6: 107. Available: http://www.ncbi.nlm.nih.gov/pubmed/26074819.

123. Chiu WA, Okino MS, Evans M V (2009) Characterizing uncertainty and population variability in the toxicokinetics of trichloroethylene and metabolites in mice, rats, and humans using an updated database, physiologically based pharmacokinetic (PBPK) model, and Bayesian approach. Toxicol Appl Pharmacol 241: 36–60. Available: http://www.ncbi.nlm.nih.gov/pubmed/19660485. Accessed 13 November 2013.

124. Bormann I (n.d.) DigitizeIt. Available at http://www.digitizeit.de.

125. Python Language Reference version 2. 7. (n.d.) Python Software Foundation. Python Language Reference, version 2.7. Available: http://www.python.org. Accessed 11 October 2015.

126. van der Walt S, Colbert SC, Varoquaux G (2011) The NumPy Array: A Structure for Efficient Numerical Computation. Comput Sci Eng 13: 22–30. Available: http://scitation.aip.org/content/aip/journal/cise/13/2/10.1109/MCSE.2011.37. Accessed 16 July 2014.

127. Hunter JD (2007) Matplotlib: A 2D Graphics Environment. Comput Sci Eng 9: 90–95. Available: http://scitation.aip.org/content/aip/journal/cise/9/3/10.1109/MCSE.2007.55. Accessed 10 July 2014.

128. Global Alliance for TB Drug Development (2008) Handbook of Anti-Tuberculosis Agents. Tuberculosis 88: 85–170.

129. Targeted tuberculin testing and treatment of latent tuberculosis infection. American Thoracic Society. (2000). MMWR Recomm Rep 49: 1–51.

130. Swaminathan S, Narendran G, Venkatesan P, Iliayas S, Santhanakrishnan R, et al. (2010) Efficacy of a 6-month versus 9-month intermittent treatment regimen in HIV-infected patients with tuberculosis: A randomized clinical trial. Am J Respir Crit Care Med 181: 743–751. doi:10.1164/rccm.200903-0439OC.

131. Blumberg HM, Burman WJ, Chaisson RE, Daley CL, Etkind SC, et al. (2003) American Thoracic Society/Centers for Disease Control and Prevention/Infectious Diseases Society of America: treatment of tuberculosis. Am J Respir Crit Care Med 167: 603–662. Available: http://www.bmj.com/content/327/7419/822.extract.

132. California Department of Public Health (2016) Fact Sheet: 12-dose Isoniazid (INH)/Rifapentine regimen for latent TB infection treatment. Available: https://www.cdph.ca.gov/programs/tb/Documents/TBCB-INH-RIF-LTBI-fact-sheet.pdf.

133. Chang KC, Leung CC, Yew WW, Chan SL, Tam CM (2006) Dosing schedules of 6-

month regimens and relapse for pulmonary tuberculosis. Am J Respir Crit Care Med 174: 1153–1158. Available: http://www.ncbi.nlm.nih.gov/pubmed/16908866.

134. Saukkonen JJ, Cohn DL, Jasmer RM, Schenker S, Jereb JA, et al. (2006) An Official ATS Statement: Hepatotoxicity of Antituberculosis Therapy. Am J Respir Crit Care Med 174: 935–952. Available: http://www.atsjournals.org/doi/abs/10.1164/rccm.200510-1666ST.

135. Pienaar E, Dartois V, Linderman JJ, Kirschner DE (2015) In silico evaluation and exploration of antibiotic tuberculosis treatment regimens. BMC Syst Biol 9: 79. Available: http://www.biomedcentral.com/1752-0509/9/79.

136. Chan MT, Anderson PJ, Chan JC, Lau GS, Critchley JA (1997) Single-dose pharmacokinetics of paracetamol and its conjugates in Chinese non-insulin-dependent diabetic patients with renal impairment. Eur J Clin Pharmacol 52: 285–288. Available: http://www.ncbi.nlm.nih.gov/pubmed/9248766.

137. Critchley JA, Critchley LA, Anderson PJ, Tomlinson B (2005) Differences in the single-oral-dose pharmacokinetics and urinary excretion of paracetamol and its conjugates between Hong Kong Chinese and Caucasian subjects. J Clin Pharm Ther 30: 179–184. Available: http://www.ncbi.nlm.nih.gov/pubmed/15811172.

138. Critchley JA, Nimmo GR, Gregson CA, Woolhouse NM, Prescott LF (1986) Inter-subject and ethnic differences in paracetamol metabolism. Br J Clin Pharmacol 22: 649–657. Available: http://www.pubmedcentral.nih.gov/articlerender.fcgi?artid=1401198&tool=pmcentrez&rendertype=abstract.

139. Ameer B, Greenblatt DJ, Divoll M, Abernethy DR, Shargel L (1981) High-performance liquid chromatographic determination of acetaminophen in plasma: single-dose

pharmacokinetic studies. J Chromatogr 226: 224–230. Available: http://www.ncbi.nlm.nih.gov/pubmed/7320146. Accessed 19 February 2014.

140. Chen L, Mohr SN, Yang CS (1996) Decrease of plasma and urinary oxidative metabolites of acetaminophen after consumption of watercress by human volunteers. Clin Pharmacol Ther 60: 651–660. Available: http://www.ncbi.nlm.nih.gov/pubmed/8988067. Accessed 19 February 2014.

141. Chiew A, Day P, Salonikas C, Naidoo D, Graudins A, et al. (2010) The comparative pharmacokinetics of modified-release and immediate-release paracetamol in a simulated overdose model. Emerg Med Australas 22: 548–555. Available: http://www.ncbi.nlm.nih.gov/pubmed/21143403. Accessed 19 February 2014.

142. Esteban A, Calvo R, Pérez-Mateo M (n.d.) Paracetamol metabolism in two ethnically different Spanish populations. Eur J Drug Metab Pharmacokinet 21: 233–239. Available: http://www.ncbi.nlm.nih.gov/pubmed/8980921. Accessed 19 February 2014.

143. Jensen LS, Valentine J, Milne RW, Evans AM (2004) The quantification of paracetamol, paracetamol glucuronide and paracetamol sulphate in plasma and urine using a single high-performance liquid chromatography assay. J Pharm Biomed Anal 34: 585–593. Available: http://linkinghub.elsevier.com/retrieve/pii/S0731708503005739. Accessed 19 February 2014.

144. Itoh H, Nagano T, Takeyama M (2002) Effect of nizatidine on paracetamol and its metabolites in human plasma. J Pharm Pharmacol 54: 869–873. Available: http://www.ncbi.nlm.nih.gov/pubmed/12079004. Accessed 19 February 2014.

145. Kamali F (1993) The effect of probenecid on paracetamol metabolism and pharmacokinetics. Eur J Clin Pharmacol 45: 551–553. Available:

http://www.ncbi.nlm.nih.gov/pubmed/8157041.

146. Kim D-W, Tan EY, Jin Y, Park S, Hayes M, et al. (2011) Effects of imatinib mesylate on the pharmacokinetics of paracetamol (acetaminophen) in Korean patients with chronic myelogenous leukaemia. Br J Clin Pharmacol 71: 199–206. Available: http://www.pubmedcentral.nih.gov/articlerender.fcgi?artid=3040540&tool=pmcentrez&rendertype=abstract. Accessed 24 July 2014.

147. Lau GS, Critchley JA (1994) The estimation of paracetamol and its major metabolites in both plasma and urine by a single high-performance liquid chromatography assay. J Pharm Biomed Anal 12: 1563–1572. Available: http://www.ncbi.nlm.nih.gov/pubmed/7696381.

148. Prescott LF (1980) Kinetics and metabolism of paracetamol and phenacetin. Br J Clin Pharmacol 10 Suppl 2: 291S–298S. Available: http://www.pubmedcentral.nih.gov/articlerender.fcgi?artid=1430174&tool=pmcentrez&rendertype=abstract.

149. Prescott LF, Speirs GC, Critchley JA, Temple RM, Winney RJ (1989) Paracetamol disposition and metabolite kinetics in patients with chronic renal failure. Eur J Clin Pharmacol 36: 291–297. Available: http://www.ncbi.nlm.nih.gov/pubmed/2744070.

150. Rawlins MD, Henderson DB, Hijab a R (1977) Pharmacokinetics of paracetamol (acetaminophen) after intravenous and oral administration. Eur J Clin Pharmacol 11: 283–286. Available: http://www.ncbi.nlm.nih.gov/pubmed/862649. Accessed 19 February 2014.

151. Shinoda S, Aoyama T, Aoyama Y, Tomioka S, Matsumoto Y, et al. (2007) Pharmacokinetics/pharmacodynamics of acetaminophen analgesia in Japanese patients

with chronic pain. Biol Pharm Bull 30: 157–161. Available: http://www.ncbi.nlm.nih.gov/pubmed/17202677.

152. Tan Q, Zhu R, Li H, Wang F, Yan M, et al. (2012) Simultaneous quantitative determination of paracetamol and its glucuronide conjugate in human plasma and urine by liquid chromatography coupled to electrospray tandem mass spectrometry: application to a clinical pharmacokinetic study. J Chromatogr B Analyt Technol Biomed Life Sci 893–894: 162–167. Available: http://www.ncbi.nlm.nih.gov/pubmed/22445307. Accessed 19 February 2014.

153. Tonoli D, Varesio E, Hopfgartner G (2012) Quantification of acetaminophen and two of its metabolites in human plasma by ultra-high performance liquid chromatography-low and high resolution tandem mass spectrometry. J Chromatogr B Analyt Technol Biomed Life Sci 904: 42–50. Available: http://www.ncbi.nlm.nih.gov/pubmed/22867840. Accessed 19 February 2014.

154. Volak LP, Hanley MJ, Masse G, Hazarika S, Harmatz JS, et al. (2013) Effect of a herbal extract containing curcumin and piperine on midazolam, flurbiprofen and paracetamol (acetaminophen) pharmacokinetics in healthy volunteers. Br J Clin Pharmacol 75: 450–462. Available: http://www.pubmedcentral.nih.gov/articlerender.fcgi?artid=3579260&tool=pmcentrez&rendertype=abstract. Accessed 19 February 2014.

155. Yin OQ, Tomlinson B, Chow a H, Chow MS (2001) Pharmacokinetics of acetaminophen in Hong Kong Chinese subjects. Int J Pharm 222: 305–308. Available: http://www.ncbi.nlm.nih.gov/pubmed/11427360.

156. Zhu T, Ding L, Guo X, Yang L, Wen A (2007) Simultaneous Determination of Tramadol

and Acetaminophen in Human Plasma by LC–ESI–MS. Chromatographia 66: 171–178. Available: http://www.springerlink.com/index/10.1365/s10337-007-0268-9. Accessed 19 February 2014.

157. Clements JA, Heading RC, Nimmo WS, Prescott LF (1978) Kinetics of acetaminophen absorption and gastric emptying in man. Clin Pharmacol Ther 24: 420–431. Available: http://www.ncbi.nlm.nih.gov/pubmed/688732. Accessed 19 February 2014.

158. Srinivasan RS, Bourne DW, Putcha L (1994) Application of physiologically based pharmacokinetic models for assessing drug disposition in space. J Clin Pharmacol 34: 692–698. Available: http://www.ncbi.nlm.nih.gov/pubmed/8083402. Accessed 19 February 2014.

159. Peters SA (2012) Physiologically-Based Pharmacokinetic (PBPK) Modeling and Simulations. Hoboken, NJ, USA: John Wiley & Sons, Inc.

160. Reisfeld B, Mayeno AN, Lyons MA, Yang RSH (2007) Computational Toxicology. Ekins S, editor Hoboken, NJ, USA: John Wiley & Sons, Inc. 33-69 p. Available: http://doi.wiley.com/10.1002/9780470145890. Accessed 20 July 2014.

161. Edginton AN, Schmitt W, Willmann S (2006) Development and evaluation of a generic physiologically based pharmacokinetic model for children. Clin Pharmacokinet 45: 1013–1034. Available: http://www.ncbi.nlm.nih.gov/pubmed/16984214.

162. Ben-Shachar R, Chen Y, Luo S, Hartman C, Reed M, et al. (2012) The biochemistry of acetaminophen hepatotoxicity and rescue: a mathematical model. Theor Biol Med Model 9: 55. Available: http://www.pubmedcentral.nih.gov/articlerender.fcgi?artid=3576299&tool=pmcentrez&rendertype=abstract.

163. Péry ARR, Brochot C, Zeman FA, Mombelli E, Desmots S, et al. (2013) Prediction of dose-hepatotoxic response in humans based on toxicokinetic/toxicodynamic modeling with or without in vivo data: a case study with acetaminophen. Toxicol Lett 220: 26–34. Available: http://www.ncbi.nlm.nih.gov/pubmed/23566899. Accessed 5 November 2013.

164. Lin J, Lu A (1997) Role of Pharmacokinetics and Metabolism in Drug Discovery and Development. Pharmacol Rev 49: 403–449.

165. Navid A, Ng DM, Stewart BJ, Wong SE, Lightstone FC (2013) Quantitative In Silico analysis of transient metabolism of acetaminophen and associated causes of hepatotoxicity in humans. In Silico Pharmacol 1: 14. Available: http://www.in-silico-pharmacology.com/content/1/1/14. Accessed 25 February 2014.

166. Geenen S, Yates JWT, Kenna JG, Bois FY, Wilson ID, et al. (2013) Multiscale modelling approach combining a kinetic model of glutathione metabolism with PBPK models of paracetamol and the potential glutathione-depletion biomarkers ophthalmic acid and 5-oxoproline in humans and rats. Integr Biol (Camb) 5: 877–888. Available: http://www.ncbi.nlm.nih.gov/pubmed/23632663. Accessed 15 February 2014.

167. Vajjah P, Isbister GK, Duffull SB (2012) Introduction to pharmacokinetics in clinical toxicology. Methods Mol Biol 929: 289–312. Available: http://www.ncbi.nlm.nih.gov/pubmed/23007434. Accessed 17 July 2014.

168. Levitt DG (2013) Quantitation of small intestinal permeability during normal human drug absorption. BMC Pharmacol Toxicol 14: 34. Available: http://www.pubmedcentral.nih.gov/articlerender.fcgi?artid=3734790&tool=pmcentrez&rendertype=abstract. Accessed 13 June 2014.

169. Morris ME, Levy G (1984) Renal clearance and serum protein binding of acetaminophen

and its major conjugates in humans. J Pharm Sci 73: 1038–1041. Available: http://www.ncbi.nlm.nih.gov/pubmed/6491906. Accessed 2 June 2014.

170. Wishart DS, Jewison T, Guo AC, Wilson M, Knox C, et al. (2013) HMDB 3.0--The Human Metabolome Database in 2013. Nucleic Acids Res 41: D801-7. Available: http://www.pubmedcentral.nih.gov/articlerender.fcgi?artid=3531200&tool=pmcentrez&rendertype=abstract. Accessed 26 May 2014.

171. Naritomi Y, Terashita S, Kagayama A, Sugiyama Y (2003) Utility of hepatocytes in predicting drug metabolism: comparison of hepatic intrinsic clearance in rats and humans in vivo and in vitro. Drug Metab Dispos 31: 580–588. Available: http://www.ncbi.nlm.nih.gov/pubmed/12695346. Accessed 18 December 2014.

172. Gwilt J, Robertson A, McChesney E (1963) Determination of blood and other tissue concentrations of paracetamol in dog and man. J Pharm Pharmacol 15: 440–444. Available: http://www.ncbi.nlm.nih.gov/pubmed/13951545. Accessed 18 December 2014.

173. Forrest JA, Clements JA, Prescott LF (n.d.) Clinical pharmacokinetics of paracetamol. Clin Pharmacokinet 7: 93–107. Available: http://www.ncbi.nlm.nih.gov/pubmed/7039926. Accessed 19 February 2014.

174. Rumack BH (2002) Acetaminophen hepatotoxicity: the first 35 years. J Toxicol Clin Toxicol 40: 3–20. Available: http://www.ncbi.nlm.nih.gov/pubmed/11990202.

175. Mutlib AE, Goosen TC, Bauman JN, Williams JA, Kulkarni S, et al. (2006) Kinetics of acetaminophen glucuronidation by UDP-glucuronosyltransferases 1A1, 1A6, 1A9 and 2B15. Potential implications in acetaminophen-induced hepatotoxicity. Chem Res Toxicol 19: 701–709. Available: http://www.ncbi.nlm.nih.gov/pubmed/16696573. Accessed 25 June 2014.

176. Nagar S, Walther S, Blanchard RL (2006) Sulfotransferase (SULT) 1A1 polymorphic variants *1, *2, and *3 are associated with altered enzymatic activity, cellular phenotype, and protein degradation. Mol Pharmacol 69: 2084–2092. Available: http://www.ncbi.nlm.nih.gov/pubmed/16517757. Accessed 19 February 2014.

177. Marangoni AG (2002) Enzyme Kinetics. Hoboken, NJ, USA: John Wiley & Sons, Inc. Available: http://doi.wiley.com/10.1002/0471267295. Accessed 20 July 2014.

178. Martin U, Temple RM, Winney RJ, Prescott LF (1993) The disposition of paracetamol and its conjugates during multiple dosing in patients with end-stage renal failure maintained on haemodialysis. Eur J Clin Pharmacol 45: 141–145. Available: http://link.springer.com/10.1007/BF00315495. Accessed 20 July 2014.

179. Clements JA, Critchley JA, Prescott LF (1984) The role of sulphate conjugation in the metabolism and disposition of oral and intravenous paracetamol in man. Br J Clin Pharmacol 18: 481–485. Available: http://www.pubmedcentral.nih.gov/articlerender.fcgi?artid=1463596&tool=pmcentrez&rendertype=abstract.

180. Fong BM, Siu TS, Tam S (2011) Persistently increased acetaminophen concentrations in a patient with acute liver failure. Clin Chem 57: 9–11. Available: http://www.ncbi.nlm.nih.gov/pubmed/21189276. Accessed 31 July 2014.

181. Iida S, Mizuma T, Sakuma N, Hayashi M, Awazu S (n.d.) Transport of acetaminophen conjugates in isolated rat hepatocytes. Drug Metab Dispos 17: 341–344. Available: http://www.ncbi.nlm.nih.gov/pubmed/2568918. Accessed 3 March 2014.

182. Jayasinghe KS, Roberts CJ, Read AE (1986) Is biliary excretion of paracetamol significant in man? Br J Clin Pharmacol 22: 363–366. Available:

http://www.pubmedcentral.nih.gov/articlerender.fcgi?artid=1401122&tool=pmcentrez&rendertype=abstract. Accessed 9 July 2014.

183. Lyons MA, Yang RSHH, Mayeno AN, Reisfeld B (2008) Computational toxicology of chloroform: reverse dosimetry using Bayesian inference, Markov chain Monte Carlo simulation, and human biomonitoring data. Environ Health Perspect 116: 1040–1046. Available: http://www.pubmedcentral.nih.gov/articlerender.fcgi?artid=2516557&tool=pmcentrez&rendertype=abstract. Accessed 11 November 2013.

184. Laine JE, Auriola S, Pasanen M, Juvonen RO (2009) Acetaminophen bioactivation by human cytochrome P450 enzymes and animal microsomes. Xenobiotica 39: 11–21. Available: http://www.ncbi.nlm.nih.gov/pubmed/19219744. Accessed 30 May 2014.

185. Riches Z, Bloomer J, Patel a, Nolan a, Coughtrie M (2009) Assessment of cryopreserved human hepatocytes as a model system to investigate sulfation and glucuronidation and to evaluate inhibitors of drug conjugation. Xenobiotica 39: 374–381. Available: http://www.ncbi.nlm.nih.gov/pubmed/19280384. Accessed 11 November 2013.

186. Souliman S, Blanquet S, Beyssac E, Cardot J-M (2006) A level A in vitro/in vivo correlation in fasted and fed states using different methods: applied to solid immediate release oral dosage form. Eur J Pharm Sci 27: 72–79. Available: http://www.ncbi.nlm.nih.gov/pubmed/16169713. Accessed 16 June 2014.

187. Hjelle JJ, Hazelton GA, Klaassen CD (1985) Acetaminophen decreases adenosine 3'-phosphate 5'-phosphosulfate and uridine diphosphoglucuronic acid in rat liver. Drug Metab Dispos 13: 35–41. Available: http://www.ncbi.nlm.nih.gov/pubmed/2858374. Accessed 7 July 2014.

188. Sahajwalla CG, Ayres JW (1991) Multiple-dose acetaminophen pharmacokinetics. J Pharm Sci 80: 855–860. Available: http://www.ncbi.nlm.nih.gov/pubmed/1800709. Accessed 19 February 2014.

189. Lin JH (1994) Dose-dependent pharmacokinetics: experimental observations and theoretical considerations. Biopharm Drug Dispos 15: 1–31. Available: http://www.ncbi.nlm.nih.gov/pubmed/8161713. Accessed 5 August 2014.

190. Hjelle JJ, Klaassen CD (1984) Glucuronidation and biliary excretion of acetaminophen in rats. J Pharmacol Exp Ther 228: 407–413. Available: http://www.ncbi.nlm.nih.gov/pubmed/6694118. Accessed 6 August 2014.

191. Tone Y, Kawamata K, Murakami T, Higashi Y, Yata N (1990) Dose-dependent pharmacokinetics and first-pass metabolism of acetaminophen in rats. J Pharmacobiodyn 13: 327–335. Available: http://www.ncbi.nlm.nih.gov/pubmed/2231264. Accessed 6 August 2014.

192. Zhao L, Pickering G (2011) Paracetamol metabolism and related genetic differences. Drug Metab Rev 43: 41–52. Available: http://www.ncbi.nlm.nih.gov/pubmed/21108564. Accessed 19 February 2014.

193. De Wildt SN, Kearns GL, Leeder JS, Van Den Anker JN (1999) Glucuronidation in humans. Pharmacogenetic and developmental aspects. Clin Pharmacokinet 36: 439–452. doi:10.2165/00003088-199936060-00005.

194. Howell B a, Yang Y, Kumar R, Woodhead JL, Harrill AH, et al. (2012) In vitro to in vivo extrapolation and species response comparisons for drug-induced liver injury (DILI) using DILIsym™: a mechanistic, mathematical model of DILI. J Pharmacokinet Pharmacodyn 39: 527–541. Available: http://www.ncbi.nlm.nih.gov/pubmed/22875368. Accessed 11

September 2014.

195. Jiang X-L, Zhao P, Barrett JS, Lesko LJ, Schmidt S (2013) Application of physiologically based pharmacokinetic modeling to predict acetaminophen metabolism and pharmacokinetics in children. CPT pharmacometrics Syst Pharmacol 2: e80. Available: http://www.pubmedcentral.nih.gov/articlerender.fcgi?artid=3817375&tool=pmcentrez&rendertype=abstract. Accessed 16 September 2014.

196. Carlini EJ, Raftogianis RB, Wood TC, Jin F, Zheng W, et al. (2001) Sulfation pharmacogenetics: SULT1A1 and SULT1A2 allele frequencies in Caucasian, Chinese and African-American subjects. Pharmacogenetics 11: 57–68. Available: http://www.ncbi.nlm.nih.gov/pubmed/11207031. Accessed 19 February 2014.

197. Guillemette C (2003) Pharmacogenomics of human UDP-glucuronosyltransferase enzymes. Pharmacogenomics J 3: 136–158. Available: http://www.ncbi.nlm.nih.gov/pubmed/12815363. Accessed 11 February 2014.

198. Lampe JW, Bigler J, Horner NK, Potter JD (1999) UDP-glucuronosyltransferase (UGT1A1*28 and UGT1A6*2) polymorphisms in Caucasians and Asians: relationships to serum bilirubin concentrations. Pharmacogenetics 9: 341–349. Available: http://www.ncbi.nlm.nih.gov/pubmed/10471066. Accessed 25 February 2014.

199. Maeda H, Hazama S, Shavkat A, Okamoto K, Oba K, et al. (2014) Differences in UGT1A1, UGT1A7, and UGT1A9 polymorphisms between Uzbek and Japanese populations. Mol Diagnosis Ther 18: 333–342. doi:10.1007/s40291-014-0083-6.

200. Court MH, Duan SX, von Moltke LL, Greenblatt DJ, Patten CJ, et al. (2001) Interindividual variability in acetaminophen glucuronidation by human liver microsomes: identification of relevant acetaminophen UDP-glucuronosyltransferase isoforms. J

Pharmacol Exp Ther 299: 998–1006. Available: http://www.ncbi.nlm.nih.gov/pubmed/11714888.

201. Hawton K, Harriss L (2007) Deliberate self-harm in young people: Characteristics and subsequent mortality in a 20-year cohort of patients presenting to hospital. J Clin Psychiatry 68: 1574–1583.

202. Mohamed AB, Zaibi G, Kachouri A (2011) Implementation of RC5 and RC6 block ciphers on digital images. International Multi-Conference on Systems, Signals and Devices, SSD'11 - Summary Proceedings. doi:10.1109/SSD.2011.5767447.

203. Hartington K, Hartley J, Clancy M (2002) Measuring plasma paracetamol concentrations in all patients with drug overdoses; development of a clinical decision rule and clinicians willingness to use it. Emerg Med J 19: 408–411. doi:10.1136/emj.19.5.408.

204. Kaysen GA, Pond SM, Roper MH, Menke DJ, Marrama MA (1985) Combined hepatic and renal injury in alcoholics during therapeutic use of acetaminophen. Arch Intern Med 145: 2019–2023. doi:10.1001/archinte.1985.00360110089021.

205. Heard K, Bui A, Mlynarchek SL, Green JL, Bond GR, et al. (2012) Toxicity From Repeated Doses of Acetaminophen in Children: Assessment of Causality and Dose in Reported Cases. Am J Ther: 1. doi:10.1097/MJT.0b013e3182459c53.

206. Leang Y, Taylor DM, Dargan PI, Wood DM, Greene SL (2014) Reported ingested dose of paracetamol as a predictor of risk following paracetamol overdose. Eur J Clin Pharmacol 70: 1513–1518. Available: http://www.ncbi.nlm.nih.gov/pubmed/25270975.

207. Peters SA (2012) Physiologically-Based Pharmacokinetic (PBPK) Modeling and Simulations: Principles, Methods, and Applications in the Pharmaceutical Industry. Wiley.

208. Krauss M, Burghaus R, Lippert J, Niemi M, Neuvonen P, et al. (2013) Using Bayesian-

PBPK modeling for assessment of inter-individual variability and subgroup stratification. In Silico Pharmacol 1: 6. Available: http://www.in-silico-pharmacology.com/content/1/1/6.

209. Georgopoulos PG, Sasso AF, Isukapalli SS, Lioy PJ, Vallero D a, et al. (2009) Reconstructing population exposures to environmental chemicals from biomarkers: challenges and opportunities. J Expo Sci Environ Epidemiol 19: 149–171. doi:10.1038/jes.2008.9.

210. Reisfeld B, Ivy JH, Lyons MA, Wright JM, Rogers JL, et al. (2013) DoseSim: A tool for pharmacokinetic/pharmacodynamic analysis and dose reconstruction. Bioinformatics 29: 400–401. doi:10.1093/bioinformatics/bts671.

211. Friberg LE, Isbister GK, Hackett LP, Duffull SB (2005) The population pharmacokinetics of citalopram after deliberate self-poisoning: A Bayesian approach. J Pharmacokinet Pharmacodyn 32: 571–605. doi:10.1007/s10928-005-0022-6.

212. Halcomb SE, Sivilotti ML a, Goklaney A, Mullins ME (2005) Pharmacokinetic effects of diphenhydramine or oxycodone in simulated acetaminophen overdose. Acad Emerg Med 12: 169–172. Available: http://www.ncbi.nlm.nih.gov/pubmed/15692141. Accessed 5 September 2014.

213. Tan C, Graudins A (2006) Comparative pharmacokinetics of Panadol Extend and immediate-release paracetamol in a simulated overdose model. EMA - Emerg Med Australas 18: 398–403. doi:10.1111/j.1742-6723.2006.00873.x.

214. Wolchok JD, Williams L, Pinto JT, Fleisher M, Krown SE, et al. (2003) Phase I trial of high dose paracetamol and carmustine in patients with metastatic melanoma. Melanoma Res 13: 189–196. Available: http://www.ncbi.nlm.nih.gov/pubmed/12690304. Accessed

19 February 2014.

215. Heard K, Rumack BH, Green JL, Bucher-Bartelson B, Heard S, et al. (2014) A single-arm clinical trial of a 48-hour intravenous N-acetylcysteine protocol for treatment of acetaminophen poisoning. Clin Toxicol (Phila) 52: 512–518. Available: http://www.ncbi.nlm.nih.gov/pubmed/24708414.

216. Özkan Y, Özalp Y, Savaşer A, Özkan SA (2000) Comparative dissolution testing of paracetamol commercial tablet dosage forms. Acta Pol Pharm - Drug Res 57: 33–41.

217. Kelly K, O'Mahony B, Lindsay B, Jones T, Grattan TJ, et al. (2003) Comparison of the Rates of Disintegration, Gastric Emptying, and Drug Absorption Following Administration of a New and a Conventional Paracetamol Formulation, Using γ Scintigraphy. Pharm Res 20: 1668–1673. doi:10.1023/A:1026155822121.

218. Raffa RB, Pergolizzi J V, Taylor R, Decker JF, Patrick JT (2014) Acetaminophen (Paracetamol) Oral Absorption and Clinical Influences. Pain Pract 14: 668–677. Available: http://doi.wiley.com/10.1111/papr.12130.

219. Hixson a. W, Crowell JH (1931) Dependence of Reaction Velocity upon surface and Agitation. Ind Eng Chem 23: 923–931. Available: http://pubs.acs.org/doi/abs/10.1021/ie50260a018.

220. Cupera J (2009) Mathematical models of dissolution Masarykova Univerzita.

221. Tsamandouras N, Rostami-Hodjegan A, Aarons L (2013) Combining the "bottom-up" and "top-down" approaches in pharmacokinetic modelling: Fitting PBPK models to observed clinical data. Br J Clin Pharmacol: 0–16. Available: http://www.ncbi.nlm.nih.gov/pubmed/24033787.

222. Perera V, Bies RR, Mo G, Dolton MJ, Carr VJ, et al. (2014) Optimal Sampling of

Antipsychotic Medicines: A Pharmacometric Approach for Clinical Practice. Br J Clin Pharmacol: 1–36. Available: http://www.ncbi.nlm.nih.gov/pubmed/24773369.

223. Verner MA, McDougall R, Johanson G (2012) Using population physiologically based pharmacokinetic modeling to determine optimal sampling times and to interpret biological exposure markers: The example of occupational exposure to styrene. Toxicol Lett 213: 299–304. doi:10.1016/j.toxlet.2012.05.024.

224. Chenel M, Bouzom F, Aarons L, Ogungbenro K (2008) Drug-drug interaction predictions with PBPK models and optimal multiresponse sampling time designs: Application to midazolam and a phase i compound. Part 1: Comparison of uniresponse and multiresponse designs using PopDes. J Pharmacokinet Pharmacodyn 35: 635–659. doi:10.1007/s10928-008-9104-6.

225. Kim HJ, Rozman P, Madhu C, Klaassen CD (1992) Homeostasis of sulfate and 3'-phosphoadenosine 5'-phosphosulfate in rats after acetaminophen administration. J Pharmacol Exp Ther 261: 1015–1021.

226. Chambers J, Levi P (1992) Organophosphates: chemistry, fate and effects. San Diego: Academic Press.

227. Casida JE (2009) Pest Toxicology : The Primary Mechanisms of Pesticide Action. Rev Lit Arts Am: 609–619.

228. Calvert GM, Karnik J, Mehler L, Beckman J, Morrissey B, et al. (2008) Acute Pesticide Poisoning Among Agricultural Workers in the United States , 1998 – 2005. Am J Ind Med 898: 883–898. doi:10.1002/ajim.20623.

229. Eaton DL, Daroff RB, Autrup H, Bridges J, Buffler P, et al. (2008) Review of the toxicology of chlorpyrifos with an emphasis on human exposure and neurodevelopment.

Crit Rev Toxicol 38 Suppl 2: 1–125. Available: http://www.ncbi.nlm.nih.gov/pubmed/18726789. Accessed 1 July 2010.

230. Nigg HN, Knaak JB (2000) Blood cholinesterases as human biomarkers of organophosphorus pesticide exposure. Rev Environ Contam Toxicol 163: 29–111. Available: http://www.ncbi.nlm.nih.gov/pubmed/10771584.

231. Clegg DJ, van Gemert M (n.d.) Determination of the reference dose for chlorpyrifos: proceedings of an expert panel. J Toxicol Environ Health B Crit Rev 2: 211–255. Available: http://www.ncbi.nlm.nih.gov/pubmed/10429680.

232. Rohlman DS, Anger WK, Lein PJ (2011) Correlating neurobehavioral performance with biomarkers of organophosphorous pesticide exposure. Neurotoxicology 32: 268–276. Available: http://www.ncbi.nlm.nih.gov/pubmed/21182866.

233. Roldán-Tapia L, Parrón T, Sánchez-Santed F (n.d.) Neuropsychological effects of long-term exposure to organophosphate pesticides. Neurotoxicol Teratol 27: 259–266. Available: http://www.ncbi.nlm.nih.gov/pubmed/15734277.

234. Reidy TJ, Bolter JF, Cone JE (1994) Neuropsychological sequelae of methyl bromide: a case study. Brain Inj 8: 83–93. Available: http://www.ncbi.nlm.nih.gov/pubmed/8124320.

235. Farahat TM, Abdelrasoul GM, Amr MM, Shebl MM, Farahat FM, et al. (2003) Neurobehavioural effects among workers occupationally exposed to organophosphorous pesticides. Occup Environ Med 60: 279–286. Available: http://www.ncbi.nlm.nih.gov/pubmed/12660376.

236. Mackenzie Ross SJ, Brewin CR, Curran HV, Furlong CE, Abraham-Smith KM, et al. (n.d.) Neuropsychological and psychiatric functioning in sheep farmers exposed to low levels of organophosphate pesticides. Neurotoxicol Teratol 32: 452–459. Available:

http://www.ncbi.nlm.nih.gov/pubmed/20227490.

237. Terry A V, Buccafusco JJ, Gearhart DA, Beck WD, Middlemore-Risher M-L, et al. (2011) Repeated, intermittent exposures to diisopropylfluorophosphate in rats: protracted effects on cholinergic markers, nerve growth factor-related proteins, and cognitive function. Neuroscience 176: 237–253. Available: http://www.ncbi.nlm.nih.gov/pubmed/21185910.

238. Johnson FO, Chambers JE, Nail CA, Givaruangsawat S, Carr RL (2009) Developmental chlorpyrifos and methyl parathion exposure alters radial-arm maze performance in juvenile and adult rats. Toxicol Sci 109: 132–142. Available: http://www.ncbi.nlm.nih.gov/pubmed/19293373.

239. Ivens IA, Schmuck G, Machemer L (1998) Learning and memory of rats after long-term administration of low doses of parathion. Toxicol Sci 46: 101–111. Available: http://www.ncbi.nlm.nih.gov/pubmed/9928673.

240. López-Granero C, Cardona D, Giménez E, Lozano R, Barril J, et al. (2013) Chronic dietary exposure to chlorpyrifos causes behavioral impairments, low activity of brain membrane-bound acetylcholinesterase, and increased brain acetylcholinesterase-R mRNA. Toxicology 308: 41–49. Available: http://www.ncbi.nlm.nih.gov/pubmed/23545134.

241. Terry A V, Beck WD, Warner S, Vandenhuerk L, Callahan PM (2012) Chronic impairments in spatial learning and memory in rats previously exposed to chlorpyrfos or diisopropylfluorophosphate. Neurotoxicol Teratol 34: 1–8. Available: http://www.ncbi.nlm.nih.gov/pubmed/22024239.

242. Terry A V, Callahan PM, Beck WD, Vandenhuerk L, Sinha S, et al. (n.d.) Repeated exposures to diisopropylfluorophosphate result in impairments of sustained attention and

persistent alterations of inhibitory response control in rats. Neurotoxicol Teratol 44: 18–29. Available: http://www.ncbi.nlm.nih.gov/pubmed/24819591.

243. Cohn J, MacPhail RC (1997) Chlorpyrifos produces selective learning deficits in rats working under a schedule of repeated acquisition and performance. J Pharmacol Exp Ther 283: 312–320. Available: http://www.ncbi.nlm.nih.gov/pubmed/9336338.

244. Dreyling E, Dederick EJ, Chari R, Resnick B, Malecki KC, et al. (2007) Tracking health and the environment: a pilot test of environmental public health indicators. J Environ Health 70: 9–16, 38, 40-2. Available: http://www.ncbi.nlm.nih.gov/pubmed/18189034.

245. Egorov AI, Dalbokova D, Krzyzanowski M (2013) Biomonitoring-based environmental public health indicators. Methods Mol Biol 930: 275–293. Available: http://www.ncbi.nlm.nih.gov/pubmed/23086846.

246. Furgal C, Gosselin P (n.d.) Challenges and directions for environmental public health indicators and surveillance. Can J Public Health 93 Suppl 1: S5-8. Available: http://www.ncbi.nlm.nih.gov/pubmed/12425168.

247. Soltaninejad K, Abdollahi M (2009) Current opinion on the science of organophosphate pesticides and toxic stress: a systematic review. Med Sci Monit 15: RA75-90. Available: http://www.ncbi.nlm.nih.gov/pubmed/19247260.

248. Lee YS, Lewis JA, Ippolito DL, Hussainzada N, Lein PJ, et al. (2016) Repeated exposure to neurotoxic levels of chlorpyrifos alters hippocampal expression of neurotrophins and neuropeptides. Toxicology 340: 53–62. Available: http://www.ncbi.nlm.nih.gov/pubmed/26775027.

249. Pancetti F, Olmos C, Dagnino-Subiabre A, Rozas C, Morales B (2007) Noncholinesterase effects induced by organophosphate pesticides and their relationship to cognitive

processes: implication for the action of acylpeptide hydrolase. J Toxicol Environ Health B Crit Rev 10: 623–630. Available: http://www.ncbi.nlm.nih.gov/pubmed/18049927.

250. Casida JE, Quistad GB (2005) Serine hydrolase targets of organophosphorus toxicants. Chem Biol Interact 157–158: 277–283. Available: http://www.ncbi.nlm.nih.gov/pubmed/16243304.

251. Terry A V, Stone JD, Buccafusco JJ, Sickles DW, Sood A, et al. (2003) Repeated exposures to subthreshold doses of chlorpyrifos in rats: hippocampal damage, impaired axonal transport, and deficits in spatial learning. J Pharmacol Exp Ther 305: 375–384. Available: http://www.ncbi.nlm.nih.gov/pubmed/12649392.

252. Vorhees C V, Williams MT (2006) Morris water maze: procedures for assessing spatial and related forms of learning and memory. Nat Protoc 1: 848–858. Available: http://www.ncbi.nlm.nih.gov/pubmed/17406317.

253. United States Environmental Protection Agency (2016) Benchmark Dose (BMD) Methods. Available: https://www.epa.gov/bmds/benchmark-dose-bmd-methods. Accessed 23 March 2016.

254. Lepage GP (n.d.) lsqfit. Available: https://github.com/gplepage/lsqfit.

255. Schmidt M, Lipson H (2014) Eureqa. Available: www.nutonian.com. Accessed 10 April 2016.

256. Netherton SD, Elias JW, Albrecht NN, Acosta C, Hutton JT, et al. (n.d.) Changes in the performance of parkinsonian patients and normal aged on the Benton Visual Retention Test. Exp Aging Res 15: 13–18. Available: http://www.ncbi.nlm.nih.gov/pubmed/2583210.

257. Brickman AM, Stern Y, Small SA (2011) Hippocampal subregions differentially associate

with standardized memory tests. Hippocampus 21: 923–928. Available: http://www.ncbi.nlm.nih.gov/pubmed/20824727.

258. Alexander BH, Burns CJ, Bartels MJ, Acquavella JF, Mandel JS, et al. (2006) Chlorpyrifos exposure in farm families: results from the farm family exposure study. J Expo Sci Environ Epidemiol 16: 447–456. Available: http://www.ncbi.nlm.nih.gov/pubmed/16570094.

259. Committee on Human Health Risks of Trichloroethylene N. R. C. (2006) Assessing the Human Health Risks of Trichloroethylene: Key Scientific Issues. The National Academies Press.

260. Saihan EM, Burton JL, Heaton KW (1978) A new syndrome with pigmentation, scleroderma, gynaecomastia, Raynaud's phenomenon and peripheral neuropathy. Br J Dermatol 99: 437–440. Available: http://www.ncbi.nlm.nih.gov/pubmed/213095.

261. Flindt-Hansen H, Isager H (1987) Scleroderma after occupational exposure to trichlorethylene and trichlorethane. Acta Derm Venereol 67: 263–264. Available: http://www.ncbi.nlm.nih.gov/pubmed/2442944.

262. Czirják L, Pócs E, Szegedi G (1994) Localized scleroderma after exposure to organic solvents. Dermatology 189: 399–401. Available: http://www.ncbi.nlm.nih.gov/pubmed/7873829.

263. Dubrow R, Gute DM (1987) Cause-specific mortality among Rhode Island jewelry workers. Am J Ind Med 12: 579–593. Available: http://www.ncbi.nlm.nih.gov/pubmed/2961258.

264. Gist GL, Burg JR (n.d.) Trichloroethylene--a review of the literature from a health effects perspective. Toxicol Ind Health 11: 253–307. Available:

http://www.ncbi.nlm.nih.gov/pubmed/7482570.

265. Griffin JM, Gilbert KM, Lamps LW, Pumford NR (2000) CD4(+) T-cell activation and induction of autoimmune hepatitis following trichloroethylene treatment in MRL+/+ mice. Toxicol Sci 57: 345–352. Available: http://www.ncbi.nlm.nih.gov/pubmed/11006364.

266. Cai P, König R, Boor PJ, Kondraganti S, Kaphalia BS, et al. (2008) Chronic exposure to trichloroethene causes early onset of SLE-like disease in female MRL +/+ mice. Toxicol Appl Pharmacol 228: 68–75. Available: http://www.ncbi.nlm.nih.gov/pubmed/18234256.

267. Carambia A, Herkel J (2010) CD4 T cells in hepatic immune tolerance. J Autoimmun 34: 23–28. Available: http://www.ncbi.nlm.nih.gov/pubmed/19720498.

268. Crispe IN (2009) The liver as a lymphoid organ. Annu Rev Immunol 27: 147–163. Available: http://www.ncbi.nlm.nih.gov/pubmed/19302037.

269. Liu D-F, Wei W, Song L-H (2006) Protective effect of paeoniflorin on immunological liver injury induced by bacillus Calmette-Guerin plus lipopolysaccharide: modulation of tumour necrosis factor-alpha and interleukin-6 MRNA. Clin Exp Pharmacol Physiol 33: 332–339. Available: http://www.ncbi.nlm.nih.gov/pubmed/16620297.

270. Wuestefeld T, Klein C, Streetz KL, Betz U, Lauber J, et al. (2003) Interleukin-6/glycoprotein 130-dependent pathways are protective during liver regeneration. J Biol Chem 278: 11281–11288. Available: http://www.ncbi.nlm.nih.gov/pubmed/12509437.

271. El-Assal O, Hong F, Kim W-H, Radaeva S, Gao B (2004) IL-6-deficient mice are susceptible to ethanol-induced hepatic steatosis: IL-6 protects against ethanol-induced oxidative stress and mitochondrial permeability transition in the liver. Cell Mol Immunol 1: 205–211. Available: http://www.ncbi.nlm.nih.gov/pubmed/16219169.

272. Bansal MB, Kovalovich K, Gupta R, Li W, Agarwal A, et al. (2005) Interleukin-6 protects

hepatocytes from CCl4-mediated necrosis and apoptosis in mice by reducing MMP-2 expression. J Hepatol 42: 548–556. Available: http://www.ncbi.nlm.nih.gov/pubmed/15763341.

273. Wunderlich FT, Ströhle P, Könner AC, Gruber S, Tovar S, et al. (2010) Interleukin-6 signaling in liver-parenchymal cells suppresses hepatic inflammation and improves systemic insulin action. Cell Metab 12: 237–249. Available: http://www.ncbi.nlm.nih.gov/pubmed/20816090.

274. Wallenius V, Wallenius K, Hisaoka M, Sandstedt J, Ohlsson C, et al. (2001) Retarded liver growth in interleukin-6-deficient and tumor necrosis factor receptor-1-deficient mice. Endocrinology 142: 2953–2960. Available: http://www.ncbi.nlm.nih.gov/pubmed/11416016.

275. Klein C, Wüstefeld T, Assmus U, Roskams T, Rose-John S, et al. (2005) The IL-6-gp130-STAT3 pathway in hepatocytes triggers liver protection in T cell-mediated liver injury. J Clin Invest 115: 860–869. Available: http://www.ncbi.nlm.nih.gov/pubmed/15761498.

276. Hoffmann E, Ashouri J, Wolter S, Doerrie A, Dittrich-Breiholz O, et al. (2008) Transcriptional regulation of EGR-1 by the interleukin-1-JNK-MKK7-c-Jun pathway. J Biol Chem 283: 12120–12128. Available: http://www.ncbi.nlm.nih.gov/pubmed/18281687.

277. Iwamoto S, Kido M, Aoki N, Nishiura H, Maruoka R, et al. (2013) TNF-α is essential in the induction of fatal autoimmune hepatitis in mice through upregulation of hepatic CCL20 expression. Clin Immunol 146: 15–25. Available: http://www.ncbi.nlm.nih.gov/pubmed/23178752.

278. Zhao L, Tang Y, You Z, Wang Q, Liang S, et al. (2011) Interleukin-17 contributes to the

pathogenesis of autoimmune hepatitis through inducing hepatic interleukin-6 expression. PLoS One 6: e18909. Available: http://www.ncbi.nlm.nih.gov/pubmed/21526159.

279. Eklund KK, Niemi K, Kovanen PT (2012) Immune functions of serum amyloid A. Crit Rev Immunol 32: 335–348. Available: http://www.ncbi.nlm.nih.gov/pubmed/23237509.

280. Yoshida A, Hosokawa T, Nishi Y, Koyama K, Nakamura K, et al. (1989) Studies on age-related functional changes in regulatory T cells and B cells involved in the autoantibody production of MRL/MpJ- +/+ mice. Mech Ageing Dev 50: 179–192. Available: http://www.ncbi.nlm.nih.gov/pubmed/2601416.

281. Kanno H, Nose M, Itoh J, Taniguchi Y, Kyogoku M (1992) Spontaneous development of pancreatitis in the MRL/Mp strain of mice in autoimmune mechanism. Clin Exp Immunol 89: 68–73. Available: http://www.ncbi.nlm.nih.gov/pubmed/1352748.

282. Toda I, Sullivan BD, Rocha EM, Da Silveira LA, Wickham LA, et al. (1999) Impact of gender on exocrine gland inflammation in mouse models of Sjögren's syndrome. Exp Eye Res 69: 355–366. Available: http://www.ncbi.nlm.nih.gov/pubmed/10504269.

283. Gottenberg J-E, Dayer J-M, Lukas C, Ducot B, Chiocchia G, et al. (2012) Serum IL-6 and IL-21 are associated with markers of B cell activation and structural progression in early rheumatoid arthritis: results from the ESPOIR cohort. Ann Rheum Dis 71: 1243–1248. Available: http://www.ncbi.nlm.nih.gov/pubmed/22532637.

284. Chun H-Y, Chung J-W, Kim H-A, Yun J-M, Jeon J-Y, et al. (2007) Cytokine IL-6 and IL-10 as biomarkers in systemic lupus erythematosus. J Clin Immunol 27: 461–466. Available: http://www.ncbi.nlm.nih.gov/pubmed/17587156.

285. Weller M, Stevens A, Sommer N, Melms A, Dichgans J, et al. (1991) Comparative analysis of cytokine patterns in immunological, infectious, and oncological neurological

disorders. J Neurol Sci 104: 215–221. Available: http://www.ncbi.nlm.nih.gov/pubmed/1940975.

286. Tovey MG, Gugenheim J, Guymarho J, Blanchard B, Vanden Broecke C, et al. (1991) Genes for interleukin-1, interleukin-6, and tumor necrosis factor are expressed at markedly reduced levels in the livers of patients with severe liver disease. Autoimmunity 10: 297–310. Available: http://www.ncbi.nlm.nih.gov/pubmed/1772964.

287. Wang G, Cai P, Ansari GAS, Khan MF (2007) Oxidative and nitrosative stress in trichloroethene-mediated autoimmune response. Toxicology 229: 186–193. Available: http://www.ncbi.nlm.nih.gov/pubmed/17123686.

288. Wang G, Wang J, Ma H, Ansari GAS, Khan MF (2013) N-Acetylcysteine protects against trichloroethene-mediated autoimmunity by attenuating oxidative stress. Toxicol Appl Pharmacol 273: 189–195. Available: http://www.ncbi.nlm.nih.gov/pubmed/23993974.

APPENDIX A

SUMMARY TABLE FOR ACETMINOPHEN LITERATURE REVIEW

The acetaminophen PBPK models described throughout Chapter 4 required an extensive set of pharmacokinetic data from the literature for model calibration and testing. Table presents a summary of these sources and notes how each data set was used.

TABLE A. Pharmacokinetic data utilized in development of acetaminophen models

Reference	Route of administration	Dose	Measured biomarkers	Number of subjects (sex)	Use in model development: training (T) or test/validation (V)	Group Designation
Ameer et al. 1981 [139]	Oral	650 mg	Plasma: APAP	1 (M)	V	A
	IV	650 mg	Plasma: APAP	1 (M)	V	A
Chen et al. 1996 [140]	Oral	1000 mg	Plasma & Urine: APAP, APAP-G, APAP-S	10 (M/F)	*	A
Chiew et al., 2010 [141]	Oral	80 mg/kg	Plasma: APAP, APAP-G, APAP-S	9 (M/F)	T	A
Chan et al. 1997 [136]	Oral	20 mg/kg	Plasma: APAP, APAP-G, APAP-S	6 (M/F)	T	B
Critchley et al. 2005 [137]	Oral	20 mg/kg	Plasma & Urine: APAP, APAP-G, APAP-S	11 (M/F)	V	A
	Oral	20 mg/kg	Plasma & Urine: APAP, APAP-G, APAP-S	9 (M/F)	V	B
Critchley et al. 1986 [138]	Oral	1500 mg	Urine: APAP, APAP-G, APAP-S	111 (M/F)	T	A
Esteban et al. 1996 [142]	Oral	1500 mg	Urine: APAP, APAP-G, APAP-S	71 (M/F)	V	A
Halcomb et al. 2005 [212] †	Oral	5000 mg	Plasma: APAP	10 (M/F)	V	-
Jensen et al. 2004 [143]	Oral	1000 mg	Plasma: APAP, APAP-G, APAP-S	6 (M/F)	V	A
Itoh et al. 2001 [144]	Oral	1000 mg	Plasma: APAP, APAP-G, APAP-S	5 (M)	V	B
Kamali 1993 [145]	Oral	1500 mg	Plasma: APAP, Urine: APAP, APAP-G, APAP-S	10 (M/F)	V	A
Kim et al. 2010 [146]	Oral	1000 mg	Plasma: APAP, APAP-G, APAP-S	12 (M/F)	V	B
Lau et al. 1994 [147]	Oral	20 mg/kg	Plasma & Urine: APAP, APAP-G, APAP-S	6 (M/F)	T	B
Prescott 1980 [148]	Oral	20 mg/kg	Plasma & Urine: APAP, APAP-G, APAP-S	8 (M/F)	T	A
	Oral	12 mg/kg	Plasma: APAP	4 (M/F)	T	A
	IV	12 mg/kg	Plasma: APAP	4 (M/F)	T	A
Prescott 1989 [149]	Oral	1000 mg	Plasma: APAP, APAP-G, APAP-S	10	V	A
Rawlins et al. 1977 [150]	Oral	500 mg	Plasma: APAP	6 (M)	V	A
	Oral	1000 mg	Plasma: APAP	6 (M)	V	A

Reference	Route of administration	Dose	Measured biomarkers	Number of subjects (sex)	Use in model development: training (T) or test/validation (V)	Group Designation
	Oral	2000 mg	Plasma: APAP	6 (M)	V	A
	IV	1000 mg	Plasma: APAP	6 (M)	T	A
Shinoda et al. 2007 [151]	Oral	1000 mg	Plasma: APAP, APAP-G, APAP-S	5 (M/F)	T	B
Tan et al. 2012 [152]	Oral	500 mg	Plasma & Urine: APAP, APAP-G	12 (***)	T	B
Tonoli et al. 2012 [153]	IV	1000 mg	Plasma: APAP, APAP-G	2 (***)	V	A
Volak et al. 2012 [154]	Oral	325 mg	Plasma: APAP, APAP-G, APAP-S	8 (M/F)	T	A
Wolchok et al. [214] †	Oral	10 g – 40 g	Plasma: APAP	36 (M/F)	T/V	-
Yin et al. 2001 [155]	Oral	500	Plasma: APAP	12 (M)	V	B
Zhu et al. 2007 [156]	Oral	650mg	Plasma: APAP	10 (M)	**	B

* Data were not used. APAP-G measurement methodology was different from that used in other studies.

** Data were not used. APAP was administered in combination with Tramadol.

*** Not specified

†Used only in APAP overdose dataset

APPENDIX B

GOVERNING EQUATIONS FOR ACETAMINOPHEN PBPK MODEL

Chapter 4 describes the use of governing equations to describe the absorption, distribution, metabolism, and elimination of acetaminophen. The following table summarizes the equations used throughout this chapter and notes which equations were used for the overdose acetaminophen model.

TABLE B. System of governing equations for acetaminophen PBPK modeling

	APAP	APAP-G	APAP-S
fat	$\frac{dC_{fat}^{APAP}}{dt} = \frac{Q_{fat}\left(C_A^{APAP} - C_{V-fat}^{APAP}\right)}{V_{fat}}$	$\frac{dC_{fat}^{APAP-G}}{dt} = \frac{Q_{fat}\left(C_A^{APAP-G} - C_{V-fat}^{APAP-G}\right)}{V_{fat}}$	$\frac{dC_{fat}^{APAP-G}}{dt} = \frac{Q_{fat}\left(C_A^{APAP-S} - C_{V-fat}^{APAP-S}\right)}{V_{fat}}$
muscle	$\frac{dC_{muscle}^{APAP}}{dt} = \frac{Q_{muscle}\left(C_A^{APAP} - C_{V-muscle}^{APAP}\right)}{V_{muscle}}$	$\frac{dC_{muscle}^{APAP-G}}{dt} = \frac{Q_{muscle}\left(C_A^{APAP-G} - C_{V-muscle}^{APAP-G}\right)}{V_{muscle}}$	$\frac{dC_{muscle}^{APAP-S}}{dt} = \frac{Q_{muscle}\left(C_A^{APAP-S} - C_{V-muscle}^{APAP-S}\right)}{V_{muscle}}$
liver	$\frac{dC_{liver}^{APAP}}{dt} = \frac{Q_{liver}\left(C_A^{APAP} - C_{V-liver}^{APAP}\right) - v_{cyp} - v_{APAP-G} - v_{APAP-S}}{V_{liver}}$	$\frac{dC_{liver}^{APAP-G}}{dt} = \frac{Q_{liver}\left(C_A^{APAP-G} - C_{V-liver}^{APAP-G}\right) + v_{mem-APAP-G}}{V_{liver}}$	$\frac{dC_{liver}^{APAP-S}}{dt} = \frac{Q_{liver}\left(C_A^{APAP-S} - C_{V-liver}^{APAP-S}\right) + v_{mem-APAP-S}}{V_{liver}}$
hepatocyte	–	$\frac{dA_{hep}^{APAP-G}}{dt} = v_{APAP-G} - v_{mem}^{APAP-G}$	$\frac{dA_{hep}^{APAP-S}}{dt} = v_{APAP-S} - v_{mem}^{APAP-S}$
kidney	$\frac{dC_{kidney}^{APAP}}{dt} = \frac{\frac{dA_{abs}}{dt} + Q_{kidney}\left(C_A^{APAP} - C_{V-kidney}^{APAP}\right) - k_R^{APAP} \cdot C_A^{APAP}}{V_{kidney}}$	$\frac{dC_{kidney}^{APAP-G}}{dt} = \frac{Q_{kidney}\left(C_A^{APAP-G} - C_{V-kidney}^{APAP-G}\right) - k_R^{APAP-G} \cdot C_A^{APAP-G}}{V_{kidney}}$	$\frac{dC_{kidney}^{APAP-G}}{dt} = \frac{Q_{kidney}\left(C_A^{APAP-S} - C_{V-kidney}^{APAP-S}\right) - k_R^{APAP-S} \cdot C_A^{APAP-S}}{V_{kidney}}$
GI: Therapeutic	$\frac{dA_{GI}^{APAP}}{dt} = I(t) - \frac{M\left[\exp\left(\frac{-t}{T_G}\right) - \exp\left(\frac{-t}{T_P}\right)\right]}{T_G - T_P}$	–	–
GI: Overdose	$\frac{dA_{ST,S}^{APAP}}{dt} = I(t) - k(t) \cdot A_{ST,S}^{APAP}$ $\frac{dA_{ST,\mathrm{Aq}}^{APAP}}{dt} = k(t) \cdot A_{ST,S}^{APAP} - \left(\frac{1}{T_G}\right) A_{ST,Aq}^{APAP}$ $\frac{dA_{ST,\mathrm{GI}}^{APAP}}{dt} = \left(\frac{1}{T_G}\right) A_{ST,Aq}^{APAP} + Q_G\left(C_A^{APAP} - C_{V-G}^{APAP}\right)$	–	–
slowly perfused	$\frac{dC_{sp}^{APAP}}{dt} = \frac{Q_{sp}\left(C_A^{APAP} - C_{V-sp}^{APAP}\right)}{V_{sp}}$	$\frac{dC_{sp}^{APAP-G}}{dt} = \frac{Q_{sp}\left(C_A^{APAP-G} - C_{V-sp}^{APAP-G}\right)}{V_{sp}}$	$\frac{dC_{sp}^{APAP-S}}{dt} = \frac{Q_{sp}\left(C_A^{APAP-S} - C_{V-sp}^{APAP-S}\right)}{V_{sp}}$

rapidly perfused	$\frac{dC_{rp}^{APAP}}{dt} = \frac{Q_{rp}\left(C_A^{APAP} - C_{V-rp}^{APAP}\right)}{V_{rp}}$	$\frac{dC_{rp}^{APAP-G}}{dt} = \frac{Q_{rp}\left(C_A^{APAP-G} - C_{V-rp}^{APAP-G}\right)}{V_{rp}}$	$\frac{dC_{rp}^{APAP-S}}{dt} = \frac{Q_{rp}\left(C_A^{APAP-S} - C_{V-rp}^{APAP-S}\right)}{V_{rp}}$
urine	$\frac{dA_e^{APAP}}{dt} = k_R^{APAP} \cdot C_A^{APAP}$	$\frac{dA_e^{APAP-G}}{dt} = k_R^{APAP-G} \cdot C_A^{APAP-G}$	$\frac{dA_e^{APAP-S}}{dt} = k_R^{APAP-S} \cdot C_A^{APAP-S}$
arterial blood concentration	$\frac{dC_{BLA}^{APAP}}{dt} = \frac{Q_C\left(C_V^{APAP} - C_A^{APAP}\right)}{V_{BLA}}$ $C_A^{APAP} = \frac{A_A^{APAP}}{V_{BLA}}$	$\frac{dC_{BLA}^{APAP-G}}{dt} = \frac{Q_C\left(C_V^{APAP-G} - C_A^{APAP-G}\right)}{V_{BLA}}$ $C_A^{APAP-G} = \frac{A_A^{APAP-G}}{V_{BLA}}$	$\frac{dC_{BLA}^{APAP-S}}{dt} = \frac{Q_C\left(C_V^{APAP-S} - C_A^{APAP-S}\right)}{V_{BLA}}$ $C_A^{APAP-S} = \frac{A_A^{APAP-S}}{V_{BLA}}$
venous blood concentration (pooled)	$\frac{dC_{BLV}^{APAP}}{dt} = \frac{\sum_T Q_T C_{V-T}^{APAP} - Q_C C_V^{APAP} + D_{IV}(t)}{V_{BLA}}$, $C_V^{APAP} = \frac{A_V^{APAP}}{V_{BLV}}$ where $D_{IV}(t)$ is the rate of intravenous APAP dosing	$\frac{dC_{BLV}^{APAP-G}}{dt} = \frac{\sum_T Q_T C_{V-T}^{APAP-G} - Q_C C_V^{APAP-G}}{V_{BLA}}$ $C_V^{APAP-G} = \frac{A_V^{APAP-G}}{V_{BLV}}$	$\frac{dC_{BLV}^{APAP-S}}{dt} = \frac{\sum_T Q_T C_{V-T}^{APAP-S} - Q_C C_V^{APAP-S}}{V_{BLA}}$ $C_V^{APAP-S} = \frac{A_V^{APAP-S}}{V_{BLV}}$